Crystallization, Phase Transformation and Thermo-mechanical Studies of Poly(1-butene) Nanocomposites

A Thesis submitted to the

UNIVERSITY OF PUNE

For the degree of

DOCTOR OF PHILOSOPHY (Ph.D.)

In

CHEMISTRY

By

SANTOSH D. WANJALE

Polymer Science and Engineering Division

National Chemical Laboratory

Pune - 411008 (India)

JULY 2007

Dedicated to my Late Parents

CERTIFICATE

Certified that the work incorporated in the thesis, **"Crystallization, Phase Transformation and Thermo-mechanical Studies of Poly(1-butene) Nanocomposites"**, submitted by Mr. Santosh D. Wanjale was carried out by the candidate under my supervision. Such material as has been obtained from other sources has been duly acknowledged in the thesis.

Dr. Jyoti P. Jog

Research guide

Polymer Science and Engineering Division

National Chemical Laboratory

Pune - 411008

DECLARATION

I hereby declare that the work presented in the thesis entitled, "**Crystallization, Phase Transformation and Thermo-mechanical Studies of Poly(1-butene) Nanocomposites**", submitted for Ph.D. degree in Chemistry to The University of Pune, has been carried out under the supervision of Dr. Jyoti P. Jog at Polymer Science and Engineering Division, National Chemical Laboratory, Pune. The work is original and has not been submitted in part or in full by me for any degree or diploma to this or any other University.

July 2007 (Santosh D. Wanjale)

Pune

Acknowledgements

It gives me a great pleasure to acknowledge everyone who has assisted me directly or indirectly to complete the thesis work in time.

I gratefully thank Dr. (Mrs.) Jyoti P Jog, research advisor, for her great encouragement, support, and guidance. She has taught me the basics of polymer science and gave a proper direction to my work. Her fervor and perspective helped me adapt to the new world of polymers both personally and professionally. I really enjoyed the freedom of work during my thesis course.

I am grateful to Dr. S. Sivaram, Director, NCL, for giving me an opportunity to work in this prestigious research institute. I would like to thank Dr. MG Kulkarni, Head, Polymer Science and Engineering Division and Dr. BD Kulkarni, Head, Chemical Engineering and Process Development Division for their constant support and encouragement.

I would like to thank Rajendra Kalgaonkar for his relentless support and friendship, which made every days work an enjoyable experience. His calmness and thinking on every aspect whether general or scientific always enchanted me. He was always there to solve any problem in the lab. I would like to express my sincere thanks to Dr. L. Priya. She was the first one who introduced me to the various characterization techniques of polymers. She always helped me in the personal as well as technical problems. Thanks (not enough) to Rajendra and Priya for being with me, it's really a cherished dream for me to work with you. I gratefully thank Nimhan, Belwalkar, Pednekar, Thandavarayan and Shedge families for their constant encouragement during my thesis work.

My cordial thanks to lab mates who have helped me in all possible ways and for being my extended family during the course. Thank you, Rajendra, Dr. L. Priya, Dr. Neelima Bulakh, Sangeeta Hambir, Dr. Nabi Saheb, Sunita Thombre, Prashant Patil, Chetan Chanmal, M. Dhanalaxmi, Amol Ridhore, Mrs. Kulkarni, Mrs. Marathe, Sachin Punde, Pravin Kodgire, Satish Peddini, Yashodhan Gokhale, S. Kumari, Sona, Rajisha, Remya, Asha, Varad, Bhupendra, Harshada and Snehal.

My special thanks to sisters, Alka and Kalpana, and brother - in - laws for their priceless help, encouragement and love during my difficult times. I will never forget the days that enjoyed with my nephews, Amit, Kiran, Abhijeet and nieces, Anu, Sumati and Sheetal.

It gives me great pleasure to acknowledge Vivek Borkar and Aniruddha Dhupe for their relentless help, support and friendship. It was a wonderful experience to work with Dr. Satish Ogale, Dr. U K Kharul, Dr. (Mrs.) V Ramaswamy and Dr. Prakash Wadgaonkar. I would like to thank Drs. Gurshran Grover, Ashish Lele, C. Ramesh, C. Rajan, M V Badiger, A Dhoble, K Guruswamy, S Nene, C V Rode, K Pandare, Menon and my college professors, H G Damle, R C Chikate, (Mrs.) S Kale, (Mrs.) A Datar, S Sonawane and Satpute for their encouragement. I am very much thankful to Harshvardhan Pol and E. Deenadayalan from Polymer Processing Center, R Pasricha, A Harkare and Purv Purohit for TEM, A B Gaikwad for SEM, Bhujang, Dhawale and Girme for their cooperation. Many thanks are due to the Administrative staff, Library staff, Engineering services, Stores and Purchase for their cooperation. My sincere thanks to Bharatiji for his help in day-to-day work.

I gratefully acknowledge the financial assistance from Council of Scientific and Industrial Research (CSIR) for providing research fellowship to carry out the doctoral work. I would like to thank Dr. Prachee Sathe, Director, Critical Care Medicines, Ruby Hall Clinic, Pune, for her support and encouragement.

Many thanks are also due to my friends, especially Rajamani (who was always there to help me in whatever the situation), Dr. Rahul Patil, Dr. Rahul Shingte, Dr. Shweta Pradhan, Dr. Prashant Karandikar, Mandar, Vikas, Ajay, Walunj, Ahire, Satish, Manisha and Manjusha Bhosale, Chetan and Rachna Ghag, Milind and Rahul Sardar, Mohan Belwalkar, Swapnil and Makrand Pednekar, Prashant Nikam, Manish, Abhay Brahme, Vijay Kadam, Shekhar, Hrushikesh, Vivek, Sachin Lalbegi, Yogesh Bhole, Santosh Kumbharkar, Harshada Lohokare, Yogesh, Jiten, Suresha, Shubhangi, Hemant, Sunita, Sandeep Kanawade, Santosh Hire, Ramesh, Bharate, Sangave, Ujjwal, Amit, Tope, Girish, Shailesh, Vipin, Kamendra, Nitin, Sunil, Deu, Ganesh, Sarika, Prakash, Abhimanyu, Arun Jagadale, Victor, Pandu, Ravi, Anand Bhansali, Manmohan Bajaj, Manmohan Kapoor, Abhilash, Amit, Pinku, D Nangre, Suhas, Subhash and Vishal Patil, Pawan, Prashant, Rajesh, Rajeev, Sachin Shukre, and K Shinde.

TABLE OF CONTENTS

Chapter 1: Introduction and Literature

Chapter 2: Experimental Details and Characterization Techniques

Chapter 3: PB/Clay Nanocomposites

Chapter 4: PB/Multiwalled Carbon Nanotubes Nanocomposites

Chapter 5: PB/Barium titanate ($BaTiO_3$) Nanocomposites

Chapter 6: Conclusions And Scope For Future Work

List of Publications

List of Figures

Chapter 1: Introduction and Literature

Chapter 2: Experimental Details and Characterization Techniques

Chapter 3: PB/Clay Nanocomposites

Chapter 4: PB/Multiwalled Carbon Nanotubes Nanocomposites

Chapter 5: PB/Barium titanate ($BaTiO_3$) nanocomposites

Chapter 6: Conclusions and Scope for future work

List of Tables

Chapter 1: Introduction and Literature

Chapter 3: PB/Clay Nanocomposites

Chapter 4: PB/Multiwalled Carbon Nanotubes Nanocomposites

Chapter 5: PB/Barium titanate ($BaTiO_3$) Nanocomposites

List of symbols

U^*	Activation energy (Growth rate equation)
ω	Angular frequency
a	Avrami – Ozawa exponent
n	Avrami exponent
ε^*	Complex permittivity
η^*	Complex Viscosity
ϕ	Cooling rate
$t_{1/2}$	Crystallization half time
T_c	Crystallization temperature
ε''	Dielectric loss
ε'	Dielectric permittivity
E''	Elastic loss modulus
E'	Elastic storage modulus
Ea	Energy of activation
G	Growth rate constant
T_∞	Hypothetical temperature below which all viscous flow ceases (T_g - 30 °C)
Φ	Nucleating Activity
K_g	Nucleation constant
G_0	Pre exponential factor
Z_t	Rate constant (modified Avrami equation)
X_t	Relative degree of crystallinity
G''	Shear loss modulus
G'	Shear storage modulus
t_c	Total crystallization time
R	Universal gas constant
F(T)	Value of cooling rate chosen at unit crystallization time

Nomenclature

CEC	Cation exchange capacity
CNT	Carbon nanotubes
DES	Dielectric Spectroscopy
DMA	Dynamic Mechanical Analysis
DSC	Differential Scanning Calorimetry
MMT	Montmorillonite
MWCNT	Multiwalled Carbon Nanotubes
OM	Optical Microscopy
SAXS	Small angle X – ray scattering
SEM	Scanning Electron Microscopy
SWCNT	Single Walled carbon nanotubes
TEM	Transmission Electron Microscopy
TGA	Thermogravimetric analysis
WAXS	Wide angle X – ray scattering
XRD	X – ray diffraction

Abstract

ABSTRACT

Poly(1-butene) PB is one of the members of polyolefin family. PB exhibits excellent mechanical properties superior to those offered by other members of polyolefin family. PB is a unique polyolefin with a number of properties that makes it an excellent choice as a pipe material. Another major application area for polybutene resins is seal-peel or easy-open packaging. It is also used in heavy-duty bags, pressure-sensitive tapes, agricultural films, gaskets, and diaphragms. However, its applications are limited compared to other polyolefins such as PE and PP because of the slow room temperature phase transformation, which complicates the production of goods with stable mechanical properties.

PB exhibits very complex polymorphic behavior and can crystallize in four crystalline forms depending on the conditions of crystallization and the presence of other components. After melting, PB crystallizes in the tetragonal crystal Form II having 11_3 helix and then it transforms into stable twined hexagonal crystal Form I of 3_1 helix. As a result, the chain packing is improved with a substantial increase in the density from 0.90 g/cc to approximately 0.95 g/cc. These structural changes are also associated with significant changes in the thermal and mechanical properties. Form I melts at 125-138°C, whereas; Form II melts at low temperature at about 110-120 °C. The phase transformation of Form II into Form I start soon after the crystallization of Form II and generally completes in about ten days.

Crystallization of PB is of great interest because of its spontaneous, kinetically favored phase transformation in solid state. Various techniques have been used such as DSC, WAXS, and hardness measurement to study the kinetics of phase transformation. Effects of addition of nucleating agents, and blending with other polyolefins on the crystallization and kinetics of phase transformation have also been studied.

A revolutionary work by Okada et al synthesizing nylon/clay nanocomposites and by Iijima synthesizing carbon nanotubes, initiated a lot of interest in fundamental as well as industrial research in the area of nanocomposites. Subsequent studies in polymer nanocomposites revealed that very small amount of nanofiller is required for achieving significant improvement in material properties such as, modulus, strength, heat resistance, and flame retardancy. These nanofillers are also reported to act as nucleating agents and help in enhancing the crystallization rates. However, till date no report was available on the use of nanofillers for accelerating the phase transformation behavior of PB. It was therefore decided to study the nanocomposites of PB based on various nanofillers with special emphasis on the crystallization and phase transformation.

In this work, the nanocomposites of PB are successfully prepared by melt compounding technique and characterized for the first time. Different nanofillers such as clay, MWCNT and $BaTiO_3$ nanoparticles are used for this purpose. The structure, morphology, crystallization, crystal-to-crystal phase transformation and thermo-mechanical behavior of the nanocomposites are studied.

The PB/clay nanocomposites show intercalated structures with uniform dispersion of clay layers in the polymer matrix. The SEM micrographs for PB/MWCNT nanocomposite exhibit dispersion of bundles of MWCNTs in the matrix, while in PB/$BaTiO_3$ nanocomposites uniform dispersion of $BaTiO_3$ nanoparticles with some agglomerates of the size about 1-4 μm are observed.

The crystallization studies reveal enhanced crystallization rates for non-isothermal as well as isothermal crystallization for nanocomposites with all the nanofillers. The non-isothermal crystallization studied using modified Avrami and combined Avrami-Ozawa theory signify enhanced crystallization rates as evidenced by the higher values of Z_t and lower values of $t_{1/2}$ and F(T) for the nanocomposites as compared to PB. The nucleating activities of the nanocomposites are found less than 0.9 for all the nanocomposites, suggesting active surface for crystallization. It is observed that the MWCNTs have more active surface for crystallization than clay and $BaTiO_3$ nanoparticles.

In isothermal crystallization, the total crystallization time against the temperature is plotted to compare the effect of nanofillers. The total crystallization time (t_c) is found lower as compared to pristine PB, indicating heterogeneous nucleation of PB in presence of nanofillers, and MWCNT is found to be more effective than clay and $BaTiO_3$ nanoparticles. As can be seen form the optical micrographs, well-defined spherulitic morphology is observed for pristine PB and PB/Barium titanate nanocomposite, but a disturbed morphology is observed for nanocomposites prepared using clay. The nanocomposites with MWCNT exhibited very small and disordered crystallites. The dynamic mechanical analysis shows improved storage modulus for all the nanocomposites compared to pristine PB, but the highest improvement is found for PB/MWCNT nanocomposites. The thermogravimetric analysis indicates enhanced thermal stability for all nanocomposites while the incorporation of MWCNTs results in significant increase in the degradation initiation temperature. The important aspect of this study is the kinetics of phase transformation from metastable tetragonal form (Form II) to stable twinned hexagonal form (Form I). The half time for phase transformation (50% conversion to Form I) of PB is about 58 hrs and it is significantly increased for PB/MWCNT nanocomposites. The clay and MWCNTs are found to be more effective in enhancing the phase transformation rate than $BaTiO_3$ nanoparticles.

Our results demonstrate that the clay, MWCNT, and $BaTiO_3$ nanoparticles provide active nucleation sites for the crystallization but MWCNT play a significant role in enhancing the overall properties of PB.

Signature of the Candidate Signature of the Research Guide

Santosh D Wanjale Dr. (Mrs.) Jyoti P Jog

Chapter 1

Introduction and Literature

1.1 Introduction:

This chapter presents an overview of crystallization, crystal-to-crystal phase transformation and thermo-mechanical properties of poly(1-butene) (PB). The inspiration behind the study of PB nanocomposites is discussed. A literature review comprising of various methods of synthesis of nanocomposites, use of different nanofillers and effect of these nanofillers on the structure, morphology, crystallization, thermomechanical, and dielectric properties of the polymer matrix is presented. The objectives of the present study are also discussed.

1.2 Poly(1-butene) (PB):

1.2.1 Synthesis, Properties, and Applications:

PB was first synthesized in 1954 and Hüls started its industrial production in 1964. Mobil Oil in the US built a small industrial plant in Louisiana. It was then taken over by Witco Chemical Corporation in 1970. In 1977 Shell Chemicals US, a subsidiary of Shell Oil Company, acquired the PB business from Witco. In 1998, the management of the polybutene portfolio was put in the hands of Shell's subsidiary Montell Polyolefins. Two years later in October 2000, Montell Polyolefins merged with Targor GmbH and Elenac GmbH to form Basell Polyolefins. [1]

PB is one of the members of polyolefin family. It is synthesized by polymerization of butene-1, with a stereo-specific Ziegler-Natta catalyst to produce a linear, high molecular weight and isotactic semi-crystalline polymer. Figure 1.1 shows the molecular structure of PB. PB combines the typical properties of conventional polyolefins with some characteristics of engineering polymers. As a result, it exhibits excellent mechanical properties superior to those offered by other members of polyolefin family. Due to structural similarity, PB is compatible with PP. It can be used in blends to improve certain characteristics of PP. On the other hand, PB is not compatible with PE. PB copolymers are blended in PE film grades for use in peelable packaging.

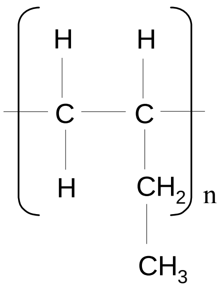

Figure 1.1: Molecular structure of poly(1-butene)

Properties:

The processability of PB is not affected by the high molecular weight and can be processed with conventional plastics manufacturing equipments. The melt strength is about twice as high as for PP, which results in better drawability and less sagging of the melt during extrusion. The rheological behavior is very non-Newtonian, which means that the melt viscosity is shear-dependent. PB is more sensitive to shear and orientation than other polyolefins. PB is easily weldable. Various joining techniques such as socket welding, butt-welding and electro-fusion welding are commonly applied for pipe installation.

The peculiar tensile behavior of PB is based on the chain entanglements (Long molecular chains act as a link between the crystalline domains). PB has an excellent burst pressure resistance, no sensitivity to stress cracking, good impact strength, good abrasion resistance, and retention of mechanical properties even at temperatures close to the melting point. PB homopolymers are more flexible than PP random copolymers and crosslinked PE. The flexibility remains high even at low temperatures and allows easier handling during cold seasons. PB resists well to impact. The IZOD notched impact strength (ISO 180) of PB is classified “no break” at room temperature. PB resist to creep when submitted to multi-axial strain like in a pressurized pipe. PB homopolymer is a very flexible and soft material for a pipe grade. Its elastic recovery is excellent even though it is not crosslinked. The compression set at 23 °C is about 55 %, and at 70 °C about 64 %, according to ASTM D395-89, method B.

The wet abrasion resistance of PB is excellent in sand/slurry type conditions. It performs as good as Ultra high molecular weight polyethylene (UHMW-PE), which is well known for its outstanding abrasion and wear resistance. In dry conditions, however, PB does not meet the high performance of UHMW-PE.

PB is even used as an additive in blend to improve the environmental stress crack resistance (ESCR) of certain PE grades. The addition of 2-5 % PB-1 improves the stress crack resistance significantly.

Being a polyolefin, PB possesses excellent chemical resistance. It is resistant to most acids, bases, detergents, oils, fats, alcohol, ketones and aliphatic hydrocarbons. PB is sensitive to oxidizing acids, aromatic and chlorinated hydrocarbons [1].

Applications:

PB is a unique polyolefin with a number of properties that make it an excellent choice as a pipe material, evidenced by its continuing market acceptance growth in both Europe and Asia.

PB homopolymers are used for various applications such as outdoor, indoor water distribution; hot and cold water transport, and industrial/chemicals radiator connections. Ease of handling and fast installation of PB pipes is determined by its light-weight, flexibility (even at cold ambient temperatures), low memory effect and the variety of available jointing techniques. Pipe fittings can be molded from the same resin. The variety of jointing techniques permits the production of a complete all-plastic piping network with homogenous connections. Another major application area for polybutene resins is seal-peel or easy-open packaging. It is also used in heavy-duty bags, pressure-sensitive tapes, agricultural films, gaskets and diaphragms. In applications where high impact resistance is required at low temperature, PB is preferred over iPP and PMP. However, its applications are limited compared to other polyolefins such as PE and PP because of the slow room temperature phase transformation, which complicates the production of goods with stable mechanical properties [1].

1.2.2 Polymorphism:

PB exhibits very complex polymorphic behavior and can crystallize in four crystalline forms depending on the conditions of crystallization and the presence of other components. The characteristics of the various forms and their chain conformations are presented in Table 1.1. After melting, PB crystallizes in the tetragonal crystal Form II with 11_3-helix and then it transforms into stable twined hexagonal crystal Form I of a 3_1 helix. As a result, the chain packing is improved with a substantial increase in the density from 0.90 g/cc to approximately 0.95 g/cc. These structural changes are also associated with significant changes in the thermal and mechanical properties. Form I melts at 125-138 °C whereas; Form II melts at low temperature at about 110-120 °C. The phase transformation of Form II into Form I start soon after the crystallization of Form II and generally completes in about ten days. The third form with an orthorhombic unit cell with a 4_1 helix can be obtained by precipitating the polymer from various solvents. It melts at about 100 °C. The fourth form is I′ with untwined hexagonal form of a 3_1 helical structure and it melts at 90 –100 °C [2].

Table 1.1: Crystalline forms of PB [2]

Form	Crystal Lattice	Helix	Unit cell dimensions (nm)	T_m (°C)	Density (g/cc)
I	Hexagonal (Twinned)	3_1	a = b = 1.77, c = 0.65	125-138	0.95
I'	Hexagonal (Untwined)	3_1	a = b = 1.77, c = 0.65	90-100	----
II	Tetragonal	11_3	a = b = 1.46, c = 2.12	110-120	0.90
III	Orthorhombic	4_1	a = 1.25, b = 0.89, c = 0.76	90-100	0.90

1.2.3 Crystal to crystal phase transformation:

Crystallization of PB is of great interest because of its spontaneous, kinetically favored phase transformation in solid state. Various techniques have been used to study the kinetics of phase transformation and are summarized in the following section.

Differential scanning calorimetry (DSC) is commonly used to study the phase transformation of PB. Since the melting points of the two forms are easily distinguishable, the melting of each form can be monitored using DSC. The melting point of Form II is observed at 110-115°C, whereas, Form I exhibits a melting peak at 125-138°C [3-5].

Wide angle X - ray diffraction (WAXD) is widely used to study the kinetics of phase transformation [6]. Marigo et al [7] have studied the phase transformation by monitoring the wide angle X – ray scattering (WAXS) patterns at different time intervals, as the crystalline Form I and Form II are easily distinguishable from the diffraction patterns. The rate of phase transformation was studied by estimating the ratio of the peak areas i.e. A_t/A_0, where A_t is the area under the peak at 2 theta value of 12° (corresponding to 200 reflection of Form II) at time t and A_0 is the area of the same peak crystallized immediately after melting. They [7] also used the SAXS patterns to study the phase transformation.

The hardness values of Form I are remarkably higher than that of Form II because of the dense chain packing in Form I. Azzurri et al [8] used hardness measurement by microindentation technique to study the crystal-to-crystal phase transformation at room temperature. The rate of transformation was found to be independent of molecular weight. Authors also observed a relationship between half time of transformation and the degree of crystallization. The increase in transformation rates with decrease in fraction of amorphous material was explained on the basis of the role played by taut tie molecules at the crystal-amorphous interphase, which favored the helix extension required for the phase transformation.

Effects of addition of nucleating agents, and blending with other polyolefins on the crystallization and kinetics of phase transformation have been studied. The nucleating agents such as pimelic acid, azelaic acid, the quinacridone dye permanent red E3B, and the mixture of calcium carbonate and pimelic acid, was found effective in accelerating the isothermal crystallization and phase transformation in PB. Amongst these E3B, calcium carbonate- pimelic acid mixture was most efficient as reported by Zhang et al. [9].

Kaszonyiova et al [10] studied the isothermal crystallization and phase transformation kinetics of PB at various temperatures. It is reported that the crystallization rate increased by 100% in presence of sodium salicylate while with talc it unexpectedly decreased by about 300%. The most important observation of this study was that the nucleating agents had no effect on the phase transformation rate.

Differential thermal analysis was used to study the effect of α-chloronaphthalene, diphenyl ether, glycerin and carbon black on crystal-to-crystal phase transformation of PB. α-chloronaphthalene and diphenyl ether were found to accelerate the transformation while glycerin and carbon black were found to be ineffective. The differences in the results were attributed to the variations in the ability to create defects, which would aid in the nucleation and possibly the growth of the new crystalline phase [11]. Sodium benzoate and stearic acid were effective in enhancing the rate of phase transformation, whereas addition of (1- naphthylacetamide) a known nucleating agent did not increase the rate when added about 0.1% [12].

The phase transformation in PB/HOCP blends is studied by Canetti et al [13]. Authors found that the transformation kinetics was influenced by the molecular mobility of the system after crystallization. The HOCP, which is melt compatible at the molecular level with PB produced an amorphous phase with reduced molecular mobility in the blends. The rate of phase transformation was found to decrease as a result of addition of HOCP at low aging temperatures up 313 °K.

Shieh et al [14] studied the crystallization and phase transformation kinetics for the solution precipitated blends of PP with PB. PB in PP rich compositions crystallized in crystal Form I', which then transforms to Form II on dynamic heating or cooling. The rate of phase transformation was improved only in PB rich compositions, due to the similar helix conformation of α form of PP and form I' and I of PB. Hong et al [12] reported that the mechanical blending of PP (5-10 % by wt.) resulted in acceleration of crystallization as well as rate of phase transformation process.

Hong et al [12] also examined the effects of cold rolling, orientation produced in film blowing and some additives on the rate of phase transformation by XRD and density measurements. They observed that the cold rolling was an effective method as it causes rapid partial transformation to Form I followed by further transformation at enhanced rates. The molecular orientation induced during melt processing was also found to enhance the rate of transformation. A special attempt was made by Beatty et al [15] to enhance the phase transformation rate by increasing the tie molecules or tie fibrils population by controlling the crystallization process. They claimed that the major effect of variation of the crystallization conditions was the change in the number of interactions of crystalline segments with the amorphous phase. Choi et al [16] reported that the filaments having higher level of crystalline orientation showed higher rate of phase transformation.

Effect of certain parameters on the rate of phase transformation such as, Pressure,[5] temperature, [17] and mechanical deformation [2] is also studied.

The transformation of Form II to Form I was accelerated by the application of pressure of only few hundred bars while at high pressures Form I' was observed [5]. The degree of phase transformation at different temperatures increased almost linearly with time and maximum rate of increase was observed at 40 °C to 50 °C [17]. The tensile drawing of Form III at 80 °C produced an oriented tape with unstable Form II which spontaneously transformed into Form I, however drawing at 70 °C yielded an oriented tape with Form I' [2].

1.3 Inspiration:

A revolutionary work by Okada et al [18] synthesizing nylon/clay nanocomposites and by Iijima [19] synthesizing carbon nanotubes, initiated a lot of interest in fundamental as well as industrial research in the area of nanocomposites. Subsequent studies in polymer nanocomposites revealed that very small amount of nanofiller is required for achieving significant improvement in materials properties such as, modulus, strength, heat resistance, and flame retardancy. These nanofillers are also reported to act as nucleating agents and help in enhancing the crystallization rates.

As discussed in the previous sections, a lot of work has been reported, wherein, use of nucleating agents, blends, mechanical deformation and fillers for accelerating the rate of phase transformation was attempted; However, till date no report was available on the use of nanofillers for accelerating the phase transformation behavior of PB. It was therefore decided to study the nanocomposites of PB based on various nanofillers with special emphasis on the crystallization and phase transformation.

1.4 Nanocomposites:

In materials research, the development of polymer nanocomposites is rapidly emerging as a multidisciplinary research activity that could expand the applications of polymers. Polymer nanocomposites are being considered as an alternative to conventional composites. As the composites are synthesized using micron size reinforcements, the nanocomposites constitute nanometer size particles (nanoparticles). Improvements in stiffness, barrier to diffusion, optical transparency and thermal stability are obtained in the polymer nanocomposites. These improvements are not only due to the small size of the particles, which results in high surface area but also due to shapes, and aspect ratios of the fillers. In case of nanocomposites, a very small amount of nanofillers (5% by weight) is required for achieving significant improvements in materials properties. Crystallization in case of semi-crystalline polymers is also found to be influenced by the addition of the nanofillers. In short, the improvements in the inherent properties of the polymer matrix are achieved without sacrificing the processibility and mechanical properties of polymers at very low percentage loading of the nanofillers.

One can categorize these nanofillers as follows:

* Fillers having one dimension in nanoscale - Clays

* Fillers having two dimensions in nanoscale – Nanotubes and Nanowhiskers

* Fillers having three dimensions in nanoscale - Nanoparticles

1.4.1 Clays:

Clays are hydrous aluminum silicates and are generally classified as phyllosilicates. These consists of natural clays like montmorillonite, hectorite, and saponite as well as synthetic clays such as magadite, mica, laponite, flourohectorite, etc. Montmorillonite is a principal clay mineral of Bentonite rock, which originates from volcanic ash. Bentonite is a rock, which consists of commonly known Smectite or Montmorillonite group clays as major component and auxiliary minerals such as kaolin, quartz, gypsum, iron ore etc. Sodium or calcium bentonite is not itself a mineral name, but more correctly, it is Smectite clay composed primarily of the mineral Montmorillonite having sodium or calcium ions as its predominant cations in the layers. Smectite or Montmorillonite group clays are further classified into two sub–groups, viz. trioctahedral and dioctahedral Smectite clays. In dioctahedral clays, two out of three cation positions in the octahedral sheet are filled, every third position being vacant; this type of sheet is called as gibbsite. In trioctahedral clay minerals, all three octahedral positions are occupied; this type of sheet is called as brucite. Montmorillonite, Beidilite and Nontronite are dioctahedral Smectite clays whereas Hectorite and Saponite are trioctahedral Smectite clays. Clay minerals are also further classified by their arrangement of tetrahedral and octahedral sheets.

1) *1:1 clay minerals* contain one tetrahedral and one octahedral sheet per clay layer; this type of clay is having basal spacing of 0.7 nm, examples, Kaolinite and Serpentine.

2) *2:1 clay minerals* contain two tetrahedral sheets with an octahedral sheet between them with a basal spacing of 1.0 nm; examples include pyrophyllite, talc and montmorillonite.

3) *2:1:1 clay minerals* contain an octahedral sheet that is adjacent to a 2:1 layer with basal spacing of 1.4 nm, for example Chlorite.

Among these layered silicates, Montmorillonite (MMT) is mostly used for the synthesis of polymer/clay nanocomposites because of its high stiffness, surface area, aspect ratio and ion exchange capacity.

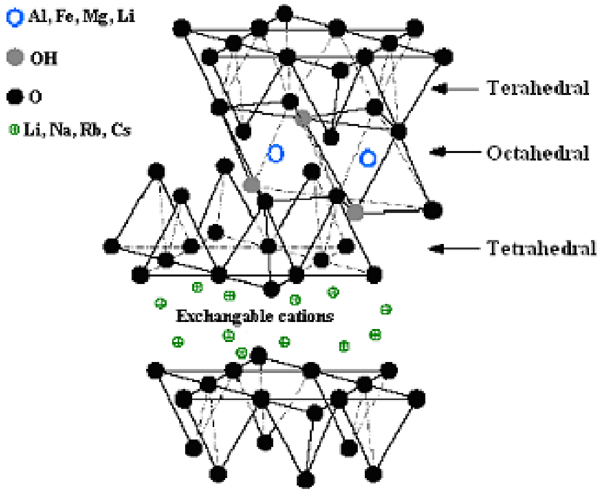

Figure 1.2: Schematic representation of clay platelet [20]

The schematic structure of the MMT is shown in Figure 1.2. The structure of MMT consists of two fused silica tetrahedral sheets and an edge-shared of either magnesium or aluminum hydroxide sandwiched between them. These layers are frequently described as "stacks of cards" or "layers of cards" to better describe their unique structure and form [20].

The layer thickness is around 1 nm and the lateral dimension of these layers may vary from 30 nm to several microns and even larger depending on the particular silicate. These layers organize themselves to form stacks with a regular van der Waals gap in between them called interlayer or gallery. Isomorphic substitutions within the layers (for e.g., Al^{3+} replaced by Mg^{2+} or Fe^{2+} replaced by Li^{+}) generate negative charges that are counter balanced by alkali or alkaline earth cations situated in the interlayer. Interlamellar complexes of clay minerals are formed by the introduction of inorganic and organic materials between the structural layers. The relatively weak bonding between the layers as compared with the strong ionic-covalent bonding within the layers facilitates complex formation.

The formula of an idealized unit cell of sodium form of montmorillonite is $Na_{0.67}$ $[Al_{3.33}Mg_{0.67}]$ $[Si_8]$ O_{20} $(OH)_4$ in which one of every 6–octahedral Al^{3+} has been replaced by Mg^{2+}. The charge deficit is 0.67 esu per unit cell, or 0.67 equivalent charge per 734 g (formula weight) of clay. This gives value of 91.3 milliequivalents (meq) charge deficit in layer per 100 g of clay. This deficiency of charge must be balanced by equal quantity of cation charge at its surface for electrical neutrality. The maximum amount of any one cation that can be taken up by particular clay is constant and is known as the cation exchange capacity (CEC) of that clay. The amount is expressed in milliequivalent (meq) per 100 g of dry clay. CEC varies from 80–100 depending up on the substituted cation. Due to isomorphous substitution for M^{3+} by M^{2+} and M^{2+} by M^{+} in its structure, bentonite clay has unique nature of cation exchange and adsorption capacity. The adsorption efficiency of bentonite is enhanced several folds after purification and/or modification.

As the hydrophilic-layered silicates are incompatible with most of the polymers, the inorganic cations in the galleries of the pristine clay are exchanged by tallow compounds/surfactants (organic moieties), which make the clay organophilic and improve the interactions with the polymer matrix. The variety of organic compounds are used for this purpose such as, quaternary ammonium compounds (quaternaries), amines, alkaloids, purines, nucleosides, proteins, etc.

1.4.2 Carbon nanotubes:

Carbon nanotubes are the graphite (hexagonal lattice of Carbon) sheets forming cylindrical shape, reported by Iijima in 1991. Nanotubes naturally align themselves into ropes held together by van der Waals forces.

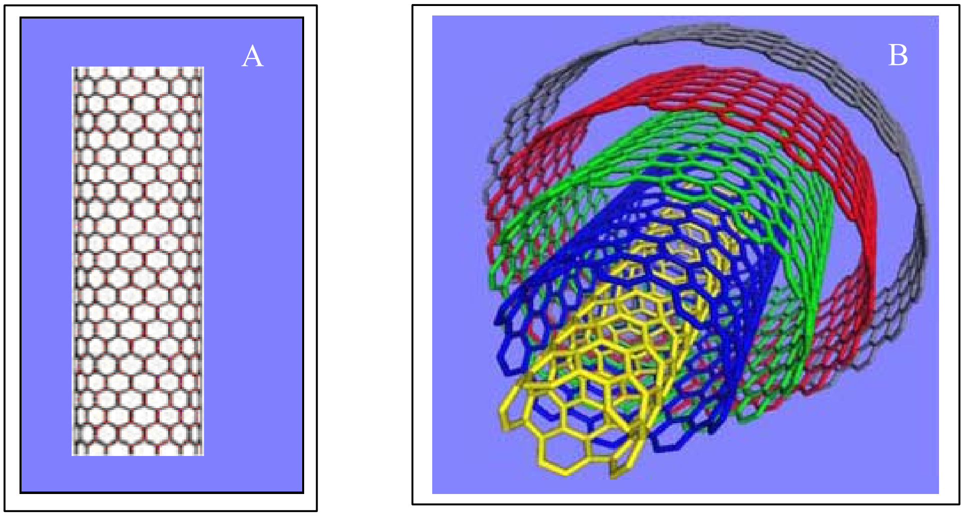

Figure 1.3: Schematic representation of carbon nanotubes, Single walled (A) multiwalled (B)

CNTs are classified according to the number of cylindrical sheets as single, double, and multiwalled. The schematic of SWCNT and MWCNT is shown in Figure 1.3. CNTs have very broad range of thermal, electronic, elastic and structural properties depending on different kind of nanotubes.

MWCNTs are reported to exhibit lower mechanical properties as compared to those of SWCNTs [21]. However, MWCNTs can be produced in much larger quantities and thus can be used for large-scale applications.

The unique structure and properties of carbon nanotubes offer promising potential for developing novel, smart, and advanced materials [21-24]. Various methods used for synthesis of CNTs are described as follows.

Arc discharge: In this technique a high current electric arc is passed through graphite electrodes in the presence of catalytic particles to form CNTs. Soot also forms with the CNTs. The production of SWCNT and MWCNT is highly dependent on the specific metal catalytic particles used for the synthesis [19, 25].

Laser ablation: Laser Ablation is a costly method that produces SWCNTs by focusing a laser on carbon containing small amount of transition metal target in an Argon atmosphere. This gives yield of around 70%. The SWNT having uniform diameter are produced. A continuous flow of mobile gas for example Argon is used to move the product [26].

Chemical vapor deposition (CVD): CVD is one of the promising synthetic methods for production of CNTs. This method involves decomposition of C_2H_2 over SiO_2 supported Fe catalysts to produce very long CNTs (2 mm). The synthesis apparatus consists of quartz tube reactor inside a combined preheater and furnace set up. The reaction temperature varies from 600-1000°C. Fe, Co and Ni metals are used for the synthesis. Nanotubes produced by this method are of high purity compared to other methods [27-28].

Properties of carbon nanotubes

Mechanical properties: Carbon nanotubes possess SP^2 carbon-carbon bonds because of which they have high stiffness and axial strength. The linear elastic modulus of the CNTs was studied by measuring the amplitude of the natural thermal vibrations in a transmission electron microscope and the Young modulus was found to be 1.8 TPa [29].

Electrical properties: Electrical properties of the CNTs depend upon the tube structure. The conductivity of a single walled carbon nanotube is reported as much as eight times higher than that of copper and thus can exhibit semi-conducting as well as metallic character [30]. These can be used as junctions between metal-semiconductor, semiconductor-semiconductor, and metal-metal. These junctions can be used for building various parts of nanoscale devices [31].

Thermal properties: The specific heat and thermal conductivity of the nanotubes can be determined by the Phonons. The temperature dependence specific heats of MWCNT and bundles of SWCNT are reported by Mizel et al [32]. The results showed that for SWCNTs, the specific heat was higher than that of graphite while the specific heat of MWCNTs was comparable to that of graphite below 50°K.

Applications of CNTs

CNTs are considered as promising materials in the various fields such as; field emission [33], molecular electronics [34], strength enhancing filler material [35], hydrogen storage

[36], molecular sieves [37], and heat transfer [38]. These nanotubes can also be used to prepare ultrahigh strength and lightweight composite materials for aerospace applications [39]. The single walled carbon nanotubes could be used as an artificial scaffold for the growth of bone tissues due to the high strength, flexibility, and low density. The CNT coatings might enhance the performance of the thermal detectors, which are used for high accuracy optical and thermal radiometry [40].

1.4.3 Nanoparticles:

Inorganic nanoparticles, such as, $CaCO_3$, SiO_2, Al_2O_3, ZnO, $BaTiO_3$, [41-45] and the metal nanoparticles, including, Cu, Ag, and Au [46-48] are being used for the nanocomposite synthesis.

Nanoparticles are synthesized by number of methods, such as, Wet chemical, Chemical vapor deposition, Sonication, UV and Microwave irradiation, Laser ablation, and by Biological methods.

Wet Chemical: This process involves number of methods, such as, Sol-gel, Hydrothermal, Solvothermal, and Reduction in solvent. In Hydrothermal method, the precursors dispersed/dissolved in water and then heated at high temperatures and pressures. The solvothermal process utilizes a solvent under high temperature and pressure above its critical point to increase the solubility and reaction rates. In reduction in solvent method, the reducing agents such as Sodium borohydride [49], hydrazine [50], Hydroxylamine hydrochloride [51], glucose [52], and long chain amines [53] are dissolved in the precursor solution. The power of the reducing agent had a direct effect on the size, shape, quantity, and quality of the nanoparticles.

Microwave synthesis: Very recently microwaves are used to synthesize nanoparticles. The microwave irradiation causes rapid volumetric heating and the reaction rates are tremendously increased. Komarneni et al [54] synthesized silver nanoparticles using two liquid phases by microwave irradiations.

Biological methods: Many living species can be used for the synthesis of the nanoparticles by the reduction method. Sastry et al [55] used fungus Verticillium for the synthesis of various nanoparticles with size less than 25 nm. Dokken et al [56] have discovered that Alfa-Alfa plants are able to uptake several heavy metals and reduce them into the nanoparticles.

Laser ablation: This is a very versatile method for the synthesis of nanoparticles for the top down approach. A laser is used to excite the bulk material placed in solution environment (Aqueous or organic) and provide a reactive species that agglomerates into the nanoparticles [57].

Chemical Vapor deposition: In this approach, vapor phase precursors are brought into a hot wall reactor under conditions that favor nucleation of particles in the vapor phase. The precursors can be solid, liquid, or gas at ambient conditions but it reaches to reactor as the vapor phase. Various methods, such as, Solvated Metal Atom Dispersion (SMAD) [58], photoreduction [59] and ultrasonication [60-61] are also used for the synthesis of various nanoparticles.

Applications of nanoparticles:

Nanoparticles are being designed for the various types of sensors. These are being used as catalysts having far better properties than their bulk counterparts. The inherent properties of the nanoparticles can be used for the synthesis of novel polymer nanocomposites or advanced materials. Nanocomposites based devices such as light emitting diodes; photovoltaic solar cells, photodiodes, and gas sensors have been developed. Polymer nanocomposites synthesized using Fe_3O_4 exhibited superparamagnetism for some ranges of concentration, particle sizes, shapes, and temperatures. These can be used for the future magnetic media storage materials [62].

The conduction mechanism through a semiconductor nanoparticle chains provides the basis for the manufacture of highly sensitive gas and vapor sensors and these sensors can combine the properties of the polymer matrix with those of the nanoparticles. The polymer nanocomposites containing nanoparticles of various properties, shapes, and sizes can be used for the neural networks applications as well as in optoelectronics and optical computing.

1.5 Methods for the Synthesis of nanocomposites:

Synthesis of nanocomposites is generally carried out by three major methods, viz., *in situ polymerization*, *solution blending*, and *melt compounding* for any type of nanofiller viz. clay, nanotubes or nanoparticles. The detail synthesis of nanocomposites, classified according to the nanoscale dimensions of nanofillers, described in following sections.

Polymer/clay nanocomposites:

Okada et al [18] synthesized first polymer/clay nanocomposites by *in situ* polymerization using nylon and Na^+ montmorillonite modified by amino acids. The pristine clay is hydrophilic and needs to be modified by the organic moieties to make it organophilic for better dispersion in the polymer matrix. The organomodified clays are prepared by reacting more voluminous organic onium cations with the montmorillonite clay. The reaction results in the exchange of relatively small sodium ions with organic counter ions. This ion exchange results into increase of the clay interlayer space, enabling organic cation chains to move in between them and secondly, the surface properties of each clay sheet are changed from being hydrophilic to hydrophobic. Synthesis of polymer/clay nanocomposites involves mainly three approaches. The first one is the ***in situ*** **polymerization**, in which the clay is swollen or intercalated by the monomers in the galleries. These clay layers then set apart by the polymerization of the intercalated monomers and the exfoliated structures can be obtained. Various polymer nanocomposites have been synthesized using this method, such as, PP, PE, PMMA and PS [63-65].

The second method for the synthesis is **solution intercalation** method. In this method the clay layers are swollen or dispersed in a particular solvent in which the polymer also have high solubility. The clay suspension and the polymer solutions are made separately, then mixed together while stirring, and again kept for homogeneous mixing for definite time. The nanocomposites are obtained either by precipitation method or by solvent evaporation. The ABS/clay nanocomposites is synthesized by precipitation method, while PEO/clay nanocomposites prepared by solvent evaporation method [66-68].

The third method is **melt intercalation** method, this process is most attractive for industrial applications in which clay and polymer are mixed under shear at temperatures higher than the melting/softening point of the polymer. Various nanocomposites based on polyolefins, polyesters, and thermoplastic elastomers [69-74] are prepared by this method.

Polymer/carbon nanotubes nanocomposites:

Ajayan et al [75] synthesized first polymer/CNT nanocomposites using liquid epoxide base resin and multiwalled carbon nanotubes. Carbon nanotubes such as SWCNTs and MWCNTs are used for the synthesis of nanocomposites resulting significant improvement in mechanical, thermal, viscoelastic properties and overall performance of the various polymers. The most important limitation of the pristine CNTs is the strong van der Waals forces, which lead to agglomeration and very poor solubility in many solvents and hinder the potential applications in various fields. Good interfacial interactions are required between CNTs and polymer matrix for efficient load transfer and hence improvement in properties.

The non-covalent and covalent methods are used for the modification of CNTs to improve their dispersion and interactions with the polymer matrix. In non-covalent modifications, surfactants [76-77], polymer wrapping [78-79] and polymer absorption [80-81] are used. The covalent functionalization of CNTs is generally carried out by nitrating mixture or nitric acid to generate carboxylic acid groups on the surface, which can be modified by different organic reactions. The various functional groups have been attached to the surface of CNTs to improve the interactions includes, radicals [82], aryl radicals [83], aryl cations [84], hydrogen [85], fluorine [86], nitrenes [87], and carbenes [88].

***In situ* polymerization** of a monomer in presence of pre-treated (modified) CNTs is the most significant method to produce nanocomposites with highly dispersed nanotubes. It has been employed for preparation of nanocomposites of polyimide [89], PMMA [90], polyaniline [91-92], and polyurethane [93].

Solution blending is another method for better dispersion of CNTs. Pre-treated CNTs initially dispersed in the solvent and then polymer solution is mixed with stirring, after solvent is evaporated the nanocomposite films are formed which can be dried in vacuum oven. PAN/SWCNT and UHMWPE/MWCNT nanocomposites have been synthesized by this method [94-95].

Melt mixing is an industrially important as well as environment friendly process, as it does not involve solvents. The pristine or chemically modified CNTs (SWCNT/MWCNT) are mixed with polymer matrix under shear above the melting temperature of the polymer. PMMA/MWCNT and PP/MWCNT composites prepared by melt compounding method [96-97].

Polymer/nanoparticle nanocomposites:

The nanoparticles of metals, semiconductors, and metal oxides are mainly used in the synthesis of these nanocomposites. There are four different approaches found in the literature. (1) In ***graft polymerization*** technique, the nanofillers are dispersed in the monomer or the monomer solution, and this suspension then polymerized to form the nanocomposite. PMMA/Silica nanocomposites are prepared by this method [98]. (2) In ***sol-gel*** technique, the metal alkoxide mixed with monomers or the polymer bearing functional groups, which can react with the hydroxyl groups, formed due to hydrolysis of alkoxide thus forming homogeneous polymer metal nanocomposites. A lot of research has been carried out on the hybrid materials syntheses by hydrolysis of metal oxides and the polycondensation with the polymer. Mostly acrylic polymer hybrids are synthesized by this method [99- 104]. (3) The **solution casting,** in which the nanoparticles are dispersed in a suitable solvent while the polymer dissolved in same solvent and then polymer solution is mixed in the nanoparticle suspension. The polymer nanocomposites films are prepared by solvent evaporation or precipitation method. PVA/Fe_2O_3 nanocomposites prepared by solution casting method [105]. (4) In **melt blending** process, the direct mixing of the nanoparticles with the polymer matrix is carried out. Nylon 6/silver nanoparticle nanocomposites prepared by melt compounding [106].

1.6 Structure and morphology of Nanocomposites:

Polymer/clay nanocomposites:

In polymer clay nanocomposites, X - ray diffraction (XRD) is used as a main tool to get the information on the structure of the nanocomposites formed. A study of relative positions, shape and intensity of the basal reflections are useful in determining the structures. Figure 1.4 illustrates different possible structures for polymer/clay nanocomposites.

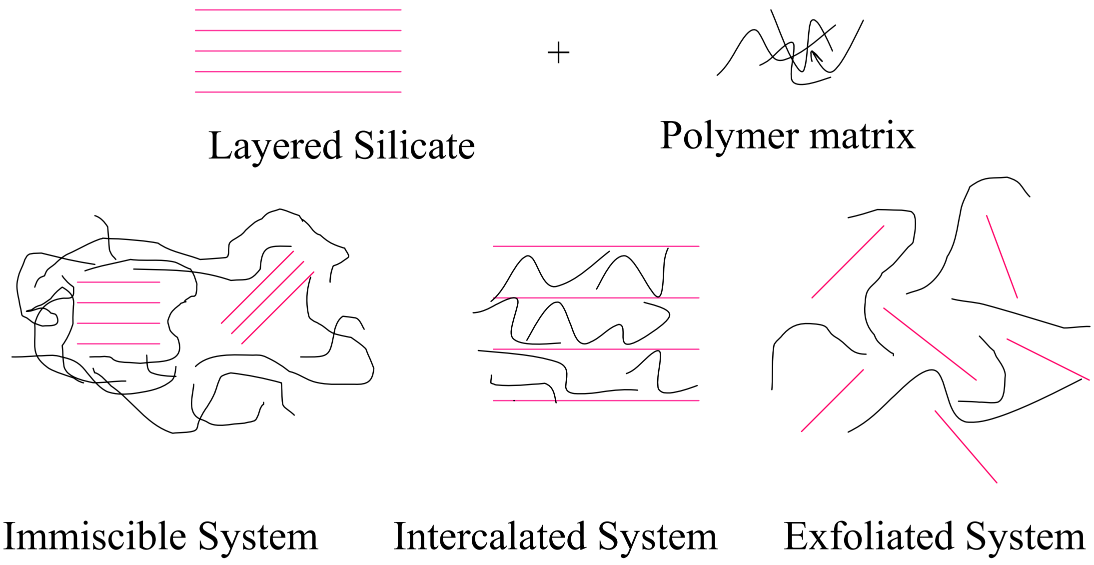

Figure 1.4: Schematic representation of possible structures in nanocomposites

Generally in immiscible structures, the characteristic basal spacing of the layered silicate doesn't change. In the intercalated nanocomposites, finite layer expansion takes place and results in new diffraction peaks of larger ‘d’ spacing. In exfoliated structures, the coherent stacking of the silicate layers is completely disturbed and featureless diffraction pattern is obtained.

Vaia and Liu [107] have shown that XRD also can be used as a tool to find the layer correlation such as crystallite size and disorder of the clay in the nanocomposites. TEM is an extremely useful technique, especially in the *XRD silent* nanocomposites. It gives a direct evidence of the structure and a definitive description of the spatial correlation such as distribution and inhomogenieties of the nanocomposites. TEM can be used to calculate the aspect ratio of the clay layers dispersed in the polymer matrix. XRD and TEM are complementary techniques in the structure evaluation of nanocomposites.

Polymer/carbon nanotubes nanocomposites:

X - ray diffraction technique can be used to evaluate the alignment of nanotubes in the polymer matrix. The diffraction patterns in two directions (perpendicular and parallel to the plane of film) can be used to evaluate the alignment of the nanotubes in the polymer matrix. [108]. Jin et al [109] showed that the (002) peak intensity is not constant with the azimuth angle ϕ but it is concentrated at two spots centered at different azimuth angles such as 90° and 270° when the nanotubes are aligned by mechanical stretching.

The dispersion level of the nanotubes in the polymer matrix can be evaluated by TEM. Nanocomposites of poly(styrene co-butyl acrylate) with MWCNTs exhibited good dispersion without any aggregation in the matrix. Authors also observed that the CNTs became shorter and less entangled compared to the bulk sample [108].

SEM is also a good technique to see the dispersion of CNTs in the polymer matrix. At lower percentage of SWCNTs, more uniform dispersion of bundles with few aggregates is observed. However, if the content of CNT increased, larger amount of CNTs self organized into bundles and forms more aggregates, as reported by Manchado et al [110].

Polymer/nanoparticle nanocomposites:

TEM is used to evaluate dispersion of nanoparticles in the polymer matrix. In case of PP/$CaCO_3$ nanocomposites a better dispersion was observed for concentration of $CaCO_3$ less than 9.2 vol%. While above this concentration a significant agglomeration was observed due to the coalescence of these nanoparticles because of their high surface energy [111].

SEM is used to study the dispersion of nanoparticles in case of PANI/$BaTiO_3$ nanocomposites. A composition dependent morphology was observed by Pant et al. [112]. Micron and nano size Cu particles were used for the synthesis of Cu/LDPE nanocomposites. The SEM for micron size composites showed much higher aggregates compared to nano size Cu composite. It has been also seen that the microvoids originated in the interface between the micron size Cu particles and matrix were much larger than microvoids originated in case of composites with nano size Cu particles [113].

1.7 Properties of Nanocomposites:

1.7.1 Crystallization Behavior:

Polymer/clay nanocomposites:

Incorporation of nanofillers in the polymer matrix results in significant changes in crystallization kinetics, spherulitic morphology, and polymorphism of the polymers. The role of clay particles in the crystallization study of polymer matrix has shown various results. The crystallinity of the PP was found to be increased with the addition of clay particles for in situ polymerized PP [114], while a decrease in crystallinity was found for exfoliated LLDPE/clay nanocomposites [115]. Clay particles enhanced the crystallization rate in some of the polymer clay system, such as PE-g-MA/clay nanocomposites [116]. The decrease in spherulitic size was observed with increasing clay content, which indicated that clay particles act as nucleating agents for (PP-MA)/clay nanocomposites [117]. Jog et al [118] have shown enhanced crystallization rates, decrease in crystallization half time for PP/clay nanocomposites prepared by melt intercalation technique, while Solomon et al [119] reported a retardation in crystallization for PP/clay nanocomposites. The presence of clay particles is also reported to have significant effect on the polymorphism of various polymers. Priya et al [120] reported a change in crystalline form in PVDF/clay nanocomposites for the first time. The pristine PVDF is found to crystallize in α form, while PVDF in PVDF/clay nanocomposites crystallized in the β form. Excess of γ-form of the crystallite of PP-MA is found in presence of clay, because of the confinement of the polymer chains between the clay particles [117]. It is also reported that the clay induced some orientation of α-phase PP crystallites in PP/clay nanocomposites [121]. In PP/clay nanocomposites, the nucleation activity is greatly enhanced in shear-induced crystallization and resulted in a drastic decrease in spherulite sizes of PP matrix [122].

Polymer/carbon nanotubes nanocomposites:

In case of sPP/MWCNT nanocomposites, crystallization temperature is significantly enhanced with the content of CNT. The crystallization rate constant increased and the half time of crystallization reduced remarkably [123]. Kodjie et al [124] reported the heterogeneous nucleation for both non-isothermal and isothermal crystallization of nanocomposites, and enhanced crystallization kinetics for HDPE/CNT nanocomposites compared to pure HDPE. The crystallization kinetics analysis showed a significant increase in activation energy on incorporating nanotubes for PP/SWCNT nanocomposites [125]. In case of PE/SWCNT nanocomposites, nanotubes provide nucleation sites to PE and accelerate the PE crystal growth rate while reducing the crystal dimensionality from spherulitic to disk-shaped as reported by Haggenmueller et al [126]. Octadecyl amine modified SWCNT promoted growth of the less-preferred β form of crystalline polypropylene at the expense of the α form [127]. On the contrary, the SWCNT displayed a nucleating effect on the PP crystallization, favoring the α crystalline form rather than the β form [125]. The "shishkebab" morphology was observed for UHMWPE/SWCNT nanocomposites. The polymer chains tend to crystallize from solution as chain-folded crystals i.e. Kebab, while the nanotube surface acts as nucleating site ie. Shish [128]. The crystallization kinetics was strongly affected by the presence of SWCNT at low concentration and the observed enhanced nucleation was ascribed to the dispersion of SWCNT offering high surface for nucleation in PP/SWCNT nanocomposites [129].

Polymer/nanoparticle nanocomposites:

Introduction of nanoparticles in the polymer matrix brings about significant effects on the crystallization, spherulitic morphology, and crystalline polymorphs. Nanocomposites synthesized using calcium carbonate ($CaCO_3$) nanoparticles displayed higher crystallinity compared to pristine PP [130]. A decrease in crystallinity is observed in case of LDPE/Cu nanocomposites [131]. Nanocomposites prepared using various nanoparticles such as Zinc (Zn) [132], Alumina (Al_2O_3) [43], and Calcium phosphate ($Ca_3(PO_4)_2$) [133] exhibited decrease in spherulitic size of PP. Nanoparticles such as $CaCO_3$ [134], TiO_2 [135], Al_2O_3 [43] induced a beta (β) crystalline form in PP nanocomposites. A long and twisted nature of lamellar morphology is observed for LDPE/Cu nanocomposites [136]. Crystallization of isotactic polypropylene (iPP) containing nano structured polyhedral oligomeric silsesquioxane (POSS) molecules showed faster crystallization rate for iPP-POSS nanocomposites than that for neat resin in quiescent as well as sheared states [137].

1.7.2 Dynamic mechanical thermal analysis:

Dynamic mechanical thermal analysis (DMTA) measures the response of a given material to a cyclic deformation as function of temperature and frequency. DMTA results are expressed in terms of three parameters, namely, the storage modulus (E'), loss modulus (E"), and tan δ. E' corresponds to energy stored elastically and reversibly, E" corresponds to the energy loss irreversibly and the tan δ is the ratio of E" to E'.

It is generally observed that the addition of nanoclay increases the storage modulus of the nanocomposites. PP nanocomposites exhibited a substantial improvement in E' with increasing clay content, especially in the rubbery regime (above T_g). The storage modulus E' was found to be almost three times than that of pristine PP for nanocomposite with 8 wt% clay [138]. The increase in storage modulus for other polymers such as PE, PMP, PVDF, PMMA, PTT, PETG, PCL, PEO, PEN, Epoxy, Polyamides, and Polyimides have been reported [139-150]. DMTA can be used to get the information on glass transition temperature of the system. PP nanocomposites synthesized by two step process. The organophilic clay was treated with MA and the melt mixed with PP. This melt mixed PP compound was then used to prepare nanocomposites. These nanocomposites showed increase in glass transition temperature by about 30°C. This was attributed to the restriction inside the clay galleries on the motion or the relaxation of molecular chains. [151]. In another study, PP nanocomposites were prepared using co-intercalated organophilic clay. Although the incorporation of clay layers resulted in substantial increase in storage modulus, the glass transition temperature was found to decrease up to certain clay loading. [152]. The effects of layered silicates and the compatibilizer on the various transitions such as α, β, and γ were studied by DMTA for LDPE/clay nanocomposites, and it was found that all the three transitions are affected by clay exfoliation level [153].

Low loadings of MWCNTs found to be more effective at increasing the storage modulus in PE/MWCNT nanocomposites. About 60% increment was found at only 0.5% MWCNT content. However, at higher loadings, an increase in modulus was found to be lowered [154].

In case of PC/MWCNT nanocomposites, two tan δ peaks were observed at 156.6°C and at about 180.0°C for more than 7% CNT content. Authors suggested that the lower tan δ peak (156.6°C) corresponds to the glass transition temperature of PC while the higher tan δ peak (180.0°C) corresponds to the confined PC chains by MWCNTs [155].

In Nylon 6/MWCNT (0-2wt%) nanocomposites the glass transition temperature remained almost same as that of pristine Nylon 6 probably due to the less constraints from CNTs imposed on the molecular chains [156].

For LLDPE/nano-SiO_2 nanocomposites the storage modulus E' and loss modulus E" of LLDPE increased and the α transition peaks of the composites shifted to the lower temperatures for untreated as well as for aminetriethoxysilane treated SiO_2 [157]. In case of PVAc, P4VP, PMMA and PS the introduction of silica nanoparticles induced the development of two different glass transition temperatures; the higher relaxation peak was ascribed to the immobilized matrix phase around the filler surface [158].

1.7.3 Melt rheology:

Rheology provides information about the processibility and the microstructure of the composite. Rheology can be used as a characteristic technique to complement TEM and XRD. The dispersion level of the reinforced nanofillers can be understood from the flow properties of the nanocomposites at various temperatures and frequencies.

The rheological response for Polystyrene/clay nanocomposites was studied to reveal the dispersion level of clay particles in the polymer matrix by Zhao et al [159]. The pristine polystyrene and the nanocomposites with low clay content gave a typical terminal relaxation behavior for polymer ($G' \sim \omega^2$, $G'' \sim \omega$). As the clay content increased, the terminal relaxation regime was changed (G' and $G'' \sim \omega$). For higher level of dispersion, the G' and G" spectra showed more solid like behavior. On further increase in clay dispersion, the G' was found to be greater than G" at all frequency range studied showing percolated network structure.

The dynamic frequency tests were carried out for Polyethylene/MMT (modifier used was dimethyl dialkyl ammonium halide) nanocomposites prepared by melt compounding. The complex viscosity (η^*) increased substantially at low frequencies and the Newtonian plateau disappeared at higher clay content. The effect was very clear for the PE-g-MA nanocomposites as compared for the uncompatibilized one. The tan δ for PE-g-MA nanocomposites also decreased significantly over the frequency range studied. On the other hand, a marginal decrease was observed for uncompatibilized PE nanocomposite [160].

The incorporation of CNTs in the polymer matrix is reported to increase the viscosity of the matrix significantly. The interconnected structures of the nanotubes have been observed in dynamic measurements by a plateau in a G' or G" versus frequency plots. However, the effect was more pronounced for G' than G". As the nanotube concentration increased the nanotube - nanotube interactions play important role to form the percolated network (interconnected structures of the nanotubes). Various percolation thresholds have been reported for different systems. The PC/MWCNT nanocomposites exhibited percolation threshold at 2 wt% [161] while for PE/MWCNT [154] it was at about 7.5 wt%, whereas for PMMA/SWCNT it was about 0.12 wt% [162]. For UHMPE/SWCNT nanocomposites the percolation threshold was observed at 0.6 wt% loading [163].

Inorganic fillers such as $CaCO_3$, SiO_2, and $BaTiO_3$ etc have been used in polymer nanocomposites to improve mechanical, thermal, and physical properties of the matrix. The flow properties of these reinforced polymer nanocomposites are sensitive to structure, particle shape, size and surface characteristics of the filler. The dispersion state of these nanoparticles in the polymer matrix and the particle/polymer and particle/particle interactions has been evaluated using rheological studies. A pseudo-solid like behavior in the low frequency range is attributed to the polymer adsorption on the filler surface that results in a transient network or entrapped entanglements [164-166] hence the dynamics of these adsorbed matrix is quite different from the bulk one and leads to increase in viscosity and concomitantly storage modulus [167]. Surface modification of nanoparticles is found to result in decreased viscosity and dynamic modulus of the polymer [168-170].

Osman et al [171] studied the rheological nature for polyethylene composite prepared with surface treated and untreated colloidal calcium carbonate. They have reported that as the content of $CaCO_3$ increased, the crossover frequency shifted to lower values indicating an increase in molecular relaxation time. This was attributed to the topological constraints to the reptation of polymeric chains leading to more chain stiffness and energy dissipation. Above a certain percentage of filler, G' and G" became frequency independent in the lower frequency region indicating pseudo-solid like behavior in the composites. In another report, Zhou et al [172] studied the nanocomposites of PDMS with $CaCO_3$. At the low filler loading, the nanocomposites exhibited a liquid like behavior at low frequency while at higher frequency the increase in G' was larger than G" suggesting solid like behavior. It is interesting to note that the crossover frequency shifted to higher values, as the content of $CaCO_3$ increased. They suggested that these suspensions become more elastic due to formation of nano $CaCO_3$ filler network.

1.7.4 Thermal Stability:

The thermal stability of the nanocomposites is studied using thermo-gravimetric analysis (TGA). Zhang et al [173] reported about 10 to 13°C increase in the degradation initiation temperature for LDPE nanocomposites prepared using various nanoclays. Authors also stated that for some polymers such as polystyrene there was large increase in onset of degradation temperature while for polyamide 6 there was no change. Yang et al [174] reported a slight reduction in the onset degradation temperature for PP/clay nanocomposites. This was due to the catalytic role played by the clay layers as explained by the Hoffmann reaction, which might accelerate the charring at the beginning of degradation process. Authors also reported that the organically modified MMT (OMMT) and the preparation methods influenced the thermal stability.

Dondero et al [175] have reported about 80°C increase in thermal stability for PP/MWCNT nanocomposites with just 3% MWCNT content, prepared by melt compounding. In HDPE/SWCNT, nanocomposites the thermal stability increased by about 70 °C in nitrogen atmosphere and 115 °C in air [124]. The thermal degradation and flammability properties of PP/MWCNT nanocomposites have studied by Kashiwagi et al [176]. The presence of nanotubes in PP/MWCNT nanocomposites modifies thermal and oxidative degradation processes of PP and significantly reduces the heat release rate of PP.

Xia et al [46] have studied the thermal stability of Cu/LDPE nanocomposites and microcomposites, the thermal decomposition temperature of the nanocomposites was found to be higher than pristine LDPE. For UV irradiated PP/ZnO nanocomposites, due to the UV screening properties of ZnO nanoparticles, the onset degradation temperature of the nanocomposites was increased compared to pristine PP [177].

1.8 Objectives of the present investigations:

The objectives of the present study are two folds, first is to prepare the nanocomposites of PB with different nanofillers using simple melt compounding technique and the second is to study the effect of these nanofillers of the crystallization and crystal-to-crystal phase transformation of PB.

The nanofillers such as clay, multiwalled carbon nanotubes, and barium titanate nanoparticles are used for this purpose. The work involves study of crystallization, crystal-to-crystal phase transformation, thermal stability, and viscoelastic properties of the nanocomposites.

The foremost objectives of this study are:

- To synthesize Poly(1-butene) nanocomposites using various nanofillers, namely, clay, multiwalled carbon nanotubes, and barium titanate nanoparticles by melt compounding method.
- To study the effect of these nanofillers on crystallization and crystal-to-crystal phase transformation of PB at room temperature.
- To study the microstructure of the nanocomposites formed.
- To study the viscoelastic properties in the solid as well as melt state and the thermal stability.

Following techniques are used to characterize the nanocomposites:

- Structure evaluation of the PB/clay nanocomposites by X - ray diffraction analysis (XRD).
- Dispersion of clay in PB matrix using Transmission Electron Microscopy (TEM).
- Dispersion of multiwalled carbon nanotubes and barium titanate nanoparticles in PB matrix studied using Scanning Electron Microscopy (SEM).
- Melting, crystallization, and crystal-to-crystal phase transformation studies are carried out using Differential Scanning Calorimetry (DSC).
- Spherulitic morphology of PB and its nanocomposites is viewed using Optical Microscope (OM).
- Viscoelastic properties in the solid state by Dynamic Mechanical Thermal Analysis (DMTA).
- Viscoelastic properties in the melt state by Advanced Rheological Expansion System (ARES).
- Thermal stability by Thermogravimetric Analysis (TGA).

1.9 Structure of the thesis:

The entire research work is presented in six chapters.

Chapter one provides the details about properties of PB and inspiration behind to study the nanocomposites of PB. An overview of the literature on various polymer nanocomposites synthesized using different techniques and the effect of nanofillers on crystallization and thermo-mechanical properties of variety of polymers is presented. The scope and objectives of the present study are also discussed.

Chapter two explains in detail, the experimental procedures and various techniques used for the characterization of PB and its nanocomposites along with theoretical background for the analysis of the experimental data.

Chapter three presents the results of PB nanocomposites prepared using nanofiller having one dimension in nanoscale, Nanocor clay (Octadecylamine modified montmorillonite). Effect of clay loading on the structure, crystallization, phase transformation kinetics, and thermo-mechanical properties is studied.

Chapter four presents the results of PB nanocomposites synthesized using MWCNTs. The nanofiller MWCNT is having two dimensions in nanoscale. Crystallization, spherulitic morphology, and crystal-to-crystal phase transformation is studied.

Chapter five presents the results of PB nanocomposites, synthesized using barium titanate nanoparticles. The nanofiller is having three dimensions in nanoscale. Effect of nanoparticle loading on the morphology, crystallization, phase transformation kinetics, and thermo-mechanical properties is described.

In chapter six, the overall conclusions on the effect of nanofillers, on various properties of PB are presented and the scope for future work is discussed.

References:

[1] http://www.pbpsa.com/eng/tech-rawtyp.asp

[2] Nakamura K, Aoike T, Usaka K, Kanamoto T. Macromolecules, 32, 4975 **(1999)**

[3] Boor J, Mitchell J. Journal of Polymer Science: part A 1, 59 **(1963)**

[4] Armeniades C, Baer E. Journal of Macromolecular Science, B1, 309 **(1967)**

[5] Nakafuku C, Miyaki T. Polymer, 24, 141, **(1983)**

[6] Hsu C, Geil P. Journal of Macromolecular Science Physics, B25, 433 **(1986)**

[7] Marigo A, Marega C, Cecchin G, Collina G, Ferrara G. European Polymer Journal, 36, 131 **(2000)**

[8] Azzurri F, Flores A, Alfonso G, Balta Calleja F. Macromolecules, 35, 9069 **(2002)**

[9] Zhang X, Zhang X, Shi G. Thermochimica Acta, 205, 245 **(1992)**

[10] Kaszonyiova M, Rybnikar F, Geil P. J Macromol Sci Phys; B43, 1095 **(2004)**

[11] Rubin I. Journal of Polymer Science part A3, 3803 **(1965)**

[12] Hong K, Spruiell J, Journal of applied polymer science, 30, 3163 **(1985)**

[13] Canetti M, Romano M, Sadocco P, Seves A. Makromol chem 191, 1589 **(1990)**

[14] Shieh Y, Lee M, Chen S. Polymer, 42, 4439 **(2001)**

[15] Beatty C, Rogers C. Polym Prepr (Am Chem Soc Div Polym Chem), 18, 641 **(1977)**

[16] Choi C, White JL. Polym Eng Sci, 41, 933 **(2001)**

[17] Tanaka A, Sugimoto N, Asada T, Onogi S. Polym J 1975, 7, 529 **(1975)**

[18] Okada A, Fukushima Y, Kawasumi M, Inagaki S, Usuki A, Sugiyama S, Kurauchi T, Kamigaito O. US patent 4739007, April **1988**.

[19] Iijima S, Nature (London) 354, 56, **(1991)**

[20] Giannelis E, Krishnamoorti R, Manias E. Adv Poly Sci, 138, 107 **(1999)**

[21] Mitchell D, Lee S, Trofin L, Li N, Nevanen T, Soderlund H, Martin C. J. Am. Chem. Soc., 124, 11864 **(2002)**.

[22] Vasilios G, Vasilios T, Dimitrios G, Dimitrios P. Chem Mater, 17, 1613, **(2005)**

[23] Sreekumar T, Liu T, Min B, Guo H, Kumar S, Hauge R, Smalley R, Adv Mat, 16, 58 **(2004)**

[24] Sandler J, Shaffer M, Prasse T, Bauhofer Q, Schulte K, Windle A, Polymer, 40, 5967 **(1999)**

[25] Ebbesen T, Ajayan P, Nature (London) 358, 220, **(1992)**

[26] Thess A, Lee R, Nikolaev P, Dai H, Petit P, Robert J, Xu C, Lee Y, Kim S, Rinzler A, Colbert D, Scuseria G, Tomanek D, Fischer J, R.E. Smalley R, Science 273, 483 **(1996)**

[27] Yacaman M, Yoshida M, Rendon L, Santiesteban J, Appl Phys Lett, 62, 202 **(1993)**

[28] Ivanov V, Nagy J, Lambin P, Lucas A, Zhang X, Zhang X, Bernaerts D, Van Tendeloo G, Amelinckx S, Van Landuyt J. Chem Phys Lett, 223, 329 **(1994)**

[29] Wong E, Sheehan P, Lieber C. Science, 277(5334), 1971 **(1997)**

[30] Appenzeller J, Martel R, Derycke V, Radosavljevic M, Wind S, Neumayer D, Avouris P. Microelectronic Eng, 64, 391 **(2002)**

[31] Papapdopoulos C, Rakitin A, Li J, Vedeneev A, Xu J, Phys Rev Lett, 85, 3476 **(2000)**

[32] Mizel A, Benedict L, Cohen M, Louie S, Zettl A, Budraa N, Beyermann W. Phys Rev B 60, 3264 **(1999)**

[33] Zhu W, Kochanski G, Bower C, Zhou O, Kochanski G, Jin S. Applied Physics Letters, 75, 873 **(1999)**

[34] Bachtold A, Hadley P, Nakanishi T, Dekker C. Science, 294, 1317 **(2001)**

[35] Frankland S, Caglar A, Brenner D, Griebel M. Journal of Physical Chemistry B, 106, 3046 **(2002)**

[36] Lamari Darkrim F, Malbrunot P, Tartaglia G. International Journal of Hydrogen Energy, 27, 193 **(2002)**

[37] Wang Q, Challa S, Sholl D, Johnson J. Physical Review Letters, 82, 956 **(1999)**

[38] Osman M, Srivastava D. Nanotechnology, 12, 21 **(2001)**

[39] Stewart, R., Plastics Engineering, 60, 29 **(2004)**

[40] Lehman, J. and Dillon, A. Laser Focus World, 41,81 (2005)

[41] Weiping Z, Guangping Z, Jianyong Y, Gance D. Journal of Applied Polymer Science, 91, 431 **(2004)**

[42] Bikiaris D, Vassiliou A , Pavlidou E , Karayannidis G European Polymer Journal, 41, 1965 **(2005)**

[43] Zhao H, Robert K. Li Y. Journal of Polymer Science: Part B: Polymer Physics, 43, 3652 **(2005)**

[44] Jianguo T, Yao W, Haiyan L, Belfiore L. Polymer 45, 2081 **(2004)**

[45] Dang Z, Xu H, Wang H, Applied Physics Letters, **90**, 012901 **(2007)**

[46] Xia X, Cai S, Xie C. Materials Chemistry and Physics 95,122 **(2006)**

[47] Manna S, Batabyal S, Nandi A. J Phys Chem B**,** 110, 12318 (**2006)**

[48] Caseri W. Macromol Rapid Commun, **21,** 705 **(2000)**

[49] Hyning V, Zukoski D. Langmuir, 14, 7034 (**1998)**

[50] Tan, Y.; Jiang, L.; Li, T.; Zhu, D. J Phys Chem B, 106, 3131 **(2002)**

[51] Leopokld N, Lendl, B. J Phys Chem B, 107, 5723 (**2003)**

[52] Raveendran P, Fu J, Wallen S. L. J Am Chem Soc, 125, 13940 (**2003)**

[53] Hiramatsu H, Osterloh F. Chem Mater, 16, 2509 (**2004)**

[54] Gao F, Lu Q, Komarneni S. Chem Mater, 17, 856- 860. **(2005**)

[55] Mukherjee, P.; Ahmad, A.; Mandal, D.; Senapati, S.; Sainkar, S. R.; khan, M. I.; Parishcha, R.; Ajaykumar, P. V.; Alam, M.; Kumar, R.; Sastry, M. Nano Lett, 1, 515 **(2001)**

[56] Gardea-Torresdey J, Tiemann, K, Gamez G, Dokken K, Tehuacanero S, Jose-Yacaman, M. Journal of Nanoparticle Research, 1, 397 **(1999)**

[57] Mafune, F.; Kohno, J.; Takeda, Y.; Kondow, T. J Phys Chem B, 104, 9111 (**2000)**

[58] Stoeva S, Klabunde K, Sorensen C, Dragieva I. J Am Chem Soc**,** 124, 2305 **(2002)**

[59] Mallick K, Wang Z, Pal, T. Journal of Photochemistry and Photobiology A: chemistry, 140, 75 (**2001)**

[60] Mizukosi, Y.; Okitsu, K.; Maeda, Y.; Yamamoto, T. A.; Oshima, R.; Nagata, Y. J Phys Chem B, 101, 7033 **(1997)**

[61] Brown S, Im H, Rondinone A, Dai S. Journal of Colloid and Interface Science, 292, 127 **(2005)**

[62] Chung Y, Lim S, Kim C, Young-Ho Kim Y, Yoon C. Journal of Magnetism and Magnetic Materials, 272, e1167 **(2004)**

[63] Sun T, Garces J, Advanced Materials 14(2), 128 **(2002)**

[64] Ray S, Galgali G, Lele A, Sivaram S. Journal of Polymer Science, Part A: Polymer Chemistry, 43(2), 304 (**2005)**

[65] Zeng C, Lee L, Macromolecules, 34(12), 4098 **(2001)**

[66] Pramanik M, Srivastava S, Samantaray B, Bhowmick A, Journal of Polymer Science, Part B: Polymer Physics, 40(18), 2065 **(2002)**

[67] Pourabas B, Raeesi V, Polymer, 46, 5533, **(2005)**

[68] Shen Z, Simon G, Cheng Y, Polymer, 43, 4251(2002)

[69] Perrin-Sarazin F, Ton-That M, Bureau M, Denault J. Polymer, 46(25), 11624 **(2005)**

[70] Luyt A, Githamma V, Polymer Testing, 26, 461 **(2007)**

[71] Ray S, Okamoto K, Maiti P, Okamoto M, Journal of nanoscience and nanotechnology, 2, 1, **(2002)**

[72] Fornes T, Yoon P, Paul D. Polymer, 44, 7545 **(2003)**

[73] Sinha Ray S, Okamoto M. Macromolecular Rapid Communications, 24, 815 **(2003)**

[74] Shen Z, Simon G, Cheng Y, European Polymer Journal, 39, 1917 **(2003)**

[75] Ajayan P, Stephan O, Colliex C, Trauth D. Science, 265, 1212 **(1994)**

[76] Islam M, Rojas E, Bergey D, Johnson A, Yodh A. Nano Lett, 3, 269 **(2003)**

[77] Kang Y, Taton T. J. Am. Chem. Soc, 125, 5650 **(2003)**

[78] Star A, Stoddart, J. Macromolecules, 35, 7516 (**2002)**

[79] O'Connell M, Boul P, Ericson L, Huffman C, Wang Y, Haroz E, Kuper C, Tour J, Ausman K, Smalley, R. Chem Phys Lett, 342, 265 (**2001)**

[80] Gomez F, Chen R, Wang D, Waymouth R, Dai H. Chem Commun, 2, 190 (2003)

[81] Barraza H, Pompeo F, O'Rear E, Resasco D. Nano Lett, 2, 797 (**2002)**

[82] Ying Y, Saini R, Liang F, Sadana A, Billups, W. Org. Lett, 5, 1471 **(2003)**

[83] Bahr J, Yang J, Kosynkin D, Bronikowski M Smalley R, Tour J. J Am Chem Soc 123, 6536 **(2001)**

[84] Dyke C, Tour J. J Am Chem Soc, 125, 1156 (**2003)**

[85] Pekker S, Salvetat J, Jakab E, Bonard J, Forro L. J Phys Chem B, 105, 7938 (**2001)**

[86] Mickelson E, Huffman C, Rinzler A, Smalley R, Hauge R, Margrave J Chem Phys Lett, 296, 188 (**1998)**

[87] Holzinger M, Vostrowsky O, Hirsch A, Hennrich F, Kappes M, Weiss R, Jellen F. Angew Chem, Int. Ed., 40, 4002 (**2001)**

[88] Chen Y, Haddon R, Fang S, Rao A, Lee W, Dickey E, Grulke E, Pendergrass J, Chavan A, Haley B, Smalley R. J Mater Res, 13, 2423 (**1998)**

[89] Park C, Ounaies Z, Watson K, Crooks R, Smith J, Lowther S, Connell J, Siochi E, Harrison J, Clair T. Chemical Physics Letters 364, 303 **(2002)**

[90] Jia Z, Wang Z, Zhu S. Mater Sci Eng A, 271, 395, **(1999)**

[91] Philip B, Xie, J, Abraham J, Varadan V. Smart Materials and Structures 13, N105, **(2004)**

[92] Park S, Cho M, Jhon M. Macromol. Rapid Commun, 24, 1070 **(2003)**

[93] Wagner H, Lourie O, Tenne R. Appl Phys Lett, 72, 188 (**1998)**

[94] Sreekumar T, Liu T, Min BG, Guo H, Kumar S, Hauge R, Smalley R. Adv Mat,16(1), 58 **(2004)**

[95] Ruan S, Gao P, Yang X, Yu T. Polymer 44, 5643 **(2003)**

[96] Jin Z, Pramoda K, Xu G and Goh SH. Chem Phys Lett, 337, 43 **(2001)**

[97] Seo M, Park S, Chem Phys Lett, 395, 44, **(2004)**

[98] Kickelbick G. Prog Polym Sci 28, 83 **(2003)**

[99] Huang Z, Qiu, K. Polymer, **38**(3), 521 **(1997)**

[100] Huang H, Wilkes, G. Macromolecules, 20, 1322 **(1987)**

[101] Huang H, Wilkes, G. Polym. Bull, 18, 455 **(1987)**

[102] Fujita M, Honda K. Polym. Commun. 1989, 30, 200 **(1989)**

[103] Mauritz K, Ju R. Chem Mater, 6, 2269 **(1994)**

[104] Mascia L, Kioul A. Polymer, 36, 3649 **(1995)**

[105] Lagashetty A, Havanoor V, Mallikarjuna N, Venkataraman A. Asian journal of chemistry, 15, 1500 **(2003)**

[106] Chae D, Oh S, Kim B. Journal of Polymer physics, 42, 790 **(2004)**

[107] Vaia R, Liu W. Journal Polymer Science Part B: Polymer Physics, 40,1590 **(2002)**

[108] Dalmas F, Chazeau L, Gauthier C, Masenelli-Varlot K, Dendievel R, Cavaille J, Forro L. Journal of Polymer Science: Part B: Polymer Physics, 43, 1186 **(2005)**

[109] Jin L, Bower C, Zhou O. Appl Phys Lett 73, 1197 **(1998)**

[110] Manchado M, Valentini L, Biagiotti J, Kenny J. Carbon, 43, 1499 **(2005)**

[111] Weon J, Sue H. J Mater Sci 41 (8) 2291 **(2006)**

[112] Pant H, Patra M, Verma A, Vadera S, Kumar N. Acta Materialia, 54 3163 **(2006)**

[113] Xia, X, Xie C, Cai S, Wen F, Shu C, Yang X. Material Science and Engineering A 429, 329 **(2006)**

[114] Hwu J, Jiang G. Journal of Applied Polymer Science 95(5), 1228 (**2005)**

[115] Lew C, Murphy W, McNally G. Polymer Engineering and Science 44 (6), 1027 **(2004)**

[116] Gopakumar T, Lee J, Kontopoulou M, Parent J. Polymer 43, 20, 5483 (**2002)**

[117] Maiti P, Nam P, Okamoto M, Kotaka T, Hasegawa N. Usuki A. Polymer Engineering and Science 42(9), 1864 **(2002)**

[118] Hambir S, Bulakh N, Kodgire P, Kalgaonkar R, Jog J. Journal of Polymer Science, Part B: Polymer Physics 39(4), 446 **(2001)**

[119] Somwangthanaroj A, Lee E, Solomon M. Macromolecules 36(7), 2333 **(2003)**

[120] Priya L, Jog J, Journal of Polymer Science, Part B: Polymer Physics, 40(15), 1682, **(2002)**

[121] Perrin-Sarazin F, Ton-That M, Bureau M. Denault J. Polymer, 46 (25), 11624 **(2005)**

[122] Nowacki R, Monasse B, Piorkowska E, Galeski A, Haudin J. Polymer, 45(14), 4877 **(2004)**

[123] Wiemann K, Kaminsky W, Gojny F, Schulte K. Macromolecular Chemistry and Physics 206 (15), 1472 **(2005)**

[124] Kodjie S, Li L, Li B, Cai W, Li C, Keating M. J. Macro. Sci. B, Phys., 45, 231 **(2006)**

[125] Leelapornpisit W, Ton-That M, Perrin-Sarazin F, Cole K, Denault J, Simard B. Journal of Polymer Science, Part B: Polymer Physics, 43(18), 2445 **(2005)**

[126] Haggenmueller R, Fischer J, Winey K. Macromolecules 39(8), 2964 **(2006)**

[127] Grady B, Pompeo F, Shambaugh R, Resasco D. Journal of Physical Chemistry B106 (23) 5852 **(2002)**

[128] Zhang Q, Lippits D, Rastogi S. Macromolecules 39(2), 658, **(2006)**

[129] Valentini L, Biagiotti J, López-Manchado M, Santucci S, Kenny J. Polymer Engineering and Science 44(2), 303 **(2004)**

[130] Ma C, Rong M, Zhang M. Acta Polymerica Sinica 3, 381 **(2003)**

[131] Xia X, Xie C, Cai S. Thermochimica Acta 427, 129 **(2005)**

[132] Tang J, Wang Y, Liu H, Belfiore L. Polymer 45, 2081 **(2004)**

[133] Saujanya C, Radhakrishnan S, Polymer 42(16), 6723 **(2001)**

[134] Weon J, Sue H. Journal of Materials Science 41, 2291 **(2006)**

[135] Fuhe Cailiao Xuebao/Acta Materiae Compositae Sinica 22 (5), 100 (2005)

[136] Xia X, Cai S, Xie C. Materials Chemistry and Physics 95,122 **(2006)**

[137] Fu B, Yang L, Somani R, Zong S, Hsiao B,. Phillips S, Blanski R., Ruth, P. Journal of Polymer Science, Part B: Polymer Physics, 39 (22), 2727 **(2001)**

[138] Ma J, Qi H. Journal of Applied Polymer Science, 82, 3611 **(2001)**

[139] Lee J, Jung D, Hong C, Rhee K, Advani S. Composites Science and Technology, 65(13), 1996 **(2005)**

[140] Wanjale S, Jog J, Journal of Applied Polymer Science, 90(12), 3233 **(2003)**

[141] Priya L, Jog J, Journal of Polymer Science, Part B: Polymer Physics, 41(1), 31 **(2002)**

[142] Ryu J, Lee J, Kim H. Macromolecular Research, 10(4), 187 **(2002)**

[143] Liu Z, Chen K, Yan D. European Polymer Journal, 39(12), 2359 **(2003)**

[144] Kalgaonkar R, Jog J, Journal of Polymer Science, part B: Polymer Physics, 41(23), 3102 **(2003)**

[145] Lepoittevin B, Devalckenaere M, Pantoustier N, Alexandre M, Kubies D, Calberg C, Jerome R, Dubois P. Polymer 43(14), 4017 **(2002)**

[146] Ratna D, Divekar S, Samui A, Chakraborty B, Banthia AK Polymer 47(11) 4068 **(2006)**

[147] Chua Y, Wu S, Lu X. Journal of Nanoscience and Nanotechnology, 6(12), 3985

(2006)

[148] Chen C, Curliss D. SAMPE Journal 37(5), 11 **(2001)**

[149] Yoon K, Polk M, Min B, Schiraldi D. Polymer International, 53(12), 2072 **(2004)**

[150] Abdalla M, Dean D, Campbell S. Material Research Society Symposium Proceedings, 726, 179 **(2002)**

[151] Zhang Y, Lee J, Rhee J, Rhee K. Composite science and technology, 64,1383, **(2004)**

[152] Liu X, Wu Q. Polymer, 42, 10013 **(2001)**

[153] Lew C, Murphy W, McNally G. Polym Eng Sci 44,1027 **(2004)**

[154] McNally T, Pötschke P, Halley P, Murphy M, Martin D, Bell S, Brennan G, Bein D, Lemoine P, Quinn J. Polymer, 46, 8222 **(2005)**

[155] SungY, Kum C, Lee H, Byon N, Yoon H, Kim W. Polymer, 46, 5656 **(2005)**

[156] Liu T, Phang I, Shen L, Chow S, Zhang W. Macromolecules, 37,7214, **(2004)**

[157] Lew C, Murphy W, McNally G. Polymer testing, 23, 9 **(2004)**

[158] Preghenella M, Pegoretti A, Migliaresi C. Polymer, 46 (26), 12065 **(2005)**

[159] Zhao J, Morgan A, Harris J. Polymer, 46, 8641, **(2005)**

[160] Gopakumar T, Lee J, Kontopoulou M, Parent J. Polymer, 43, 5483**(2002)**

[161] Pötschke P, Fornes T, Paul D. Polymer, 43, 3247 **(2002)**

[162] Du F, Scogna R, Zhou W, Brand S, Fischer J, Winey K. Macromolecules, 37, 9048 **(2004)**

[163] Zhang Q, Lippits D, Rastogi S. Macromolecules, 39(2), 658-666, **(2006)**

[164] Eggers H, Schummer P. Rubber Chem Technol, 69, 253 **(1996)**

[165] Aranguren M, Mora E, DeGroot J, Macosko C. J Rheol, 36, 1165 **(1992)**

[166] Sternstein S, Zhu A. Macromolecules, 35,7262 **(2002)**

[167] Picu R, Ozmusul M. J Chem Phys 2003;118:11239., Vilgis TA. Polymer, 46, 4223 **(2005)**

[168] Suetsugu Y, White J. J Appl Polym Sci,28,1481 **(1983)**

[169] Sun L, Park M, Salovey R, Aklonis J. Polym Eng Sci, 32, 777 **(1992)**

[170] Malik T, Carreau P, Germela M, Dufresne A. Polym Compos, 9, 412 **(1988)**

[171] Osman M, Atallah A. Polymer, 47(7) 2357, **(2006)**

[172] Zhou Y, Wang S, Zhang Y, Zhang Y, Jiang X, Yi D. Journal of Applied Polymer Science, 101, 3395 **(2006)**

[173] Zhang J, Wilkie C. Polymer Degradation and Stability, 80, 163, **(2003)**

[174] Tang Y, Hu Y, Song L, Zong R, Gui Z, Chen Z, Fan W. Polymer Degradation and Stability, 82, 127 **(2003)**

[175] Dondero W, Gorga R. J Polym Sci B, Polym Phys, **44**, 864 **(2006)**

[176] Kashiwagi T, Grulke E, Hilding J, Harris R, Awad W, Douglas J. Macromol Rapid Commun, 23, 761 **(2002)**

[177] Zhao H, Li R. Polymer, 47, 3207 **(2006)**

Chapter 2

Experimental Details and Characterization Techniques

2.1 Introduction:

This chapter presents details of preparation of nanocomposites and the characterization techniques used for evaluating the various properties of the pristine polymer and its nanocomposites. The theoretical background for the analysis of the experimental data is also discussed.

2.2 Experimental:

2.2.1 Melt compounding:

The nanocomposites are prepared using melt compounding technique. Two types of equipments are used for this purpose. A Brabender Plasticorder batch mixer, having capacity 60g, (model PLE 330) is used for PB/clay nanocomposites compounding. A batch mixer is made up of a heated mixing head (WEH 50) containing a pair of sigma shaped roller blades, which are driven by a dynamometer at a controlled speed. The rotors are counter-rotating with a speed ratio of 2:3. Electric heaters controlled by Eurotherm PID are used for heating the mixer. The temperature accuracy is ± 1 ^{o}C. A Haake Polylab batch mixer having 50g capacity is also used for the compounding of nanocomposites of MWCNT and $BaTiO_3$ nanoparticles. The batch mixer is a Rheomix 600P equipped with roller rotors R600.

The melt compounding is carried out at 150 °C for 7 min at rotor speed of 60rpm. Three compositions with 3,5 and 7 wt% of clay and MWCNT while 5,7 and 10 wt% of $BaTiO_3$ is prepared and the samples are coded as PB3N, PB5N and PB7N for PB/clay nanocomposites, PB3C, PB5C and PB7C for PB/MWCNT nanocomposites and PB5B, PB7B and PB10B for PB/$BaTiO_3$ nanocomposites, respectivley.

2.2.2 Sample Preparation:

The films are prepared by compression molding using Carver press model F – 15181. An appropriate quantity of material is taken and heated above melting temperature between metal sheets, which are sprayed using mold release spray. Nominal pressure is applied to get the required thickness of the film. Platens of carver press are then cooled using water circulation. These films are used for further characterization.

2.3 Characterization techniques:

2.3.1 X-ray diffraction (XRD):

X- ray diffraction (XRD) is a non-destructive analytical technique for identification and quantitative determination of long-range order in various crystalline compounds.

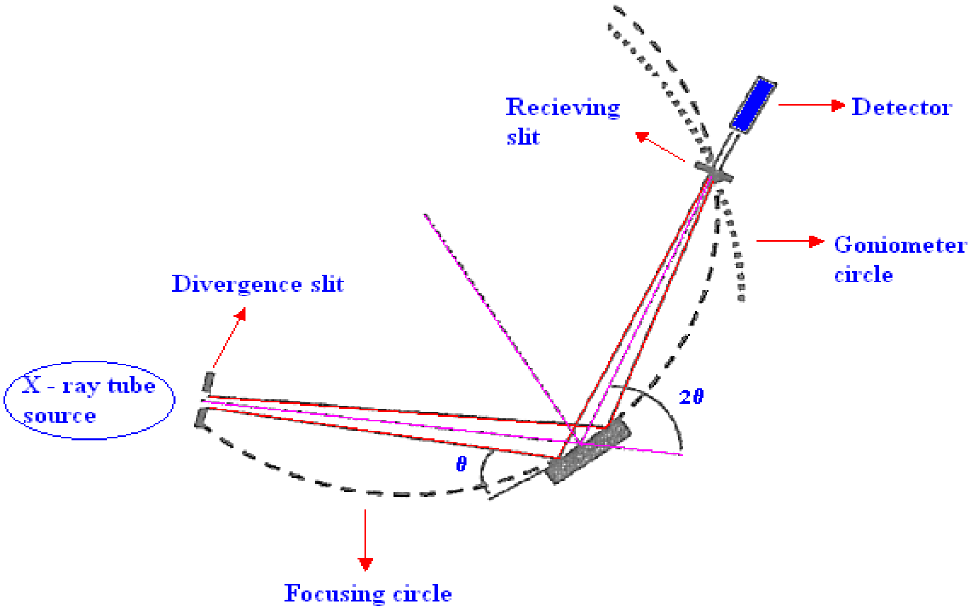

Figure 2.1: Bragg Brentano parafocusing geometry of XRD in reflection mode [2]

The basic components of the instrument are X - ray tube (X-ray generator), goniometer, detector, and the software. The X – rays are generated by bombarding the target with high-speed electrons. As the electrons collide the target atoms a continuous spectrum of

X - ray is emitted known as Bremsstrahlung radiations. According to Auger's theory, different wavelength such as K_α and K_β are generated. Copper and Molybdenum are commonly used targets that emit X - rays of wavelength 0.154 nm and 0.08 nm respectively. The mechanical assembly that makes up the sample holder, detector arm, and associated gearing is referred to as goniometer.

The working principle of a Bragg-Brentano parafocusing reflection goniometer is shown in Figure 2.1. For the Theta: 2-Theta goniometer, the X-ray tube is stationary, the sample moves by the angle Theta and the detector simultaneously moves by the angle 2-Theta. X-ray powder diffraction in the reflection mode (Bragg Brentano Parafocusing geometry) [1-2] as shown in the figure, is used to characterize the structure of polymer clay nanocomposites. Bragg presented a simple explanation of the diffracted beams from a crystal. The diffracted beams are found when the reflections from parallel planes of the atoms interfere constructively. Consider parallel lattice planes spaced at a distance d apart (Figure 2.2).

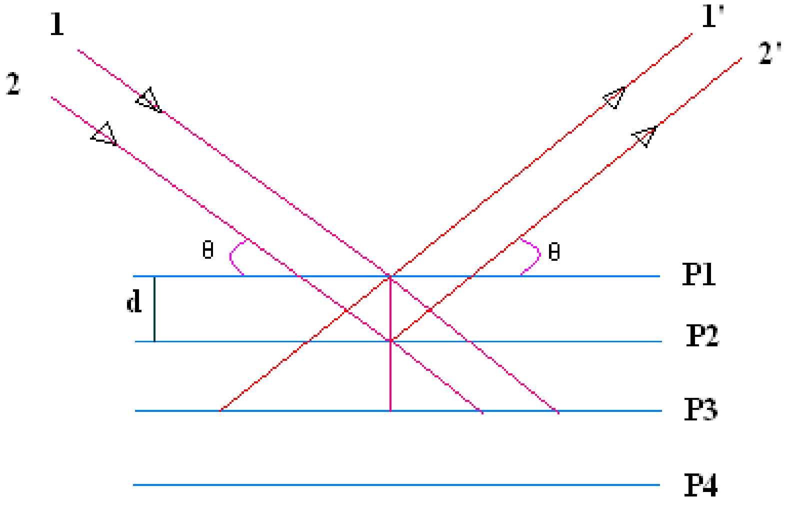

Figure 2.2: Principle of X-ray diffraction

The radiation is incident in the plane of the crystal lattice. The path difference for rays reflected from adjacent planes is 2d sinθ, where θ is measured from the plane. Constructive interference of the radiation from successive planes occurs when path difference is an integral multiple (n) of wavelength λ. Therefore,

$n\lambda = 2d \sin\theta$.

This is the Braggs law. Although the reflection from each plane is specular, for only certain value of θ, the reflection from all parallel planes add up in phase to give strong reflected beam. The Bragg's law is a consequence of periodicity of the lattice. It requires that θ and λ to be matched. To achieve this it is necessary to scan either wavelength or angle. X-rays are scattered by contrasting regions of electron density, which originate from voids, grain boundaries, density fluctuations, difference in electron density between crystalline and amorphous regions, etc., in materials.

The crystalline forms of polymer and the structure of nanocomposites is evaluated by performing wide-angle X-ray Diffraction (WAXD) experiments using a Rigaku model Dmax 2500 X-ray diffractometer. The system consisted of a rotating anode X - ray generator operated at 40 kV and 100 mA with a wide-angle goniometer.

2.3.2 Transmission Electron Microscopy (TEM):

The principle of electron microscope resembles that of the light microscope. However, the electron microscope differs from the light microscope in the usage of focused beam of electrons instead of light to acquire information about material composition and structure and to view the specimen. In an electron microscope, an electron source forms the stream of electrons and positive electric potential is used for its acceleration towards the specimen. Metal apertures and magnetic lenses are used to focus the stream of electrons and are then confined to a thin monochromatic beam. Magnetic lenses are intended to focus this monochromatic beam onto the sample. Electron beam gets affected by the interactions that happen within the irradiated sample. These interactions are then transformed into an image.

There are four main components of TEM viz, an electron optical column, a vacuum system, necessary electronics (lens supplies for focusing and deflecting the beam and the high voltage generator for the electron source) and the software. Schematic of TEM is shown in Figure 2.3.

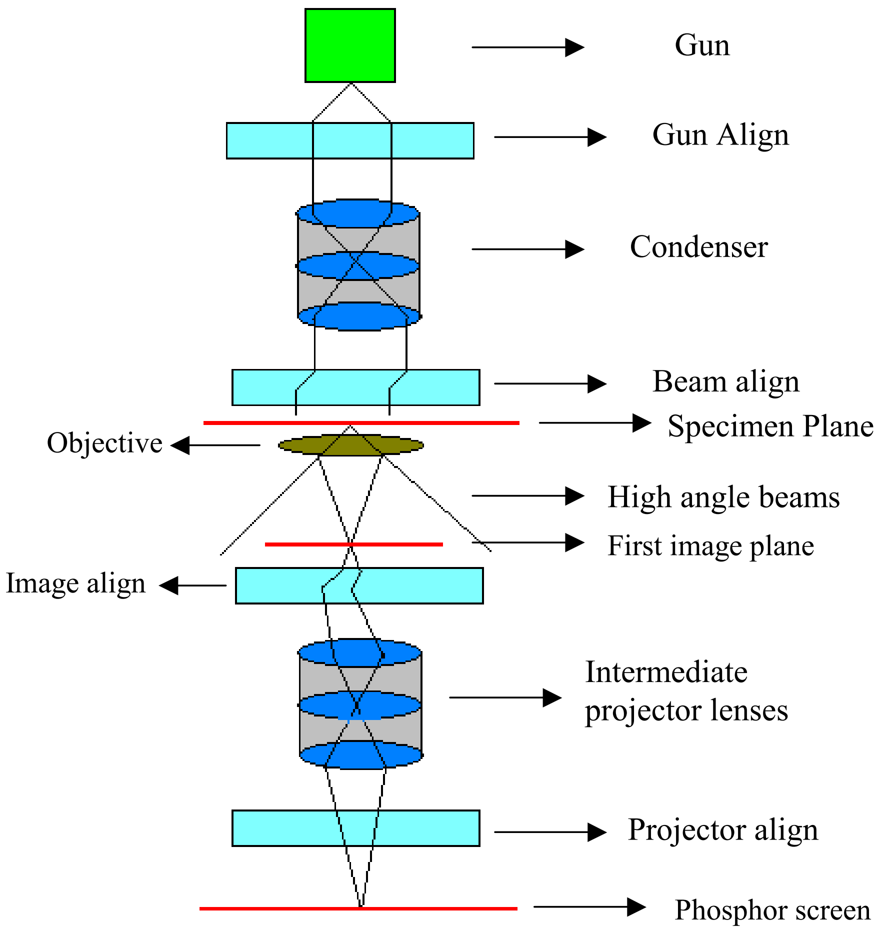

Figure 2.3: Schematic of Transmission electron microscopy

TEM specimen needs to be sufficiently thin of the order of 100 nm or less. In this thin area, only a few electrons are scattered and more than 90% of the incident beam is undeviated. Regions of the specimen, which are thicker, or of higher density will scatter the electron beam more strongly and will appear darker in the image. If the specimen is too thick, the number of electrons transmitted reduces and this reduces the contrast. Hence, the specimen thickness should be of the order of 100 nm or less.

The samples for TEM are prepared using a Leica Ultracut UCT microtome. Properly trimmed samples (of trapezoid shape having its lateral dimensions closer to 1mm) are placed in an arm, which is attached to a motor controlled hand wheel. As the arm moves vertically past the diamond knife, the sample is cut in the required thickness. These cut sections are collected on water surface, of a boat attached to the knife-edge. The cut sections are directly transferred to the grids and dried properly before being transferred to the TEM experimental setup. TEM images are observed using JEOL (JEM 1200 EX) apparatus.

2.3.3 Scanning Electron Microscopy (SEM):

In Scanning Electron Microscopy (SEM) an electron beam is used for the observation of the sample. A high vacuum is required as the electrons scattered more in the air atmosphere. Electrons in scanning electron microscopes are accelerated at voltages in the range of 2 to 40 kV. An electron beam < 0.01μm in diameter is focused on the specimen. These fast primary electrons (PE) interact in various ways with the surface layers of the specimen. Secondary electrons (SE), back scattered electrons (BSE), and absorbed electrons are produced, flowing off as specimen current. In addition, X-rays, Auger electrons, and cathodoluminescence are produced. The surface of a specimen is brought into the focus of electron beams. The signals produced control the brightness of a screen tube such that an image of the surface of the sample appears. The samples should be electrically conductive, otherwise, it may get overcharged due to the irradiations. The schematic for SEM is shown in Figure 2.4. The main component of SEM consists of an electron gun, (cathode – Wehnelt cylinder – anode), lens system (lenses, apertures, beam deflection coils and stigmator coils) and the specimen chamber.

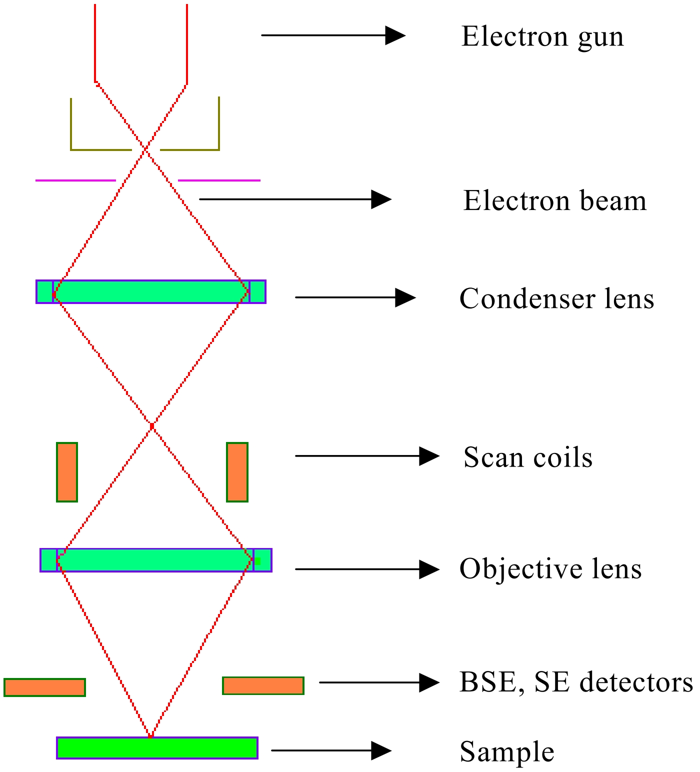

Figure 2.4: Schematic of scanning electron microscopy

The fractured surface morphology is viewed using Leica – 440 Scanning Electron Microscope operated at 20kV, for the dispersion of multiwalled carbon nanotubes and $BaTiO_3$ nanoparticles in the polymer matrix.

2.3.4 Differential Scanning Calorimeter (DSC):

Perkin Elmer DSC is a power compensating type calorimeter, which gives the differential power required to maintain both the sample and the reference at the same temperature during heating and cooling.

During heating as the solid sample melts and transform to liquid state, it absorbs more energy (endothermic) than that of reference. Similarly, as the crystallization takes place excess energy is given out (exothermic) which is monitored. As a result, the melting and crystallization processes appear as peaks (endothermic or exothermic) and the area under the curve gives a direct measure of the heat of fusion or crystallization.

Non-isothermal, isothermal crystallization and crystal-to-crystal phase transformation of PB and the nanocomposites were studied by using a Perkin Elmer DSC-2 equipped with Thermal Analysis Data Station (TADS), in nitrogen atmosphere. The energy and temperature scales are calibrated using Indium, Tin and Lead as standards.

The phase transformation of PB and the nanocomposites is studied using a Perkin Elmer DSC–2. The samples about 5-6mg are prepared by melting the polymer and nanocomposites in the DSC cell at a rate of 10 °C/min up to 150 °C and held for 2 minutes at same temperature and cooled to room temperature at 40 °C/min. This step is carried out to ensure identical thermal history for each sample. The samples are then stored at room temperature. The phase transformation of Form II to Form I is monitored by measuring the enthalpies of two melting peaks corresponding to the particular crystal forms at various time intervals. The crystalline fraction for each form is calculated by using the values of heat of fusion for pristine PB and the nanocomposites after aging for 216 hrs. (As the heat of fusion remains almost same after 216 hrs)

2.3.5 Optical Microscopy (OM):

A microscope is a simple lens system for magnifying small objects. The first lens called objective has a short focal length of few millimeter, and creates an image of the object in the intermediate image plane. This image is then viewed by another lens (eye - piece) that provide additional magnification. A polarized light beam is used to view the spherulitic morphology. A spherulite is a commonly observed spherically symmetrical morphological feature consisting of chain folded lamellae radiating from a central point. A spherulite becomes three-dimensional spherical object by virtue of the fact that the lamellae occasionally branched. The dimensions of spherulites ranges from several microns to some millimeters, sometimes it reaches up to a centimeter in few cases. Macromolecular chains in a spherulite are arranged perpendicular to the radius. Spherulites exhibit birefringence and possess anisotropic properties due to the radial symmetry. The birefringence is observed because the orientation of the crystallographic axes continuously changes along the angular coordinate therefore the spherulites can be readily analyzed by polarized light microscopy.

The spherulitic morphology of PB and nanocomposites is studied with a Leica Laborlux 12 Pol S polarized light microscope. The samples are prepared by melt pressing at 160 °C between a glass slide and a cover slip and kept for a minute to ensure uniform melting. The slide then transferred to the hot stage maintained at desired temperature. The photomicrographs under cross polarizers are taken using Cannon Powershot S 50 digital camera.

2.3.6 Dynamic Mechanical Analysis (DMA):

In dynamic mechanical analysis, a sinusoidal strain or stress is applied to a sample and the response is monitored as a function of frequency and temperature.

For an applied stress varying sinusoidally with time, a viscoelastic material will also respond with a sinusoidal strain for low amplitudes of stress. The sinusoidal variation in time is usually described as a rate specified by the frequency (f = Hz; ω = rad/sec).

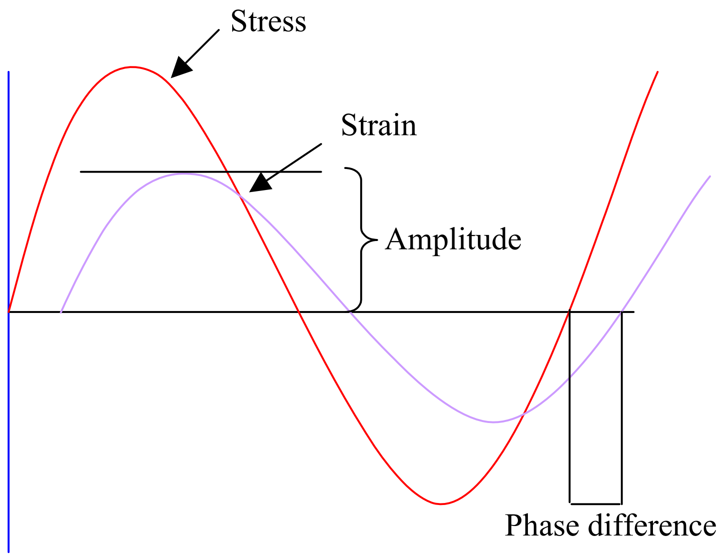

Figure 2.5: Principle of dynamic mechanical analysis

The strain of a viscoelastic body is out of phase with the stress applied, by the phase angle, δ. This phase lag is due to the excess time necessary for molecular motions and relaxations to occur. Principle of DMA is shown in figure 2.5. The viscoelastic material is subjected to a sinusoidally varying stain,

$$\varepsilon = \varepsilon_o \sin(\omega t) \qquad (1)$$

Where ε_o is the amplitude and ω is the angular frequency. Due to viscoelasticity, the stress resulting from the strain will not be in phase. The shift between stress and strain is denoted by δ. The resulting stress will then be

$$\sigma = \sigma_o \sin(\omega t + \delta) \tag{2}$$

The assumption made that the stress varies sinusoidally is valid as long as the material is linearly viscoelastic. By using classic trigonometry the eq. 2 can be rewritten as

$$\sigma = \sigma_o \sin(\omega t) + \sigma_o \cos(\omega t) \sin(\delta) \tag{3}$$

Thus the stress is expressed in two terms, the first on describes the in phase stress and the second one describes an out of phase stress. In another words, the stress is divided into elastic and viscous terms. Therefore, the elastic modulus and viscous modulus can be defined as follows

$$E' = \sigma_o / \varepsilon_o \cos(\delta) \text{ ....Elastic modulus} \tag{4}$$

$$E'' = \sigma_o / \varepsilon_o \sin(\delta) \text{ ....Viscous modulus} \tag{5}$$

The elastic modulus is commonly referred to as the storage modulus while the viscous modulus is referred to as the loss modulus (since the non-elastic effects lead to mechanical losses). To be able to define a total dynamic modulus it is appropriate to view stress and stain in a complex way:

$$\varepsilon = \varepsilon_\circ e^{(i\omega t)} \tag{6}$$

$$\sigma = \sigma_0 e^{i(\omega t + \delta)} \tag{7}$$

The ratio between stress and strain is called the complex modulus, E*

$$E^* = \frac{\sigma}{\varepsilon} = \frac{\sigma_\circ}{\varepsilon_\circ} e^{i\delta} = \frac{\sigma_\circ}{\varepsilon_\circ}(\cos\delta + i\sin\delta) = E' + iE'' \tag{8}$$

Equation (8) shows that the complex modulus obtained from a dynamic mechanical test consists of "real" and "imaginary" parts. The real (storage) part describes the ability of the material to store potential energy and release it upon deformation. The imaginary (loss) portion is associated with energy dissipation in the form of heat upon deformation. The above equation is rewritten for modulus as,

$E^* = E' + iE''$ where, E' is the storage modulus and E'' is the loss modulus. The phase angle δ is given by

$$\tan\delta = \frac{E''}{E'} \qquad (9)$$

These properties are expressed in terms of a storage modulus (E'), a loss modulus (E''), and a mechanical damping term (tan δ) (Figure 2.6). Typical values of dynamic moduli for polymers range from 10^5-10^{11} Pa depending upon the type of polymer, temperature, and frequency. The storage modulus (E') is often times associated with "stiffness" of a material and is proportional to the energy stored during a loading cycle. It is related to the Young's modulus, E. The dynamic loss modulus (E'') is often associated with "internal friction" and is sensitive to different kinds of molecular motions, relaxation processes, transitions, morphology, and other structural heterogeneities. It is proportional to the energy dissipated during one loading cycle.

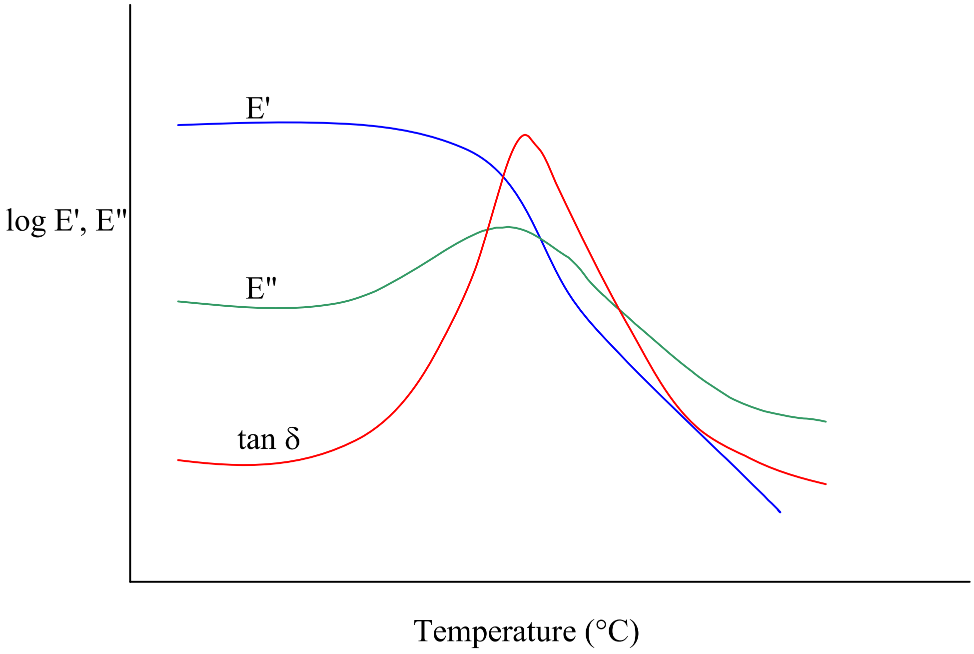

Figure 2.6: Typical DMA scan showing E', E" and tan δ curves

Thus, the dynamic properties provide information at the molecular level to understanding the polymer mechanical behavior. The dynamic mechanical properties of the samples are studied using Rheometric dynamic mechanical analyzer; model DMTA IIIE in the tensile mode. For the constant frequency, oscillatory test, temperature sweep is carried out from -60 to 100 °C and the sample is heated at a rate of 5 °C/min. The frequency is kept as 10 rad/s and the 0.02% strain is fixed suitably in the linear region, by carrying out strain sweep tests and noting that the force lies between the transducer limits.

2.3.7 Melt Rheology:

An oscillatory shear experiment is the most commonly used method for determining the linear viscoelastic properties of polymer melts. In a typical oscillatory shear experiment, a sinusoidally varying small amplitude stress or strain is applied to the sample, and the response, i.e., either sinusoidally varying strain or stress respectively, is measured. A typical frequency response curve is shown in the Figure 2.7. At low frequencies (terminal region), G" > G' i.e., the behavior of polymer melt is liquid like. The slopes of G' and G" are 1 and 2 respectively. G' and G" increases with frequency until the crossover frequency is reached.

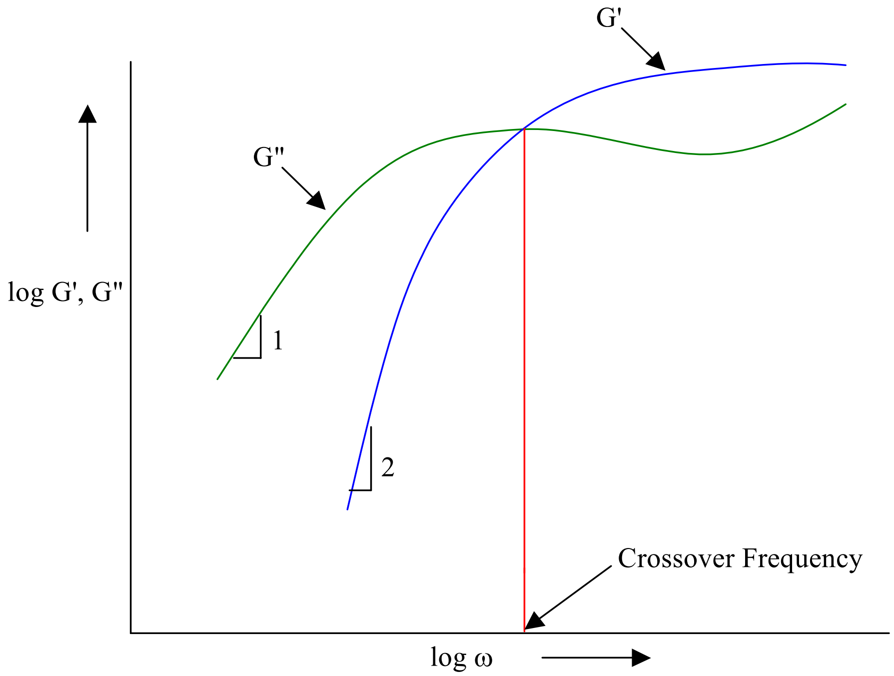

Figure 2.7: G' and G" behavior as the function of frequency

Reciprocal of crossover frequency gives the characteristic relaxation time of the material. After crossover, G' reaches a constant value in the intermediate frequencies called as the plateau modulus. Plateau modulus is independent of the molecular weight and depends only on the chemical nature of the polymer. In this region G" passes through a minimum. At higher frequencies or small time scales, response will be only due to the small parts of the polymer chains. The viscoelastic material functions are strongly dependent on temperature and frequency. No single experiment can cover the entire span of frequencies.

Dynamic oscillatory frequency sweeps are carried out using Rheometric Scientific ARES rheometer in the frequency range of 0.1 to 100 rad/sec at temperatures 175 - 225 °C. Parallel plate geometry of 25 mm diameter is used for this purpose. The specimen thickness is about 0.5 mm. The strain sweep experiment is carried out to find the region of linear response. The strain value fixed at 2% ensuring that the measurements are carried out in linear region.

2.3.8 Dielectric Spectroscopy (DES):

Dielectric spectroscopy is a technique wherein a sinusoidal voltage is applied and the response of the sample is measured. Application of an electric field displaces a charge on the dielectric material and it stores some part of it. The displacement of the charge by applying the electric field is called “polarization.”

There are different types of polarization mechanisms: electronic polarization, atomic polarization, orientation polarization and interfacial polarization.

The dielectric properties of a material are defined by a complex dielectric permittivity, ε^*.

$$\varepsilon^* = \varepsilon' + i\varepsilon'' \qquad (10)$$

Where, ε' is the relative dielectric permittivity (dielectric constant, energy store capacity) of the material and ε'' is the imaginary part which is a measure of the heat related loss of the material known as the dielectric loss (energy dissipitated per cycle). Generally tan δ is discussed ($\tan \delta = \varepsilon''/ \varepsilon'$) which is the phase angle between applied voltage and resulting current. The dielectric constant (ε') is used to define the ability of an insulator to store electrical charge. The schematic for dielectric analyzer is shown in Figure 2.8.

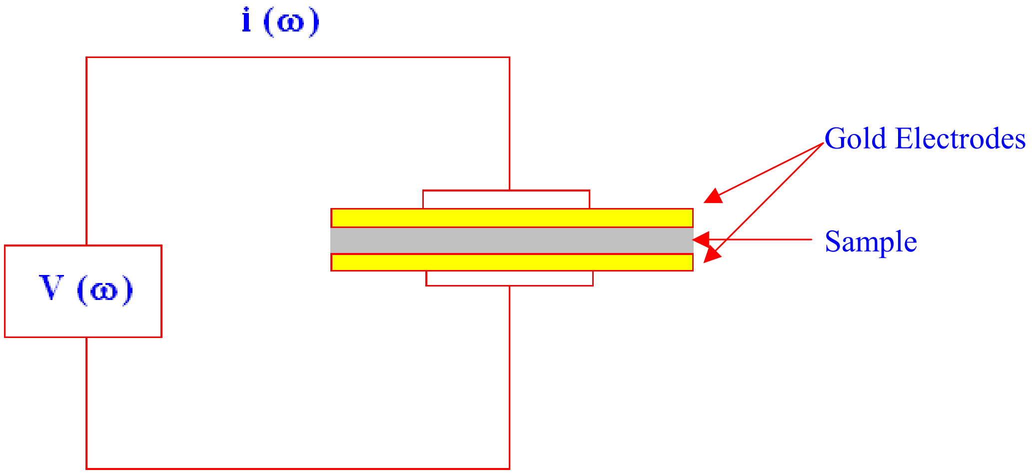

Figure 2.8: Schematic of principle of dielectric analysis

Dielectric properties of the samples in the film phase are measured using the Novo Control Alpha A Analyzer equipped with ZGS active sample cell having temperature controller and WinDeta, WinImp and WinFit softwares. The samples are scanned between frequencies 0.01Hz and 1MHz at temperature ranging from 30 to 100 °C. Bias voltage applied across the sample is 0.1V. The electrode of 20mm diameter is used while thickness of the sample is measured and used while calculating the dielectric constant.

2.3.9 Thermogravimetric Analysis (TGA):

In this technique, change in weight of the sample is monitored when heated under controlled temperature programme. The programme is often consists of linear increase in temperature. This technique is quantitative and is very important to study the reactions taking place while heating the sample.

The important components in the instrumentations are as follows:

A thermobalance: A recording balance having sensitivity around one microgram and capacity of about few hundred milligrams. Furnace: The heating furnace is operated in the temperature range of 50 to 1000 °C with heating rate up to 100 °C/min.

Perkin Elmer TGA7 is used for the study of thermal stability of the pristine polymer and the various nanocomposites in an inert atmosphere.

2.4 Crystallization in Polymers:

Crystallization of long chain flexible molecules of sufficient structural regularity is widely observed for a large number of polymers. The crystallization process consists of two steps such as nucleation and growth. When the nucleation occurs spontaneously only due to the supercooling and no second phase or other nuclei exists, such type of nucleation called as homogeneous nucleation. While in presence of any other second phase such as foreign particle or surface from the same polymer nuclei/crystal, then the nucleation is referred as heterogeneous nucleation.

The nucleation, growth, and kinetics of development of these crystalline regions are of both profound fundamental and pragmatic interest. These characteristics are directly linked to understanding of the morphological details of crystalline regions.

The kinetics of polymer crystallization is controlled by various factors such as molecular weight, chain flexibility, chain defects, and stereo-regularity, etc., which is different from that of small molecules. The crystallization process is also affected by experimental conditions such as temperature, pressure, nucleating agents, and stress, etc.

2.5 Analysis of Experimental data:

2.5.1 Non-isothermal crystallization:

Non-isothermal crystallization is studied for different cooling rates, first the sample is heated by 10 °C/min up to 150 °C and held for two minutes to ensure complete melting and the crystallization peaks are recorded for different cooling rates, such as 2.5, 5, 10 and 20 °C/min. The thermal parameters such as melting peak temperature (T_m), heat of fusion (ΔH_f), crystallization peak temperature (T_c), and heat of crystallization (ΔH_c) are measured as shown in Figure 2.9. The non-isothermal crystallization peaks are analyzed for the total crystallization time. For this purpose the temperature scale was converted to time scale as follows:

$$t_c = (T_i - T_f)/\phi \tag{11}$$

Where T_i is the initial crystallization temperature and T_f is the final crystallization temperature and ϕ is the cooling rate.

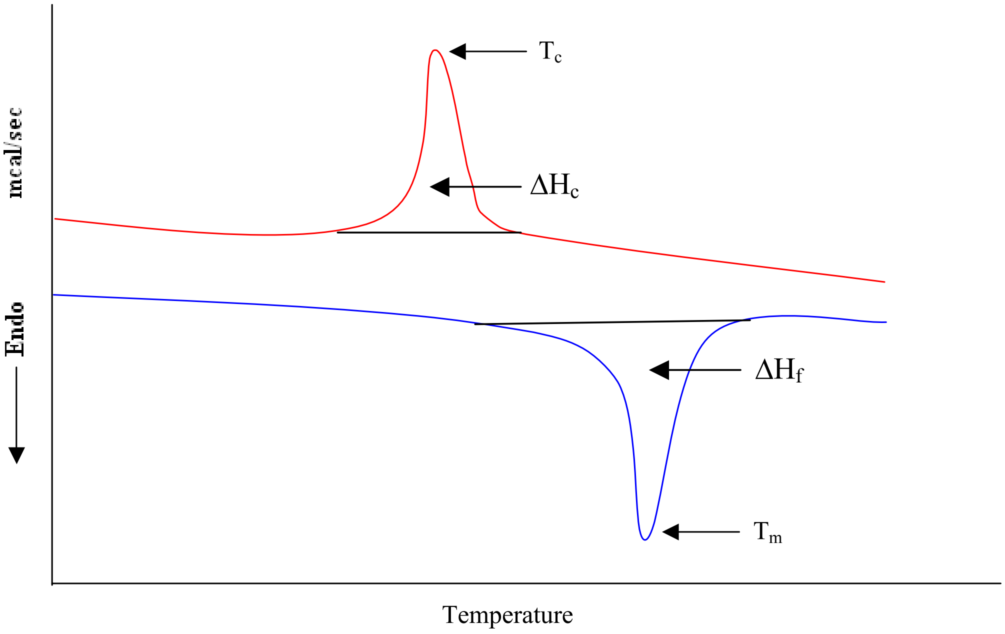

Figure 2.9: Typical non-isothermal crystallization curves, heating (lower curve) and cooling (upper curve)

2.5.1.1 Non- isothermal crystallization kinetics:

The non-isothermal crystallization kinetics is studied using modified Avrami theory by converting temperature scale into the time scale for various degrees of cooling rates. For isothermal crystallization kinetics, Avrami equation [3] was used as given below.

$$1 - X_t = \exp(-Z_t t^n) \qquad (12)$$

While the Avrami equation was reasonable to some extent for many systems, a number of researchers tried to fit experimental results obtained from crystalline polymers and proposed some modified forms.

Considering the non-isothermal character of the process investigated, Jeziorny pointed out that value of rate constant Z_t should be adequately corrected for the cooling rate.

Assuming constant or approximately constant cooling rate, ϕ, the new form of the rate constant is given by

$$\log Z_c = \frac{\log Z_t}{\phi} \qquad (13)$$

During the non-isothermal crystallization process the relation between crystallization time ‘t’ and temperature ‘T’ is given by

$$t = \frac{|T_o - T|}{\phi} \qquad (11)$$

Where T_o is the temperature at which crystallization begins and T is the temperature chosen at particular degree of crystallinity.

The plot of $\log[-\ln(1-X_t)]$ vs. log t gives straight lines, the Avrami exponent (n) and growth rate parameter (Z_t) are calculated from the slope and intercept respectively.

The crystallization half time ($t_{1/2}$) is calculated using following equation:

$$t_{1/2} = \left(\frac{\ln 2}{Z_c}\right)^{1/n} \qquad (14)$$

Liu introduced [4] the combined Avrami-Ozawa equation for determination of non-isothermal crystallization kinetics given as follows.

$$\log Z_t + n\log t = \log K(T) - m\log\phi \qquad (15)$$

The above equation converted to

$$\log\phi = \log F(T) - a\log t \qquad (16)$$

Where, $F(T) = [K(T)/Z_t]^{1/m}$ and ‘a’ is the ratio between the Avrami and Ozawa exponent i.e. n/m. F(T) refers to the value of the cooling rate chosen at unit crystallization time, when the system has defined degree of crystallinity.

The plots of log ϕ vs log t yield a straight line at defined crystallinity with log F(T) and '–a' are determined by intercept and slope respectively.

2.5.1.2 Energy of activation:

The energy of activation for non-isothermal crystallization is derived from the Kissinger equation [5] as follows.

$$d[\ln(\frac{\phi}{T_c^{\ 2}})]/[d(\frac{1}{T_c})] = -E_a / R \tag{17}$$

Where, ϕ is cooling rate, T_c is crystallization peak temperature, E_a is energy of activation for crystallization, and R is universal gas constant. The graph of $(\ln\phi/T_c^2)$ vs $(1/T_c)$ is plotted and straight lines are fitted, and from the slopes, activation energy is derived.

2.5.1.3 Nucleating Activity:

The nucleating activity of the nanofillers is determined by the method used by Dobreva and Gutzow [6], where the cooling rate and the degree of super cooling is taken into consideration. For homogeneous nucleation the following equation is used:

$$\log\phi = A - \frac{B}{2.303\Delta T_c^{\ 2}} \tag{18}$$

For the heterogeneous system in which the foreign particles help in crystallization, the following equation is used:

$$\log\phi = A - \frac{B^*}{2.303\,\Delta T_c^{\ 2}} \tag{19}$$

Where ϕ is cooling rate, ΔT_c is the degree of supercooling (T_m-T_c), A, B and B* are constants and B is parameter that can be calculated using the following equation:

$$B = \frac{\omega\sigma^3 V_m^{\ 2}}{nkT_m \Delta S_m^{\ 2}} \qquad (20)$$

Where ω is a geometrical factor; σ is the specific surface energy, V_m is the molar volume of the crystallizing substance, n is the Avrami exponent, ΔS_m is the entropy of melting and k is the Boltzmann constant.

The nucleating activity, Φ is determined from the ratio of B* to B, the slopes of linear function log ϕ as the function of $1/\Delta T_c^2$.

2.5.2 Isothermal Crystallization:

In an isothermal crystallization, the sample is heated at 40 °C/min up to 150 °C and held for two minutes, then quenched at a cooling rate of 160 °C/min to the desired crystallization temperature (72-96 °C). A typical isothermal crystallization exotherm is shown in figure 2.10.

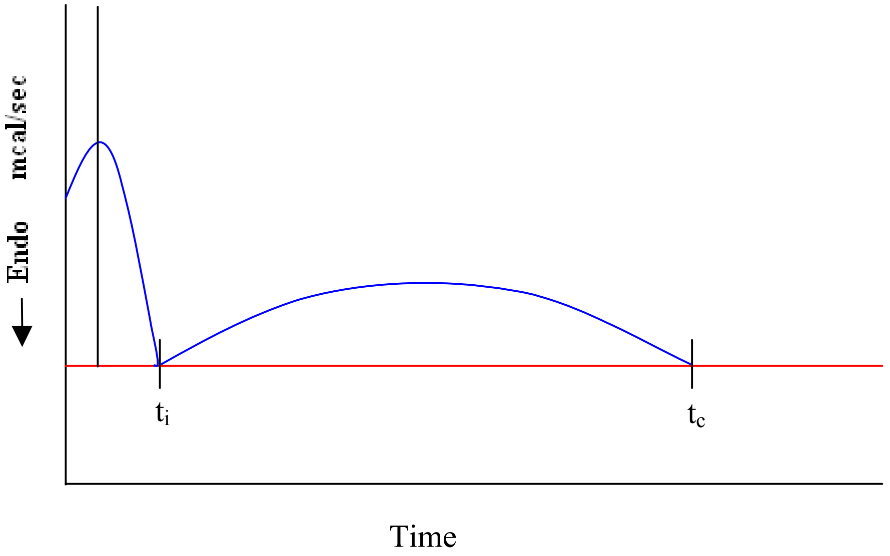

Figure 2.10: A typical isothermal crystallization exotherm

The curve shows induction time (t_i), total crystallization time (t_c). The induction time is the time required to initiate the isothermal crystallization while the total crystallization time is total time required to complete the crystallization process.

The crystallization peaks were recorded on a time base and analyzed by Avrami equation [3] for determining the rate constant.

2.5.2.1 Isothermal Crystallization Kinetics:

The Avrami equation is used to analyze the isothermal curves for the crystallization kinetics in PB and PB nanocomposites.

$$X_t = 1 - \exp(-Kt^n) \qquad (21)$$

Where, X_t is the relative degree of crystallinity at different crystallization time, n is the Avrami exponent that gives dimensionality of the crystal and K is the rate constant related to nucleation and growth parameters. The equation (21) is written as follows:

$$\log[-\ln(1 - X_t)] = n \log t + \log K \qquad (22)$$

By plotting $\log[-\ln(1 - X_t)]$ vs. log t, a straight line is obtained if the crystallization kinetics obeys the Avrami theory. The Avrami exponent (n) and the crystallization kinetic constant (K) are obtained from the slope and the intercept of the straight lines respectively. The total crystallization time (t_c), and the rate constant are calculated from the plots.

Depending on the mechanism of nucleation (homogeneous or heterogeneous) and type of crystal growth, different values of '*n*' are obtained. Avrami exponent '*n*' is a combined function of number of dimensions in which growth unit takes place and the order of time dependence of the nucleation process. The value of *n* =1 corresponds to one-dimensional growth (rods). *n* =2 and 3 corresponds to two-dimensional disc and three-dimensional spheres respectively for instantaneous nuclei. When the growth is sporadic, *n* = 2, 3 and 4 represents one dimensional, two-dimensional and three-dimensional growth respectively. However, integer values of Avrami exponent are seldom obtained due to various simplifications used in the original derivation. Hence, the precise interpretation of the results is difficult [3].

Isothermal crystallization kinetics is further analyzed using the spherulitic growth rate in the context of the Lauritzen – Hoffman secondary nucleation theory [7]. The growth rate G is given as a function of the crystallization temperature T_c, using following bi-exponential equation:

$$G = G_0 \exp\left[\frac{-U^*}{R(T_c - T_\infty)}\right] \exp\left[\frac{-K_g}{fT_c \Delta T}\right] \qquad (23)$$

Where G_0 is the pre-exponential factor, the first exponential term contains the contribution of diffusion process to the growth rate, while the second exponential term is the contribution of nucleation process. U* and T_∞ are the Vogel-Fulcher-Tamman-Hesse (VFTH) parameters that describe the transport of molecular segments across the liquid/crystal interphase to the crystallization surface, K_g is the nucleation constant, ΔT denotes the degree of supercooling (T_m-T_c) and f is the correction factor.

When $\ln(1/t_{1/2})+U^*/R(T_c-T_\infty)$ is plotted against $1/fT_c\Delta T$ gives a straight line having a slope equal to K_g. For the growth rate G, the approximation: $G = 1/t_{1/2}$ is used. For a secondary or heterogeneous nucleation, K_g can be calculated from

$$K_g = \frac{nb\sigma\sigma_e T_m^{\ 0}}{\Delta H_f\ k\beta} \qquad (24)$$

Where σ, σ_e are the side surface and fold surface free energies which measures the work required to create a new surface, b is the distance between two adjacent fold planes, β is the parameter that depends on the crystallization regime and *k* is the Boltzmann constant. In all calculations, the values for U* is taken as 1500 cal/mol and T_∞ as T_g - 30°C. The correction factor f is calculated as, $f = 2\,T_c/(T_m^\circ + T_c)$, and T_m° is taken as 147°C.

2.5.2.2 Energy of activation:

The energy of activation for the isothermal crystallization is determined using the following rate equation.

$$\frac{1}{n}(\ln K) = \ln K_0 - \frac{\Delta E_a}{RT} \qquad (25)$$

The Arrhenius plot of [1/n ln K vs $1/T_c$] gives the straight lines from which the slope is determined as Ea/R and then energy of activation is calculated. Where, n is an Avrami constant, K is a rate constant; R is a universal gas constant.

References:

[1] Bish D, Post J. Modern Powder Diffraction: Reviews in Mineralogy, 20 Edition, Mineralogical Society of America: Washington DC **(1989)**

[2] Klugg H, Alexander L. X – ray diffraction procedures; John Wiley and Sons: USA **(1974)**

[3] a)Avrami M. Journal of Chemical Physics, 7,1103 **(1939)**
b)Avrami M. Journal of Chemical Physics, 8, 212 **(1940)**
c)Avrami M. Journal of Chemical Physics, 9, 177 **(1941)**

[4] Liu T, Mo Z, Wang S, Zang H. Polymer Engineering and Science 37, 568 **(1997)**

[5] Kissinger HE. Journal of Research of the National Bureau of Standards 57 (4), 217 **(1956)**

[6] Dobreva A, Gutzow I. J Non-Cryst Solids, 162, 13 **(1993)**

[7] Hoffman J, Davis G, Lauritzen J. In: Hannay NB, Treatise on solid-state chemistry, Vol. 3. New York: Plenum Press; p. 497–614 **(1976)**

Chapter 3

PB/Clay Nanocomposites

The work presented in this chapter has been published in the following Journals

1] Wanjale SD, Jog JP. Journal of Polymer Science: Part B: Polymer Physics 41, 1014-1021 (2003)

2] Wanjale SD, Jog JP. Journal of Macromolecular Science: Part B: Physics B42, 1141–1152 (2003)

3.1 Introduction:

This chapter presents a study of nanocomposites of PB with organically modified clay. The nanocomposites are prepared by melt intercalation technique. Melt processing is carried out at 150 °C. Three compositions with 3, 5 and 7 wt% of clay are prepared and coded as PB3N, PB5N and PB7N. These nanocomposites are characterized by various techniques such as, XRD, DSC, OM, DMA, and TGA. Effect of clay on the crystallization, phase transformation, thermal stability, and viscoelastic properties are studied.

Poly(1-butene) (PB) and organically modified clay (Nanocor) are used for the preparation of nanocomposites, the details of the materials and their characterization are given in the following sections.

3.2 Material Characterization:

3.2.1 Poly(1-butene) (PB):

Poly(1-butene) (PB) used as a matrix polymer is supplied by Aldrich. The average molecular weight of PB is 570,000 g/mol.

3.2.1.1 X - ray diffraction (XRD):

The X - ray diffraction patterns for two crystalline forms, Form I and Form II of poly(1-butene) are depicted in Figure 3.1. These two crystalline forms are easily distinguishable from each other as they show characteristic diffraction peaks at distinct 2 θ angles. Form I is characterized by the diffraction peaks at 2θ values of 10.2°, 17.4° and 21.6°, while Form II shows the diffraction peaks at 2θ values of 12°, 17°, and 18.5° [1].

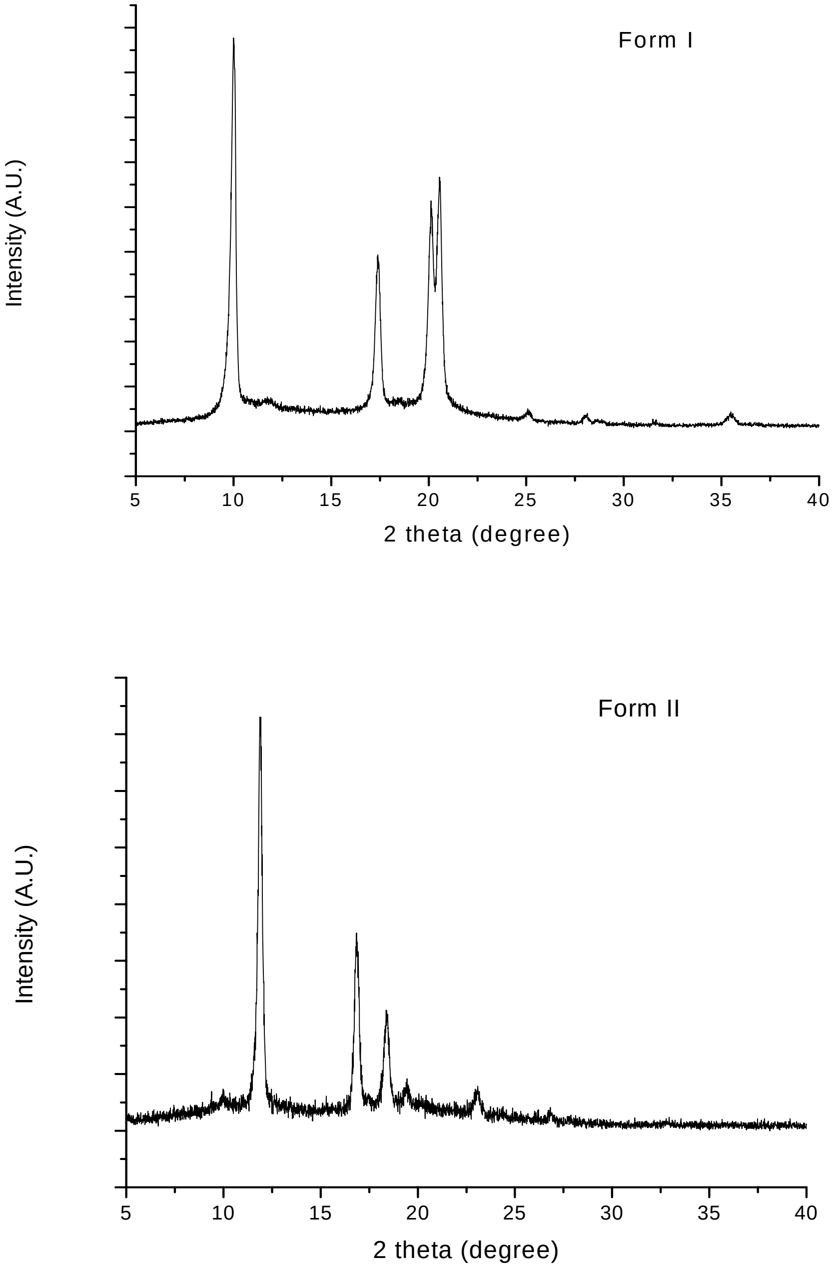

Figure 3.1: X - ray diffraction patterns for Form I and Form II of PB

3.2.1.2 Differential Scanning Calorimetry (DSC):

Figure 3.2 shows the DSC thermograms for the two crystalline forms. Form I shows a melting peak at about 128 °C, while Form II melts at around 114 °C [1]. The heat of fusion (ΔH_f) for Form I is 68.9 J/g and that of Form II is about 31.0 J/g.

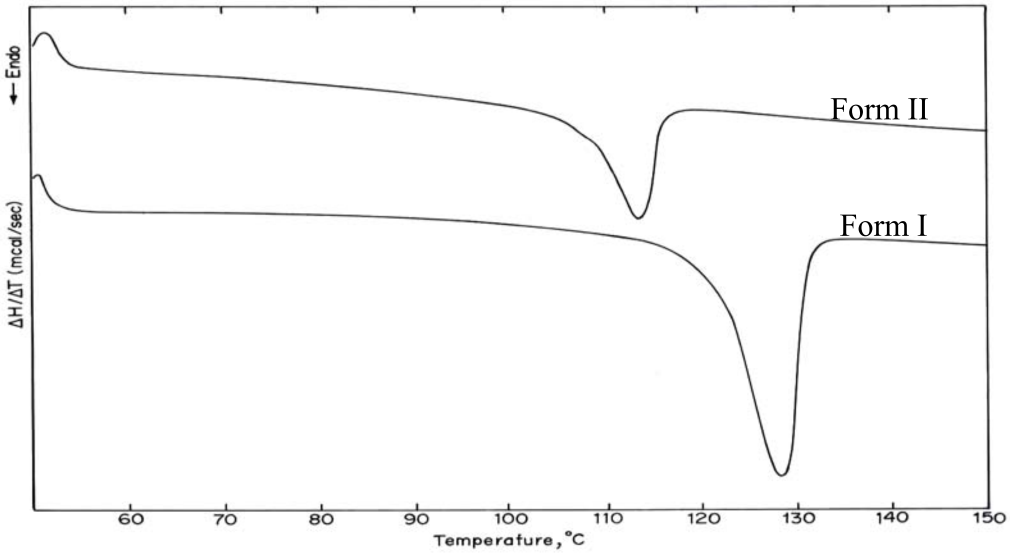

Figure 3.2: DSC thermograms for Form I and Form II of PB

3.2.1.3 Thermogravimetric Analysis (TGA):

The TGA thermogram of PB is shown in Figure 3.3. The degradation of pure PB starts at 350 °C and the complete degradation occurs at 475 °C in the nitrogen atmosphere. It can be seen from the thermogram that the thermal degradation of PB takes place in a single step.

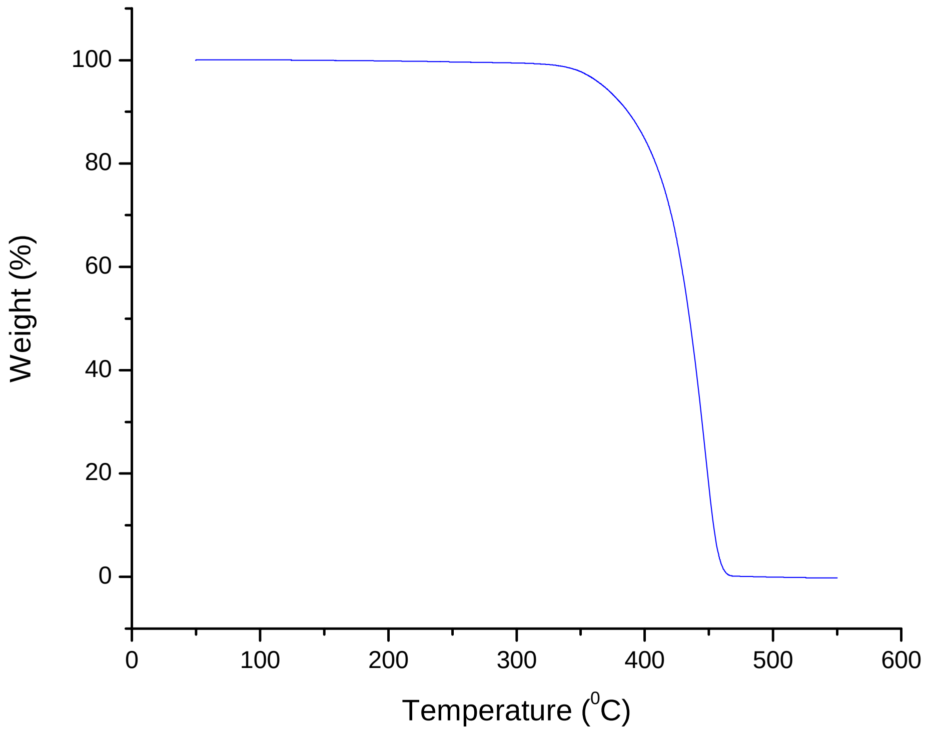

Figure 3.3: TGA thermogram for PB

3.2.2 Clay:

Organically modified clay (Nanocor) from Nanocor Inc, USA, is used for the preparation of PB/clay nanocomposites. As per company data sheet, the cation exchange capacity (CEC) of the clay is 135 meq/100g and it is modified using octadecyl amine. The organic content is reported to be about 36%.

3.2.2.1 X - ray diffraction (XRD):

The X - ray diffraction pattern of the Nanocor clay is shown in Figure 3.4. Clay exhibited two prominent diffraction peaks at 2θ of 3.6° and 8.08° corresponding to d spacing of 2.4

and 1.09 nm respectively. The d_{001} peak at 2.4 nm is used for further structural evaluation of the nanocomposites.

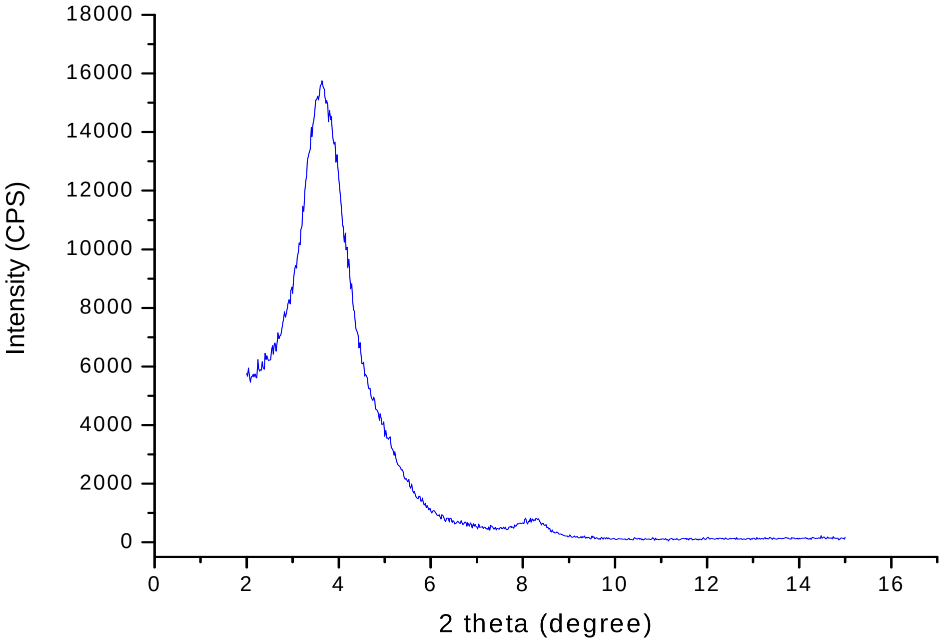

Figure 3.4: X - ray diffraction pattern for Nanocor clay

3.2.2.2 Scanning electron microscopy (SEM):

The morphology of the clay is studied using SEM. The micrographs of the clay particles are shown in Figure 3.5. The clay particles are found to form agglomerates of size about 6-10 µm [figure 3.5(A)]. The platy structure of the clay is clearly visible in the micrograph taken at a higher magnification [(figure 3.5(B)].

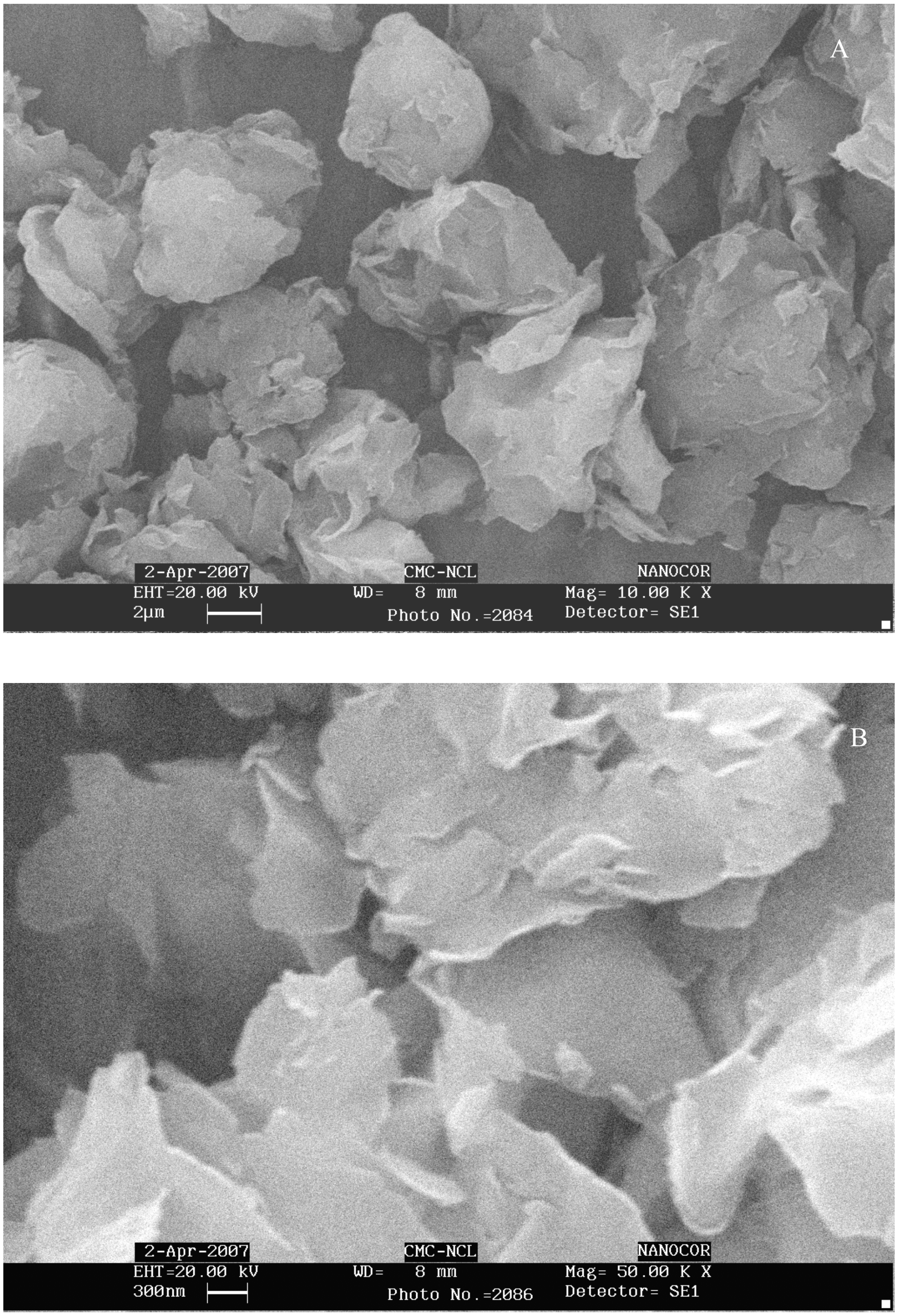

Figure 3.5: Scanning electron micrographs for Nanocor clay, A (×10K) and B (×50K)

3.2.2.3 Thermogravimetric analysis (TGA):

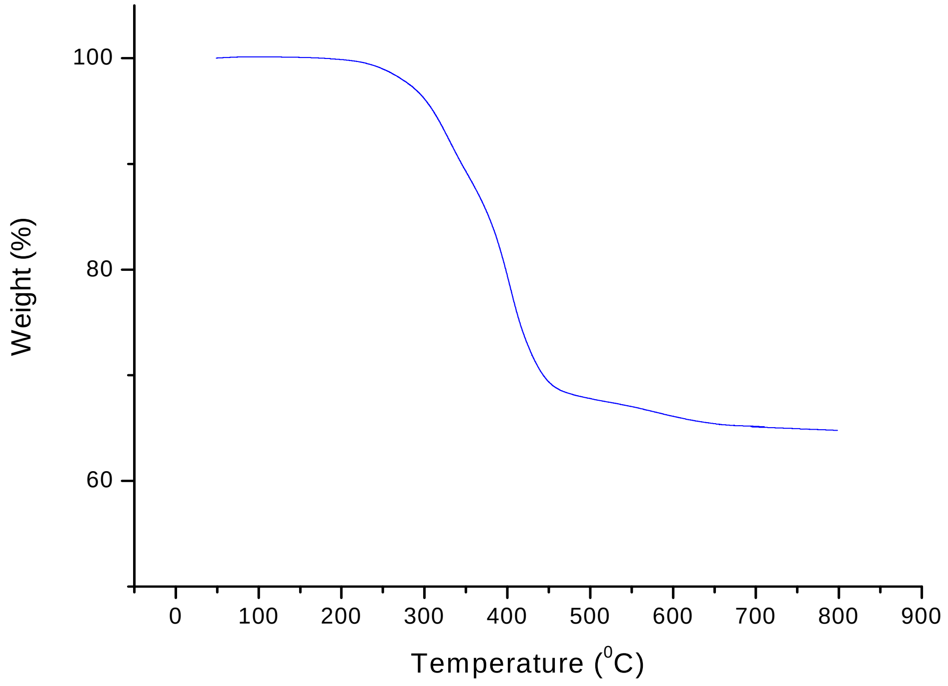

Figure 3.6: TGA thermogram for clay

The TGA thermogram for the clay is shown in figure 3.6. The thermogram shows that degradation starts at 250 °C. Above 650 °C the weight remains constant at 64%, suggesting the percent weight loss is 36%. The percent weight loss is due to the organic moiety present in the organically modified clay.

3.3 Results and Discussion:

3.3.1 Structure Evaluation:

3.3.1.1 X-ray diffraction analysis (XRD):

X - ray diffraction patterns can be used to confirm the intercalation of polymer matrix into the clay layers. Increase in d spacing generally suggests an intercalated structure while the complete disappearance of the peak suggests delamination or exfoliated structure. The XRD patterns for clay and the nanocomposites are shown in Figure 3.7.

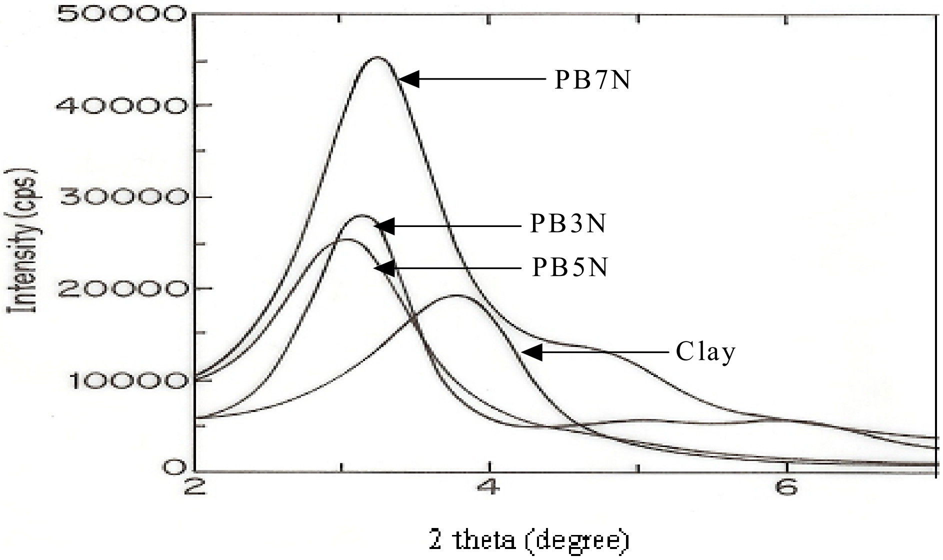

Figure 3.7: X - ray diffraction patterns for clay and PB/clay nanocomposites

The XRD pattern of Nanocor clay shows characteristic d_{001} peak at 2θ value of 3.6° corresponding to basal spacing of 2.4 nm. The nanocomposites exhibit well-defined diffraction peaks with the increase in d spacing of about 0.4 nm, 0.54 nm and 0.32 nm for PB3N, PB5N, and PB7N respectively. The increase in the d spacing for all the three compositions confirms the intercalation of polymer in clay layers and thus the formation of intercalated structures in PB/clay nanocomposites.

3.3.1.2 Transmission electron microscopy (TEM):

The dispersion of the clay layers in PB matrix is studied using TEM. Figure 3.8 shows the TEM micrographs for the PB5N nanocomposites at two different magnifications. The nanoscale dispersion of the clay tactoids of the size varies from 20 to 100 nm (dark lines) in the polymer matrix is clearly discernible.

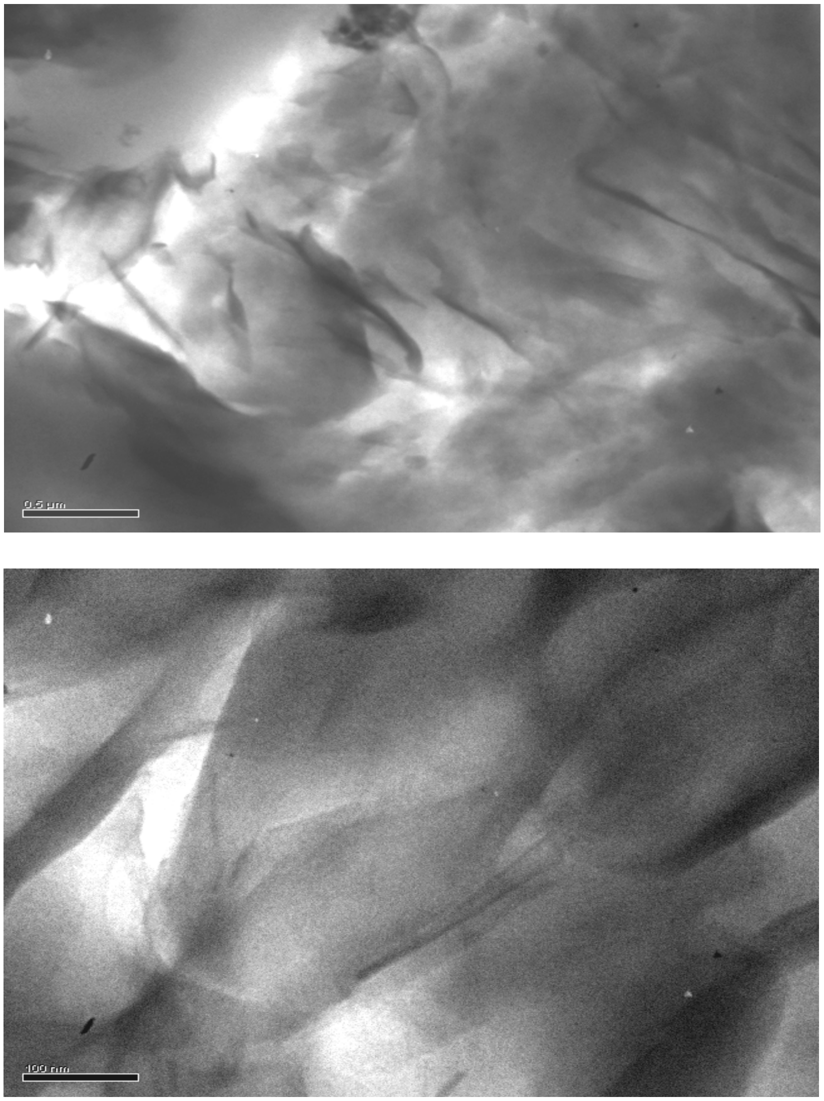

Figure 3.8: TEM micrographs for PB5N

3.3.2 Crystallization studies:

As described earlier in the introduction section, the layered silicates bring about significant changes in the crystallization behavior of the polymer matrix. In the following section, we will discuss the crystallization behavior of PB and the nanocomposites.

3.3.2.1 Non-isothermal crystallization:

A study of non-isothermal crystallization of polymer nanocomposites is of pragmatic significance because in processing, crystallization occurs under non-isothermal conditions. It has been reported that the nanoscale clay layers bring about significant changes in the crystallization behavior and polymorphic nature in semicrystalline polymers. In Nylon 6 (PA) the γ form is predominantly observed in presence of clay [2], while Priya et al [3] reported the presence of β form in polyvinylidine fluoride (PVDF) for intercalated nanocomposites with organically modified clays.

It was thus interesting to study the effect of clay layers on the crystallization behavior of PB. The melting and crystallization parameters determined from heating and cooling scans for PB and PB/clay nanocomposites are presented in Table 3.1.

Table 3.1: Melting and crystallization parameters for PB and PB/clay nanocomposites

Sample	T_m (°C)	T_c (°C)	ΔH_f (J/g)
PB	128.9	69.8	68.9
PB3N	128.2	71.5	69.0
PB5N	128.7	74.2	71.5
PB7N	128.4	73.8	69.2

The values of heat of fusion (ΔH_f) of nanocomposites are comparable to that of PB. The crystallization temperatures for the nanocomposites are higher than that of PB suggesting nucleating effect of clay.

Non-isothermal crystallization behavior of PB and the nanocomposites with clay is studied to investigate the effect of cooling rate. Different cooling rates such as 2.5, 5, 10 and 20 °C/min are used. The crystallization parameters for PB and nanocomposites for different cooling rates are shown in Table 3.2. It can be seen from the Table 3.2, that the crystallization peak temperature (T_c) for PB as well as for nanocomposites is shifted to lower temperatures as the cooling rate increased. However, it is observed that at a given cooling rate, T_c of nanocomposites is higher than that of pristine PB. This clearly suggests that incorporation of clay results in enhanced nucleation of PB matrix.

3.3.2.1.1 Non- isothermal Crystallization Kinetics:

The non-isothermal crystallization kinetics is studied using modified Avrami theory by converting temperature scale into time scale for various cooling rates. The $t_{1/2}$, n, Z_t and Z_c are given in Table 3.2. As the cooling rate increased, crystallization rate constant (Z_t) also increased in both PB and PB/clay nanocomposites but latter showed higher values compared to those for pristine PB. The $t_{1/2}$ values are found to be lower for nanocomposites than those for PB. Above results signify that the rate of crystallization is enhanced in nanocomposites. In non-isothermal crystallization Z_t (rate constant) and n (Avrami exponent) does not have the same physical significance as in an isothermal crystallization study due to the constant change in temperature in case of non-isothermal crystallization [4].

Table 3.2: Non-isothermal crystallization parameters for PB and PB/clay Nanocomposites (modified Avrami analysis)

Sample	ϕ	$t_{1/2}$ (min)	T_c (°C)	n	Z_t (min^{-1})	Z_c
PB	2.5	1.5	79.4	4.2	4.99×10^{-3}	0.12
	5	1.1	74.3	4.5	5.28×10^{-2}	0.56
	10	1.0	69.8	4.6	0.54	0.94
	20	0.9	62.9	4.2	3.48	1.06
PB3N	2.5	1.4	81.3	4.1	0.0137	0.17
	5	1.0	76.9	4.0	0.1656	0.70
	10	0.9	71.5	3.9	0.979	1.00
	20	0.9	64.5	3.6	5.051	1.08
PB5N	2.5	1.4	82.9	4.2	0.0106	0.16
	5	1.0	78.8	4.5	0.096	0.63
	10	0.9	74.2	4.4	1.656	1.05
	20	0.9	68.5	4.4	10.952	1.13
PB7N	2.5	1.3	83.2	3.7	0.0247	0.23
	5	1.0	78.4	4.3	0.0699	0.59
	10	0.9	73.8	4.2	0.725	0.97
	20	0.9	68.5	4.5	8.89	1.12

Liu et al [5] modified the Avrami-Ozawa equation by considering the relative degree of crystallization (Combined Avrami-Ozawa equation). The non-isothermal crystallization process is then analyzed using the parameters such as relative degree of crystallinity (X_t), cooling rate (ϕ), and crystallization temperature (T_c). Figure 3.9 illustrates plots of log ϕ vs log t at different relative degrees of crystallinities.

The values of F(T) and 'a' are determined from the plots and summarized in Table 3.3. It can be seen from the data that the values of F(T) are increased with the X_t, signifying that the time required for reaching the defined X_t increased for the given cooling rate. In case of nanocomposites the values of F(T) are found to be lower than those for PB suggesting that the time required to attain the certain X_t is lowered as compared to the time required for the same X_t in the pristine polymer. The Avrami-Ozawa exponents are found in the range of 1.2 and 1.4 for both PB and PB/clay nanocomposites signifies that Avrami exponent (n) is always slightly greater than Ozawa exponent (m).

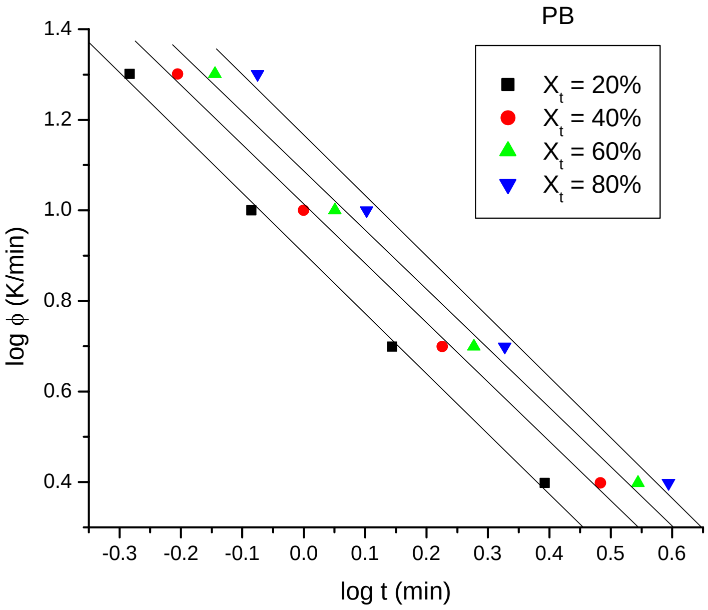

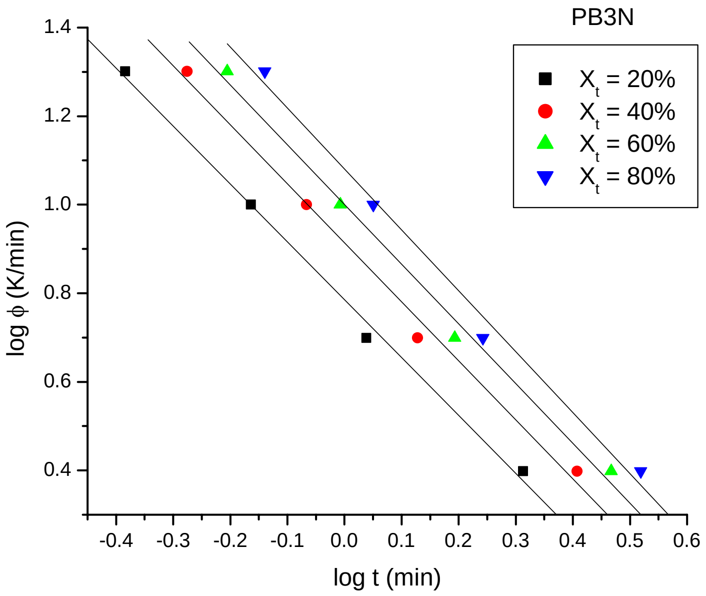
PB3N
■ X_t = 20%
● X_t = 40%
▲ X_t = 60%
▼ X_t = 80%
log ϕ (K/min)
1.4
1.2
1.0
0.8
0.6
0.4
log t (min)
-0.4
-0.3
-0.2
-0.1
0.0
0.1
0.2
0.3
0.4
0.5
0.6

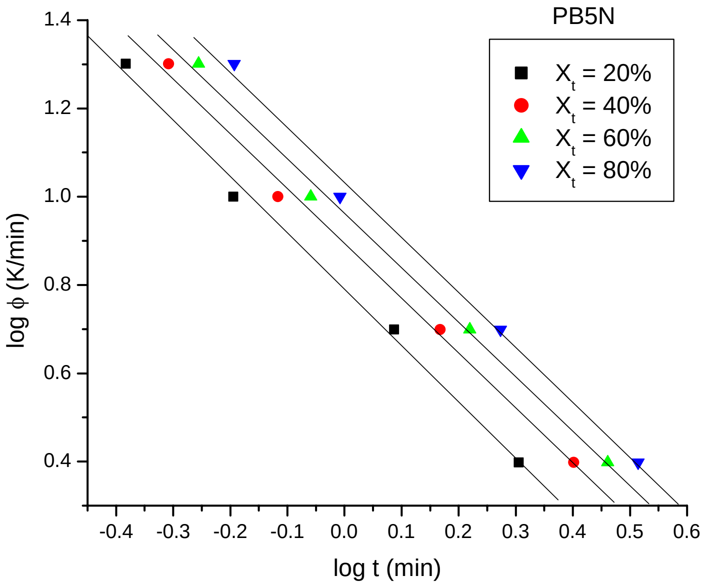
PB5N
■ X_t = 20%
● X_t = 40%
▲ X_t = 60%
▼ X_t = 80%
log ϕ (K/min)
1.4
1.2
1.0
0.8
0.6
0.4
log t (min)
-0.4
-0.3
-0.2
-0.1
0.0
0.1
0.2
0.3
0.4
0.5
0.6

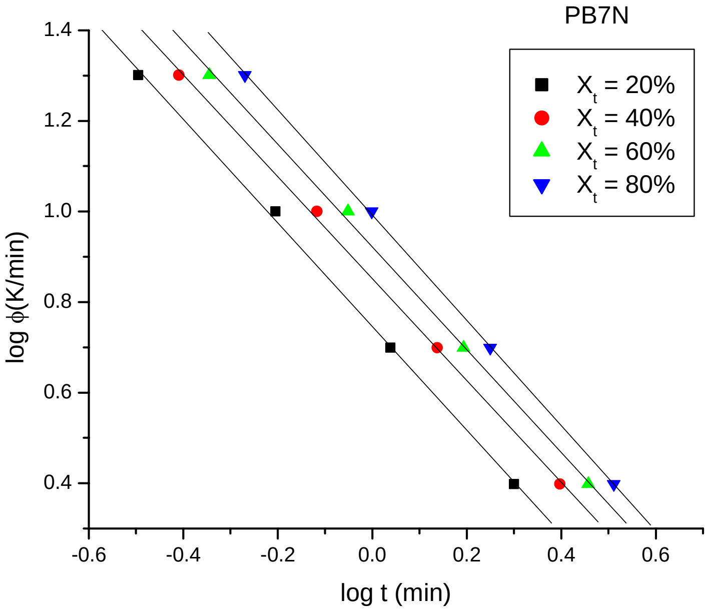

Figure 3.9: log ϕ vs log t for PB and PB/clay nanocomposites

Table 3.3: Non-isothermal crystallization parameters for PB and PB/clay Nanocomposites (Combined Avrami–Ozawa analysis)

Sample	X_t (%)	F(T)	'a'
PB	20	8.0	1.3
	40	10.3	1.3
	60	12.2	1.3
	80	14.7	1.3
PB3N	20	6.1	1.3
	40	8.2	1.3
	60	10.1	1.4
	80	12.0	1.4
PB5N	20	6.2	1.3
	40	7.8	1.2
	60	9.2	1.2
	80	10.8	1.3
PB7N	20	6.6	1.4
	40	8.5	1.4
	60	10.4	1.4
	80	12.4	1.4

3.3.2.1.2 Energy of Activation

The non-isothermal crystallization activation energy is calculated by using the Kissinger equation as explained in part 2.5.1.2. The plot of $\ln(\phi/T_c^2)$ vs $(1/T_c)$ is shown in Figure 3.10 and from the slopes of straight lines, activation energies are calculated. Energy of activation for PB is about 131 kJ/mol, while it is 127, 151 and 149 kJ/mol for PB3N, PB5N and PB7N nanocomposites respectively.

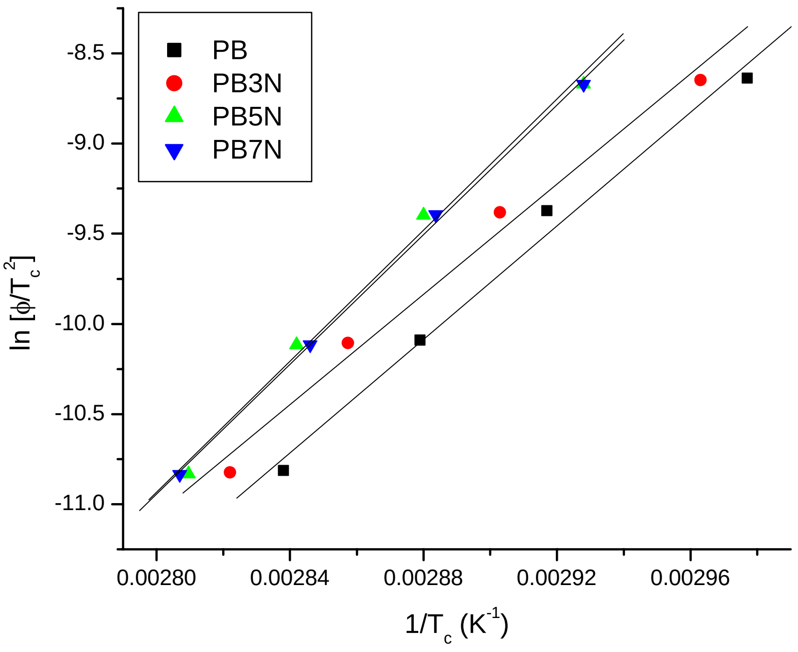

Figure 3.10: ln [ϕ/T_c^2] vs 1/T_c plots for PB and PB/clay nanocomposites

The increase in activation energy for the nanocomposites indicates that the incorporation of clay impedes the chain transportation to the growing crystal surfaces [6]. In general, it is observed that there are two mutually opposite effects of clay on the crystallization behavior such as nucleating ability and growth retardation. Both effects are related to the content and dispersion of clay. Although an increase in activation energy is observed, the other results such as F(T) and Z_t indicate increase in rate of crystallization. These results thus suggest that the incorporation of clay layers have significant effect on nucleation rather than growth and the net influence is positive.

3.3.2.1.3 Nucleating Activity:

The nucleating activity (Φ) of the clay is determined by the method used by Dobreva and Gutzow [7].

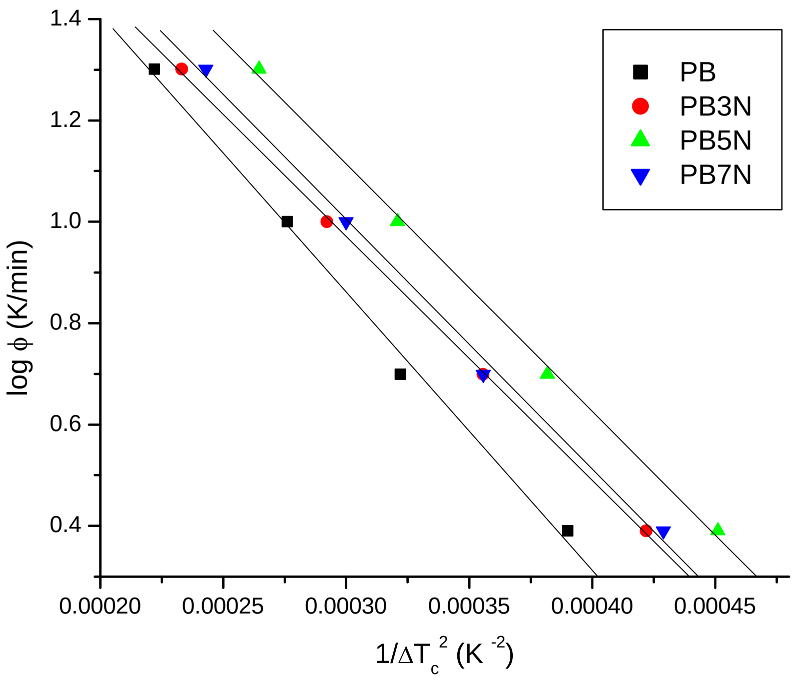

Figure 3.11: log ϕ vs 1/ΔT$_c^2$ for PB and PB/clay nanocomposites

The slopes, B* and B of linear plots of log ϕ vs 1/ΔT$_c^2$ (Figure 3.11) are used to determine Φ. It has been stated that for active surface Φ tends to zero while when it tends to one, the surface is considered as an inert surface for nucleation [8]. The values of nucleating activity calculated are 0.88, 0.89, and 0.90 for PB3N, PB5N, and PB7N nanocomposites respectively. From these results, it can be seen that clay layers do not offer active surface for nucleation.

3.3.2.2 Isothermal Crystallization:

The isothermal crystallization of PB and PB/clay nanocomposites is studied to determine the effect of incorporation of clay on crystallization behavior. The measurements are carried out over a temperature range from 80 °C to 90 °C. Figure 3.12 illustrates the temperature dependence of total crystallization time (t_c) calculated at each crystallization temperature (T_c) for PB and PB/clay nanocomposites.

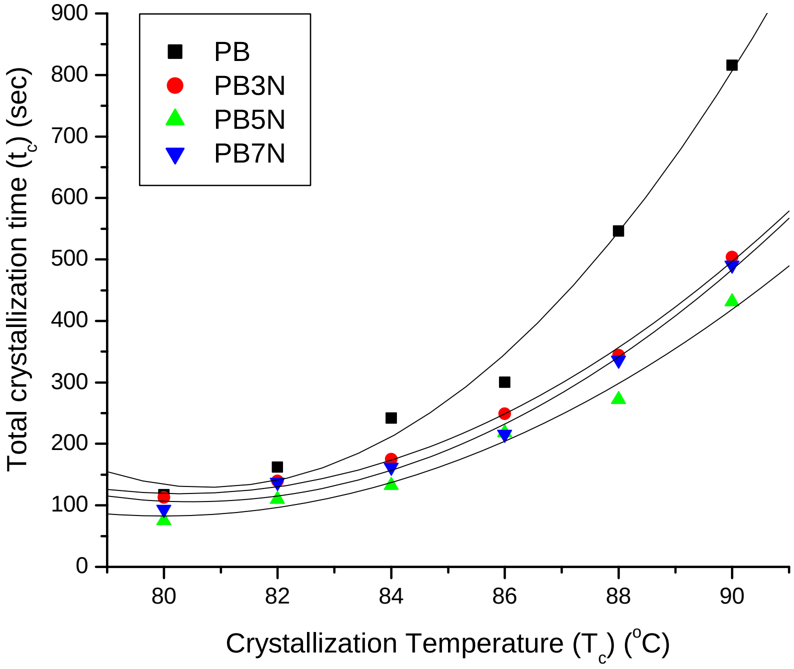

Figure 3.12: T_c vs t_c for PB and PB/clay nanocomposites

From the figure, it can be seen that the values of t_c are lower for nanocomposites than those for PB. The effect of clay on the crystallization is clearly observed at higher T_c compared to lower one. For example, the total crystallization time (t_c) at 84 °C for PB is

242 seconds while it decreased to 175, 132 and 162 seconds for PB3N, PB5N and PB7N nanocomposites respectively. The lower values of t_c suggest acceleration of crystallization process in nanocomposites as compared to PB.

3.3.2.2.1 Isothermal Crystallization Kinetics:

The Avrami equation is used to analyze the isothermal curves for the crystallization kinetics in PB and PB/clay nanocomposites. As explained earlier in section, 2.6.2.1 by plotting $\log[-\ln(1-X_t)]$ vs. log t, a straight line is obtained if the crystallization kinetics obeys the Avrami theory. The Avrami exponent (n) and the crystallization kinetic constant (K) (rate constant) are obtained from the slope and the intercept of the straight lines respectively. The rate constant derived from the plots, for PB is 1.05×10^{-4} (min^{-1}), while it increased to 1.8×10^{-4}(min^{-1}), 2.4×10^{-4} (min^{-1}) and 2.1×10^{-4} (min^{-1}) for PB3N, PB5N, and PB7N nanocomposites respectively at 84 °C. The values of Avrami exponent (n) are about 2, and are almost similar to those of PB. Isothermal crystallization is further analyzed using the spherulitic growth rate in the context of the Lauritzen – Hoffman secondary nucleation theory as explained in section 2.6.2.1.

Figure 3.13 shows the plots of $\ln(1/t_{1/2}) + U^*/R(T_c-T_\infty)$ versus $1/fT_c\,\Delta T$ for PB and PB/clay nanocomposites. The nucleation constant (K_g) values are determined from the slopes of the lines for PB and PB/clay nanocomposites. The K_g value for PB is 4.3×10^5 and it changes to 3.6×10^5, 4.6×10^5, and 4.0×10^5 for PB3N, PB5N, and PB7N nanocomposites respectively. As it is well known that a foreign surface frequently reduces the nucleus size needed for the crystal growth as the creation of the interface between polymer crystal and substrate may be less hindered than the creation of the corresponding free polymer crystal surface. A heterogeneous nucleation path makes the use of a foreign pre-existing surface to reduce the free energy opposing primary nucleation.

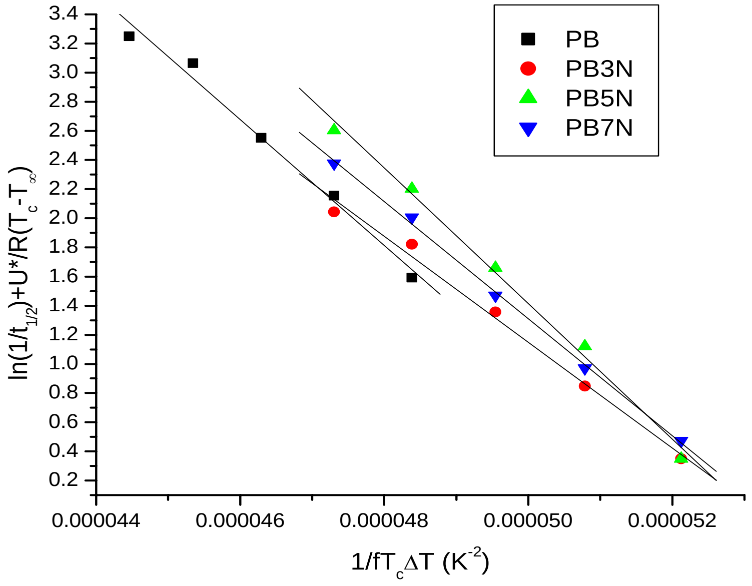

Figure 3.13: ln (1/$t_{1/2}$) + U*/R(T_c-T_∞) vs 1/fTc ΔT (K^{-2}) for PB and PB/clay nanocomposites

The lower values of K_g obtained in the present study thus can be ascribed to the heterogeneous nucleation of PB in the nanocomposites. Similar results are reported for PE/VMT nanocomposites [9].

3.3.2.2.2 Energy of Activation:

The energy of activation (E_a) is calculated from the slope of the graph [1/n ln K vs 1/T_c] for isothermal crystallization is shown in Figure 3.14. As explained in section 2.6.2.2,

ΔE_a is total activation energy, which consists of the transport activation energy ΔE^* and the nucleation activation energy ΔF. ΔE^* refers to the activation energy required to transport molecular segments across the phase boundary to the crystallization surface, while ΔF is the free energy of formation of critical size crystal nuclei at particular crystallization temperature.

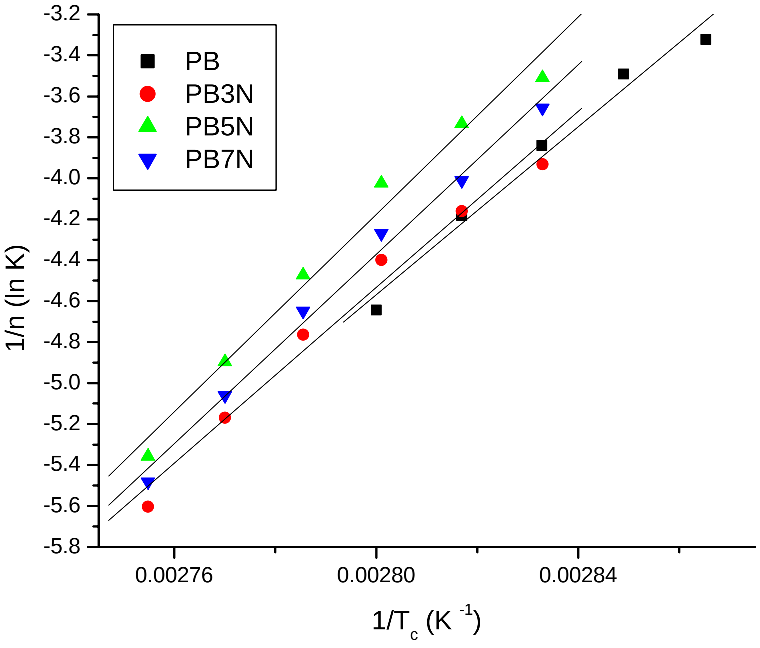

Figure 3.14: 1/n (ln K) vs 1/T_c for PB and PB/clay nanocomposites

The activation energy, E_a is found to change marginally because of incorporation of clay. The values of E_a are found to be about 170 kJ/mol for PB, and 178, 200 and 192 kJ/mol for PB3N, PB5N, and PB7N respectively. The increase in the activation energy for the nanocomposites can be ascribed to the hindered mobility of polymer chains due to presence of clay [10].

3.3.3 Optical Microscopy (OM):

As can be seen from Figure 3.15, pristine PB shows well-defined spherulitic morphology. In case of nanocomposites, the introduction of clay results in disturbed spherulitic morphology. PB3N shows the spherulitic morphology whereas for PB5N and PB7N the spherulitic morphology is hardly discernible. As the clay percent increased, the Maltese cross gradually disappeared.

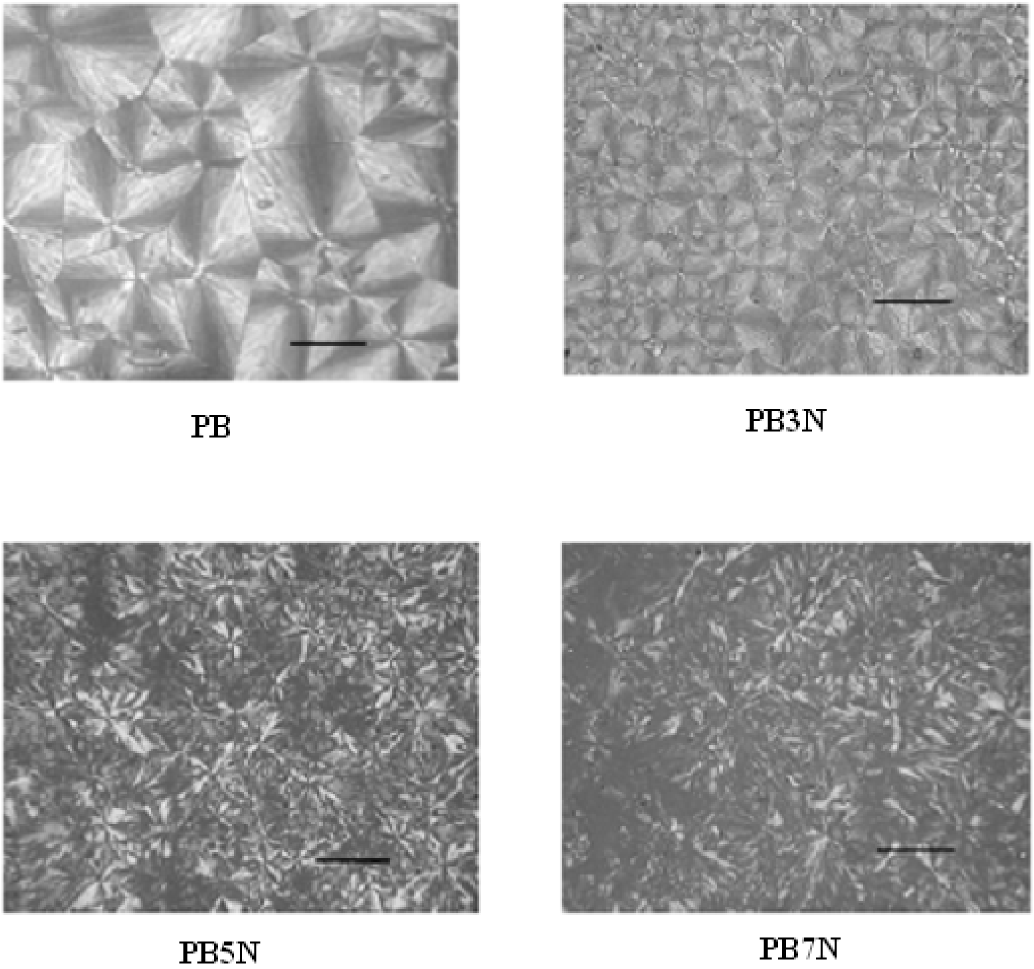

PB

PB3N

PB5N

PB7N

Figure 3.15: Optical micrographs for PB and PB/clay nanocomposites (Scale bar = 100 μm)

Generally, in case of polymer/clay nanocomposites, it has been observed that the clay layers serve as seeds for spherulitic growth and resulted in fine uniform, small size spherulites [11-12]. However, in our study, the effect clay is more significant on spherulitic structure rather than on the spherulitic size.

3.3.4 Phase transformation studies:

Differential Scanning Calorimetry is used to study the phase transformation of PB and PB/clay nanocomposites.

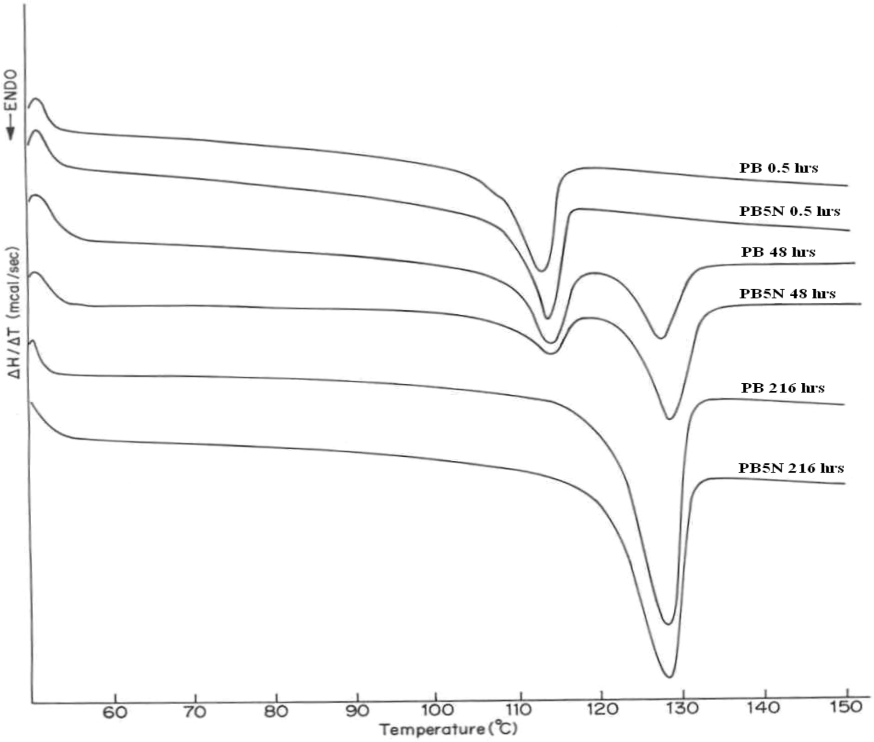

Figure 3.16:DSC thermograms illustrating the phase transformation for PB and PB5N nanocomposite

As stated earlier, DSC can be used to differentiate the various polymorphic forms of PB as they exhibit different melting points. As shown in figure 3.2, the endothermic peaks at about 128 and 114°C correspond to Form I and Form II respectively.

The phase transformation is studied by measuring the heat of fusion at various time intervals upon aging at room temperature. The DSC thermograms for various time intervals for PB and PB5N nanocomposites are shown in Figure 3.16. As the aging time increases the fraction of Form II transforms into Form I as evidenced by the decrease in heat of fusion of Form II. The fractional conversion for the nanocomposite at various time intervals is calculated as follows.

$$\text{Fractional conversion} = \frac{\Delta H_f \text{ of Form I at time 't'}}{\Delta H_f \text{ of Form I at 216 hrs}}$$

The fractional conversion as a function of time for PB5N is shown in Figure 3.17.

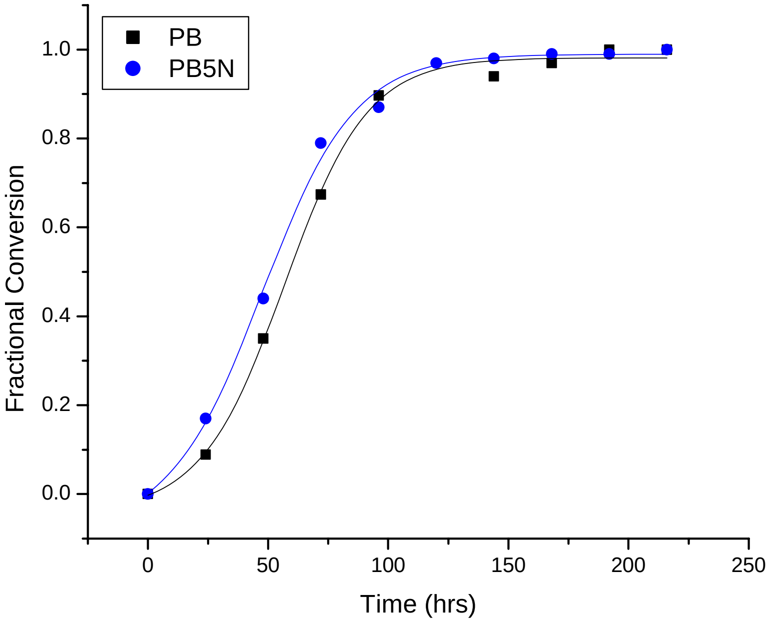

Figure 3.17: Fractional conversion of Form I for PB and PB5N nanocomposite

As can be seen from the figure the phase transformation is faster for the nanocomposite as compared to pristine PB.

The conversion to Form I for PB at 48 hrs is 35% while it increased to 44% for PB5N. After 96 hrs the conversions for PB and PB5N nanocomposites are found to be almost same. The kinetics of phase transformation is studied using Avrami theory and the rate constants are calculated. The rate constant K is 2.89 $x10^{-4}$ (hrs^{-1}) for PB and 8.52 $x10^{-4}$ (hrs^{-1}) for PB5N. This data clearly indicate that the transformation of PB from Form II to Form I take place faster in the presence of clay. The half time for phase transformation ($t_{0.5}$) value for conversion is about 50.6 hrs for PB5N and 54 hrs for PB7N, while it is about 58 hrs for PB. The Avrami exponent 'n' for all the nanocomposites are found to about 1.7 while that for PB is about 1.9. The enhancement in the rate of phase transformation is not significant as the half time for phase transformation changes from 58 hrs to 50.6 and 54 hrs for PB5N and PB7N nanocomposites.

3.3.5 Viscoelastic properties:

3.3.5.1 Dynamic mechanical analysis (DMA):

DMA is a suitable technique to study the dynamic response of the polymers under a given set of conditions. The storage modulus (E'), loss modulus (E''), and tan δ curves are used to generate information on the crystalline as well as amorphous nature in polymers. Figure 3.19 shows the storage modulus (E') of PB and PB/clay nanocomposites. At -50°C the storage modulus (E') for PB is about 2.9×10^{9} Pa, which decreases as the temperature increases and at 50°C, it drops down to 3.55×10^8 Pa. The sharp decrease in storage modulus at about -10°C corresponds to the onset of micro-Brownian motion with the short-range diffusional motion in the polymer.

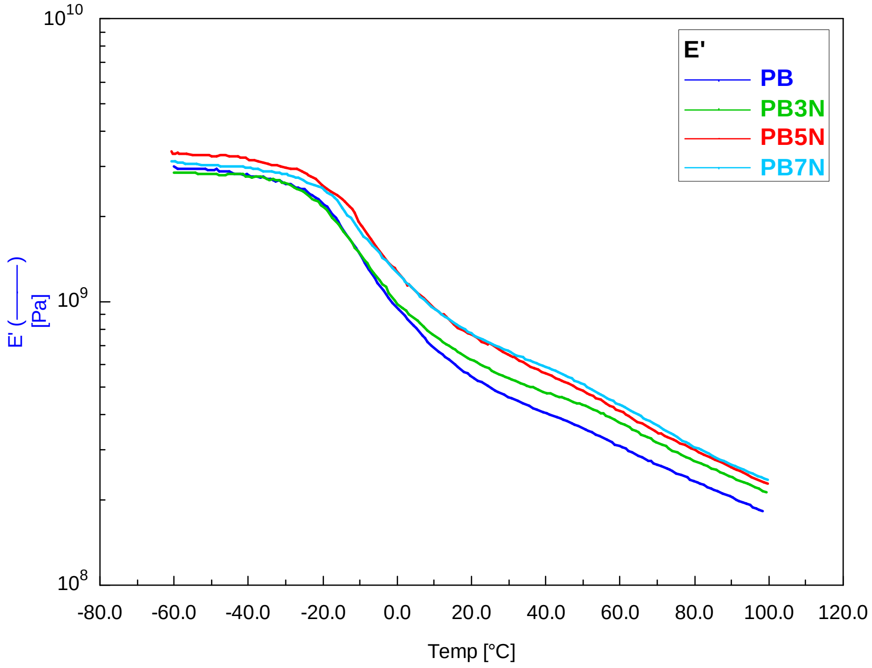

Figure 3.18: The storage modulus (E') curves for PB and PB/clay nanocomposites

The nanocomposites show higher values for the storage modulus in the rubbery regime. It is observed that, as the clay percent increases, the storage modulus also increases. At 100 °C the increase in storage modulus is 16, 24 and 29% for PB3N, PB5N and PB7N nanocomposites respectively. This increase in the storage modulus of the nanocomposites clearly illustrates the reinforcing effect of clay, which in turn could be ascribed to the higher aspect ratio of the clay layers. The organophilic clay layers get expanded as a result of intercalation of the polymer, thereby increasing the apparent aspect ratio of the clay layers. Similar increase in storage modulus is reported for other polymer nanocomposites [13-15]. The effect of clay layers on tan δ is given in Figure 3.20. It is apparent from figure that the tan δ values for nanocomposites are lower than that for PB.

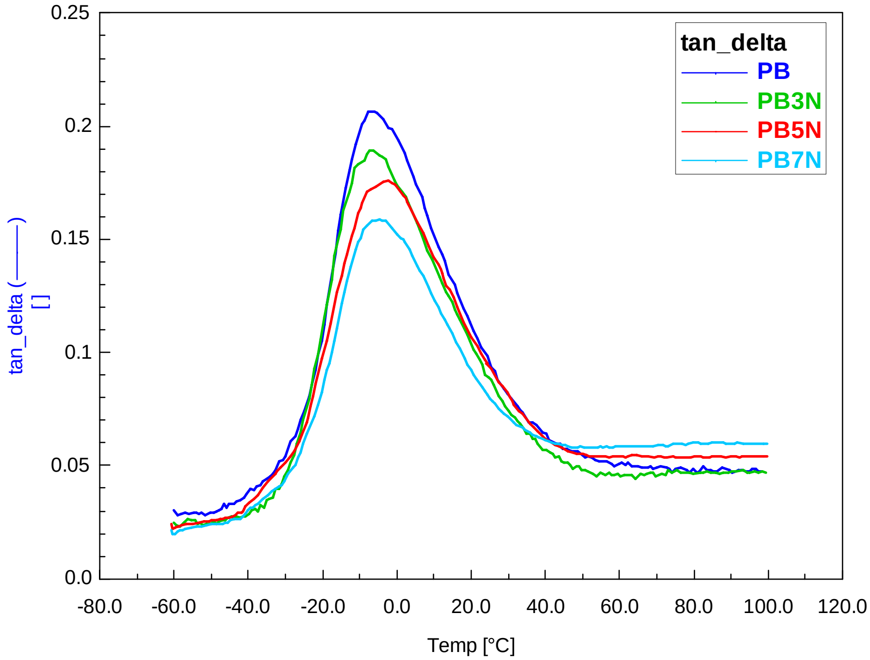

Figure 3.19: Tan δ curves for PB and PB/clay nanocomposites

The tan δ values are found to be about 0.18, 0.17, and 0.15 for PB3N, PB5N, and PB7N nanocomposites, while it is 0.21 for pristine PB suggesting decrease in damping due to incorporation of clay in the polymer matrix.

3.3.5.2 Melt Rheology:

The complex viscosity (η*) data from the dynamic frequency measurements is shown in Figure 3.20 for different clay content. The complex viscosity is increased with the clay content. The PB5N nanocomposite exhibited slightly higher values compared to PB7N nanocomposite. As can be seen from the figure, the plots exhibited same nature as that for pristine PB.

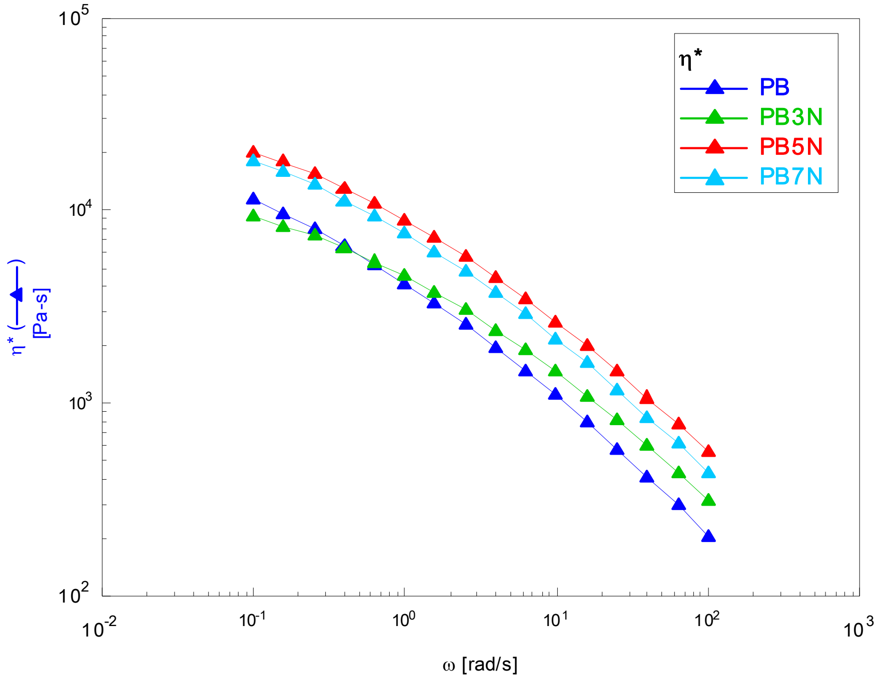

Figure 3.20: Complex Viscosities (η*) for PB and PB/clay nanocomposites

Figure 3.21 depicted the storage modulus (G') for PB and PB/clay nanocomposites. The storage modulus is increased with the content of clay. The higher values of η* for PB5N is attributed to the better dispersion of clay and the more number of polymer chains infiltrated compared to PB7N in the matrix as can be seen from XRD patterns, this data also supported by DSC, which shows higher T_c for PB5N compared to PB7N.

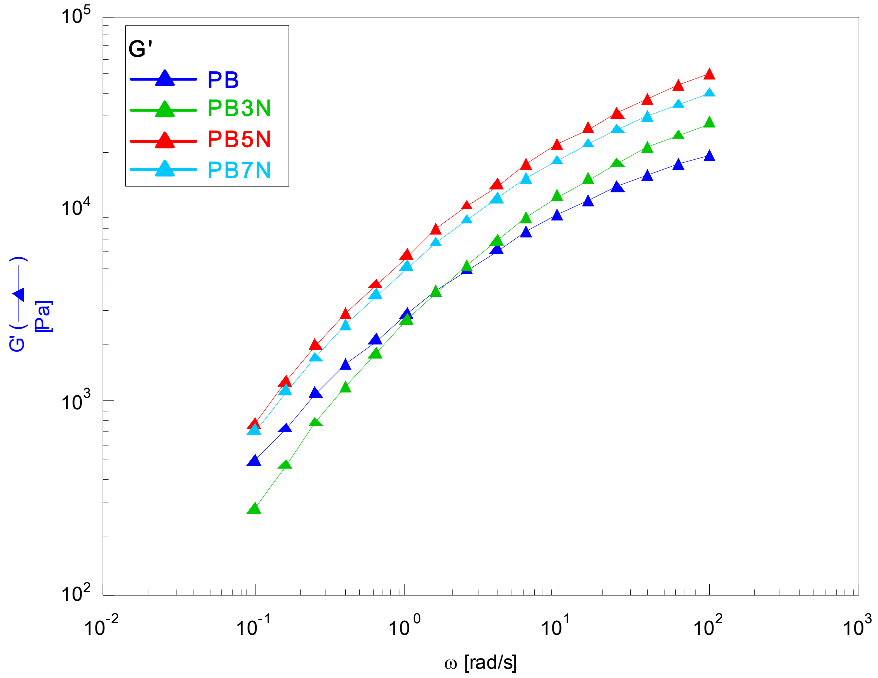

Figure 3.21: Storage modulus (G') for PB and PB/clay nanocomposites

In dynamic frequency tests the polymer shows liquid like behavior that is $G' \propto \omega^2$, $G'' \propto \omega$ in the low frequency terminal zone. It has been reported that due to reinforcement of clay in the polymer matrix, the response in the terminal zone changes. Generally when G' exceeds G" at lower frequency and found to be nearly independent of the lower frequencies suggests pseudo-solid like behavior. This low frequency response can be explained in terms of physical jamming of the clay layers due to their highly anisotropic nature. Due to this nature and geometric constraints, the layers exhibit local correlations. These local correlations cause the presence of domains and this results in the enhancement in storage modulus at lower frequencies. Such behavior is attributed to the formation of a mesoscale clay network at loadings above the percolation threshold. However, from the Figure 3.21 it is clearly seen that in this system the nanocomposites do not exhibit pseudo solid like behavior and flow like pure polymer in the low frequency region. Similar behavior is reported for other intercalated polymer/clay nanocomposites systems like PS/clay [16] and PI/clay nanocomposites [17].

3.3.6 Thermogravimetric analysis (TGA):

The Thermogravimetric analysis of PB and PB/clay nanocomposites is carried out in nitrogen atmosphere. Figure 3.22 shows the TGA thermograms for PB and PB/clay nanocomposites.

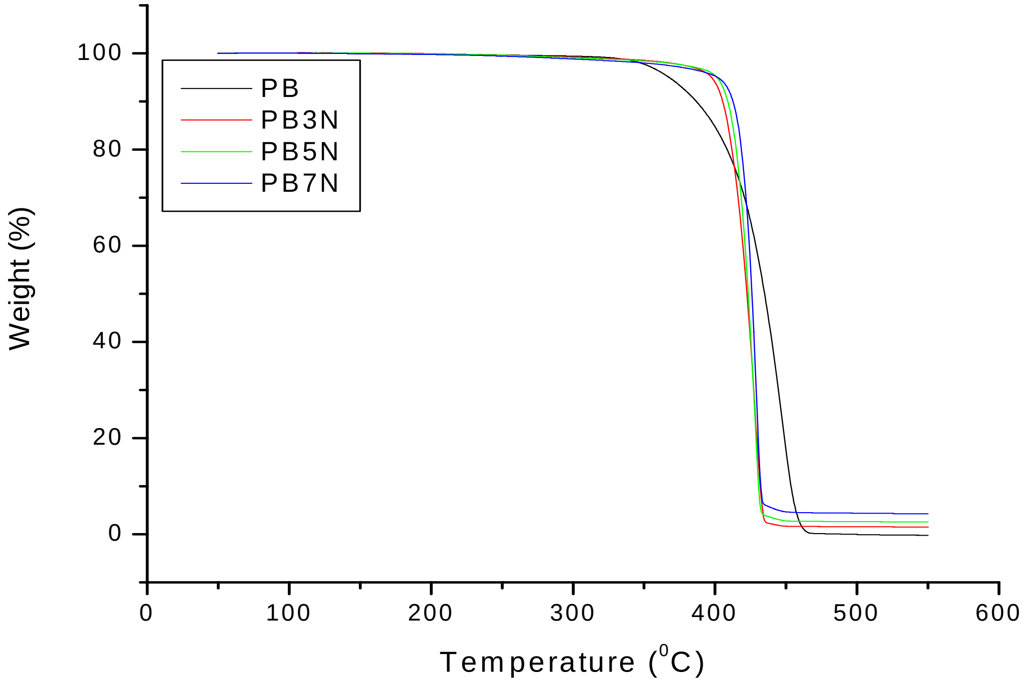

Figure 3.22: TGA thermograms for PB and PB/clay nanocomposites

As can be seen from the figure the onset of temperature of degradation initiation (TDI) increases by about 23 °C, 28 °C and about 33 °C for PB3N, PB5N, and PB7N nanocomposites respectively. The increase in the temperature suggests delay in degradation of PB/clay nanocomposites and can be ascribed to the dispersion of clay layers. Similar results have been reported for other polymer/clay nanocomposites [18].

3.4 Conclusions:

Nanocomposites of PB with organically modified clay are prepared using melt intercalation technique. The X- ray diffraction patterns portray the intercalated structure for the melt processed PB/clay nanocomposites and the transmission electron micrographs reveal the dispersion of clay layers. The non-isothermal crystallization studies exhibits enhanced crystallization in presence of clay as evidenced by the higher values for Z_t and lower values for F(T) and $t_{1/2}$. Energy of activation is found to be slightly lower for PB3N while it increases as the content and found higher than that of pristine PB. The nucleating activity of nanocomposites is found to be about 0.88-0.9. The isothermal crystallization study shows reduction in total crystallization time and higher crystallization rates suggesting enhanced crystallization. The energy of activation for isothermal crystallization is found to be higher than that of pristine PB. In optical microscopic studies, a slight reduction in spherulitic size is observed for PB3N while for higher clay contents, disturbed and disordered spherulite structures are found. The rate of crystal-to-crystal phase transformation is enhanced as result of incorporation of clay. The dynamic mechanical analysis exhibits higher storage modulus for the nanocomposites due to reinforcement by clay. In thermogravimetric analysis, an increase in degradation initiation temperature attributed to the clay layers acting as a diffusion barrier. The increase of volatilization rate at higher temperature is due to the catalytic degradation activity of zeolitic structure (such as that exhibited by the clays) on hydrocarbon moieties, which overcomes the barrier effect at the temperature at which extensive degradation occurs.

References:

[1] Nakamura K, Aoike T, Usaka K, Kanamoto T. Macromolecules, 32, 4975 **(1999)**

[2] Liu X, Wu Q. Polymer, 43(6), 1933 **(2002)**

[3] Priya L, Jog J. J Polym Sci Part B: Polym Phys, 40(15), 1682 (**2002)**

[4] Xu w, He P, J Polym Sci Part B: Polym Phys,, 40, 408, **(2002)**

[5] Liu T, Mo Z, Wang S, Zang H. Polymer Engineering and Science 37, 568 **(1997)**

[6] Hu X, Lesser A. Macromolecular chemistry and physics 205, 574-580 **(2004)**

[7] Dobreva A, Gutzow I. J Non Cryst Solids, 162, 13 **(1993)**

[8] Kim SH, Ahn SH, Hirai T. Polymer,; 44, 5625 **(2003)**

[9] Tjong S, Bao S. Journal of polymer Science part B Polymer Physics 43, 253**(2005)**

[10] Wu TM, Liu CY. Polymer; 46, 5621 **(2005)**

[11] Priya L. Ph.D. thesis University of Pune **(2005)**

[12] Wu Z, Zhou C, Zhu N. Polymer Testing, 21,479 **(2002)**

[13] Messersmith P, Giannelis E. Chem Mater, 6,1719 **(1994)**

[14] Kodgire P, Kalgaonkar R, Hambir S, Bulakh N, Jog J. J Apply Polym Sci, 81,1786 **(2001)**

[15] Hambir S, Bulakh N, Kodgire P, Kalgaonkar R, Jog, J. J Polym Sci Part B: Polym Phys, 39, 446 **(2001)**

[16] Lim Y, Park O. Rheologica Acta, 40, 220 **(2001)**

[17] Jeon H, Rameshwaram J, Kim G, Weinkauf D. Polymer, 44, 5749 **(2003)**

[18] Burnside, S, Giannelis E. Chem Mater, 7,1597 **(1995)**

Chapter 4

PB/Multiwalled Carbon Nanotubes Nanocomposites

The work presented in this chapter has been published in the following journals

1] Wanjale SD, Jog JP. Polymer, 47, 6414 (2006)

2] Wanjale SD, Jog JP. Journal of Macromolecular Science: Part B: Physics, 45, 1053 (2006)

4.1 Introduction:

This chapter presents study of poly(1-butene)/multiwalled carbon nanotube (MWCNT) nanocomposites. The unique structure and properties of carbon nanotubes offer promising potential for developing novel, smart, and advanced materials [1-5]. Here we discuss the effect of MWCNT on the crystallization, phase transformation, thermo-mechanical, and dielectric properties of PB.

4.2 Multiwalled Carbon Nanotubes (MWCNT):

The multiwalled carbon nanotubes are used for the preparation of nanocomposites. These MWCNTs have internal diameter of 5-10 nm, outer diameter of 10-20 nm, and length about 0.5-200 μm. The MWCNTs with 95+% purity are procured from Aldrich. The MWCNTs are prepared by chemical vapor deposition method. The surface area measured by BET method is 40-600 m^2/g. The density is 2.1g/cc while the bulk density is very low around 0.04-0.05 g/cc. The melting of these nanotubes ranges from 3652 - 3697 °C (as per company data sheet).

4.2.1 X -ray diffraction (XRD):

X - ray diffraction pattern for MWCNTs is shown in figure 4.1. A characteristic peak at 11.7° for the MWCNTs represents the average intershell distance [6]. A sharp peak at 2θ values of 26° (002), and other two peaks at 45° (101), 53° (004) are due to the ordered concentric cylinders of graphitic carbon [7].

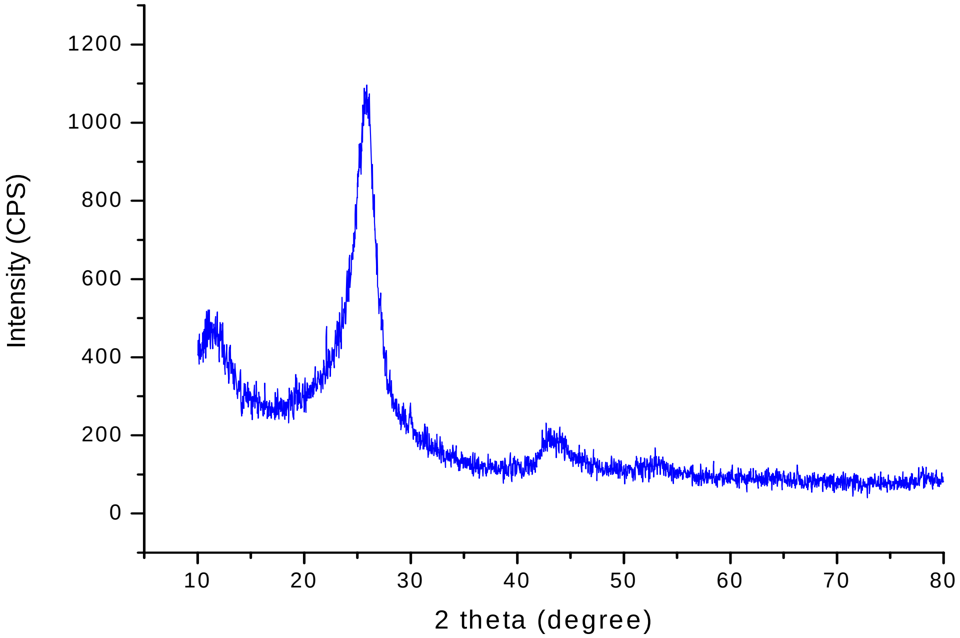

Figure 4.1: X - ray diffraction pattern for MWCNT

4.2.2 Morphology:

The scanning electron and transmission electron micrographs for MWCNT are shown in figure 4.2 and 4.3 respectively. The micrograph of carbon nanotubes shows the entanglements and formation of the bundles. The diameter of the nanotubes is varying from 20 to 50 nm while the length is in few microns.

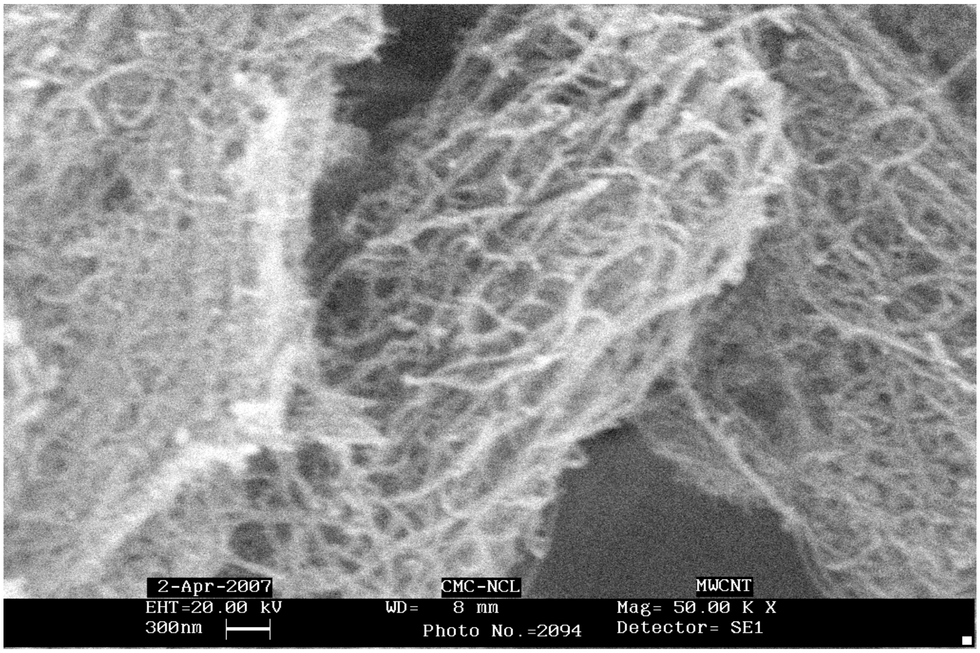

Figure 4.2: Scanning electron micrograph for MWCNT

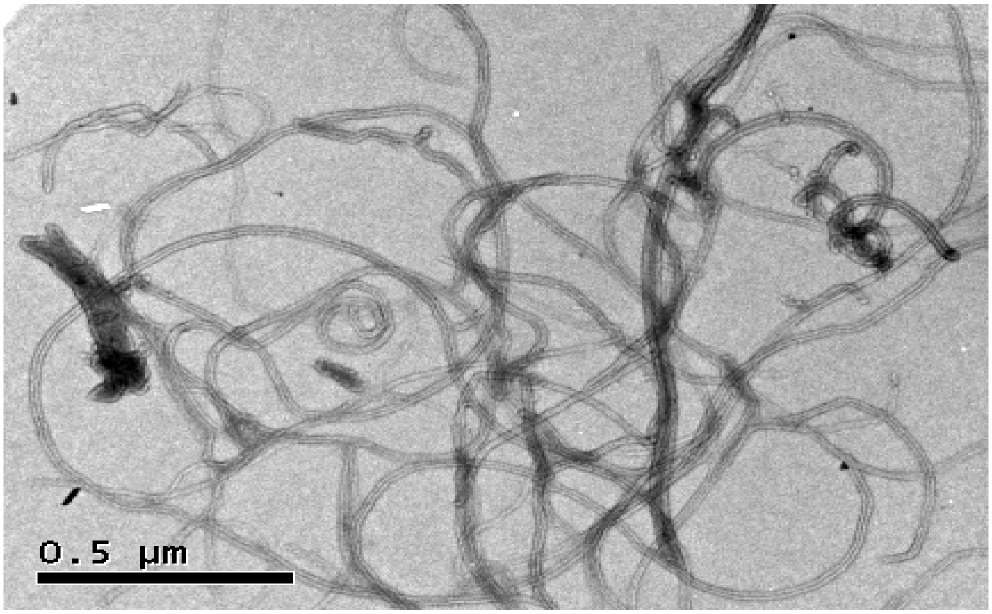

Figure 4.3: Transmission electron micrograph for MWCNT

4.2.3 Thermogravimetric analysis (TGA):

The thermal stability of the carbon nanotubes in the nitrogen atmosphere is estimated using thermogravimetric analysis. The multiwalled carbon nanotubes exhibit high thermal stability over the temperature range studied and show only 5% weight loss up to 700°C.

4.3 Results and discussion:

4.3.1 Morphology:

4.3.1.1 Scanning Electron microscopy (SEM):

The SEM micrographs of two magnifications for PB7C nanocomposite are shown in figures 4.4 A and 4.4 B. Nanotubes have tendency to bundle due to the substantial van der Waals attractions between them. In addition, their large aspect ratio causes them to agglomerate to microscopic bundles and even microscopic particles. The nanotube bundles or particles have significantly lower aspect ratio and thus exhibit lower mechanical properties [8]. The lower aspect ratio is also likely to lead to higher percolation thresholds for electrical and thermal conductivity [8]. Figure 4.4 A clearly show the white patches of varying size of aggregates of MWCNTs and some individual nanotubes that are dispersed in the polymer matrix. Non-polar nature of polymer and weak interactions between nanotubes and the matrix might result in the formation of aggregates. The wrapping of the polymer matrix around the nanotube surface is clearly seen using higher magnification (figure 4.4 B). Similar results are reported for various polymer/carbon nanotubes nanocomposites [9-11].

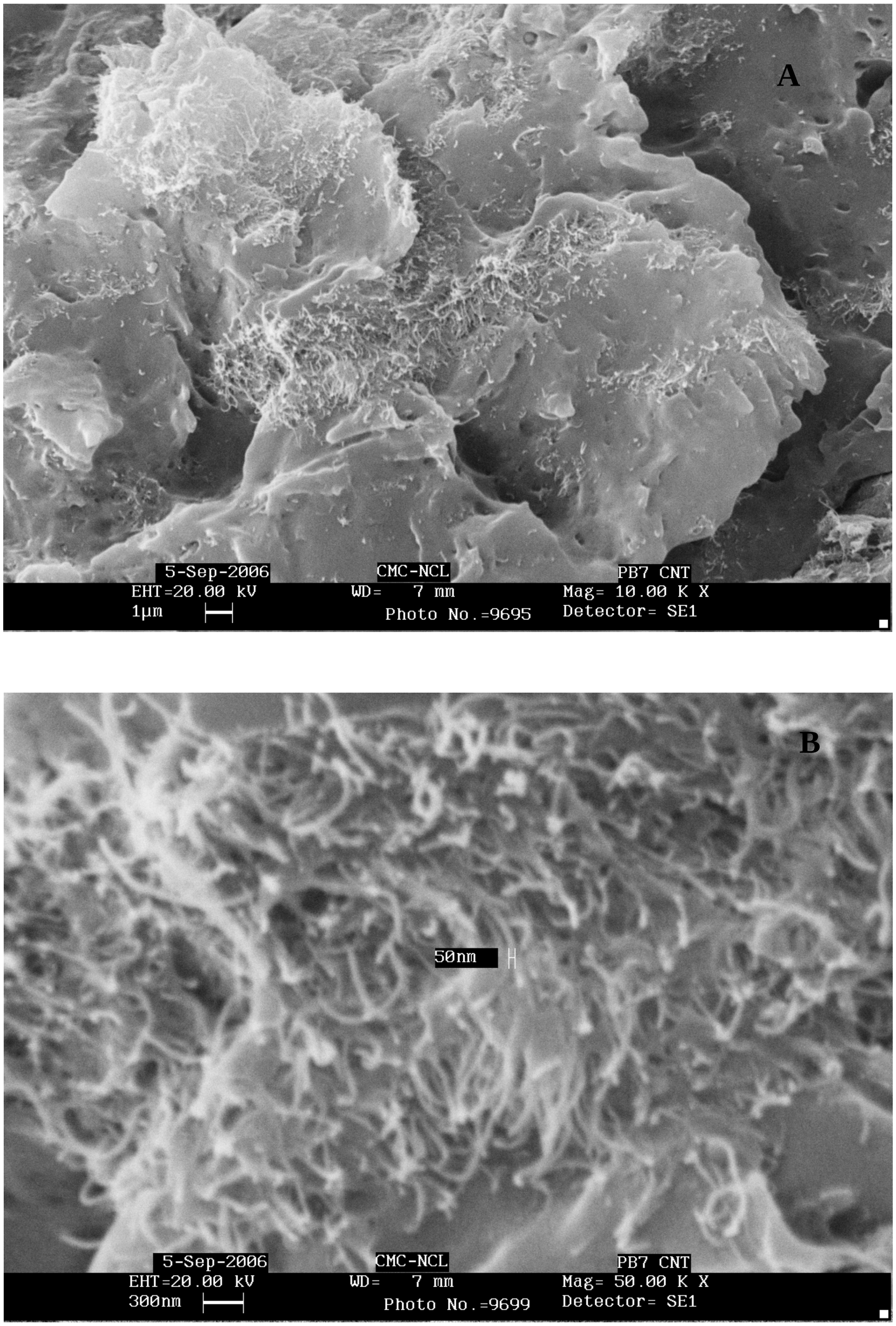

Figure 4.4: Scanning electron micrographs for PB7C (A) (×10K) and (B) (×50K)

4.3.2 Crystallization Studies:

4.3.2.1 Non-isothermal Crystallization:

Table 4.1 shows melting temperature (T_m), crystallization temperature (T_c), and Heat of fusion (ΔH_f) for PB and PB/MWCNT nanocomposites.

Table 4.1: Melting and crystallization parameters for PB and PB/MWCNT nanocomposites

Sample	T_m (°C)	T_c (°C)	ΔH_f (J/g)
PB	128.9	69.8	68.9
PB3C	130.2	83.6	69.6
PB5C	129.9	84.6	74.2
PB7C	130.1	84.9	74.6

The PB5C and PB7C nanocomposites show higher ΔH_f than that of PB while for PB3C, ΔH_f is comparable to that of PB. The crystallization temperature is increased by about 13 °C for PB3C and by 15 °C for PB5C and PB7C, suggesting heterogeneous nucleation for PB due to incorporation of MWCNTs in PB matrix.

The effect of different cooling rates and MWCNT content on the non-isothermal crystallization of PB is studied. The crystallization parameters at different cooling rates are shown in Table 4.2. As can be seen from the table, with an increase in the cooling rate, a decrease in crystallization temperature (T_c) for both PB and nanocomposites is observed. However, at a given cooling rate, the T_c for the nanocomposites is found to be higher than pristine PB due to incorporation of MWCNT. The increase in crystallization temperature can be ascribed to the enhanced nucleation induced by MWCNTs.

Table 4.2: Non-isothermal crystallization parameters for PB and PB/MWCNT Nanocomposites (modified Avrami analysis)

Sample	ϕ (°C /min)	$t_{1/2}$ (min)	T_c (°C)	n	Z_t (min $^{-1}$)	Z_c
PB	2.5	1.5	79.4	4.2	4.99×10^{-3}	0.12
	5	1.1	74.3	4.5	5.28×10^{-2}	0.56
	10	1.0	69.8	4.6	0.54	0.94
	20	0.9	62.9	4.2	3.48	1.06
PB3C	2.5	1.4	91.8	3.7	1.38×10^{-2}	0.18
	5	1.0	87.5	4.4	0.156	0.69
	10	0.9	83.6	4.4	1.328	1.03
	20	0.9	76.7	3.8	9.055	1.12
PB5C	2.5	1.4	92.8	4.8	9.77×10^{-3}	0.16
	5	1.0	88.9	4.6	0.1022	0.63
	10	0.9	84.6	4.1	1.557	1.05
	20	0.9	77.7	3.6	8.596	1.11
PB7C	2.5	1.3	92.8	4.7	0.02	0.19
	5	1.0	89.6	4.8	0.08	0.61
	10	0.9	84.9	4.6	1.07	1.01
	20	0.8	79.3	4.1	7.75	1.11

4.3.2.1.1 Non-Isothermal Crystallization Kinetics:

The non-isothermal crystallization kinetics is studied using modified Avrami theory as discussed in section 2.5.3.1.

The non-isothermal crystallization parameters calculated from the plots of log [-ln (1-X_t)] vs. log t are presented in Table 4.2. The values of Z_t are found to increase while values of

$t_{1/2}$ decrease with an increase in the cooling rates for PB and PB/MWCNT nanocomposites. The higher values of Z_t and the lower values of $t_{1/2}$ for the nanocomposites, as compared to pristine PB, signify the enhanced rate of crystallization for PB in the nanocomposites.

A combined Avrami-Ozawa equation is used for analyzing the non-isothermal crystallization kinetics of PB and the PB/MWCNT nanocomposites. The log ϕ vs. log t plots shows linear relationship at a given relative degree of crystallinity. Table 4.3 presents values of F(T) and 'a' calculated from the graphs shown in Figure 4.5.

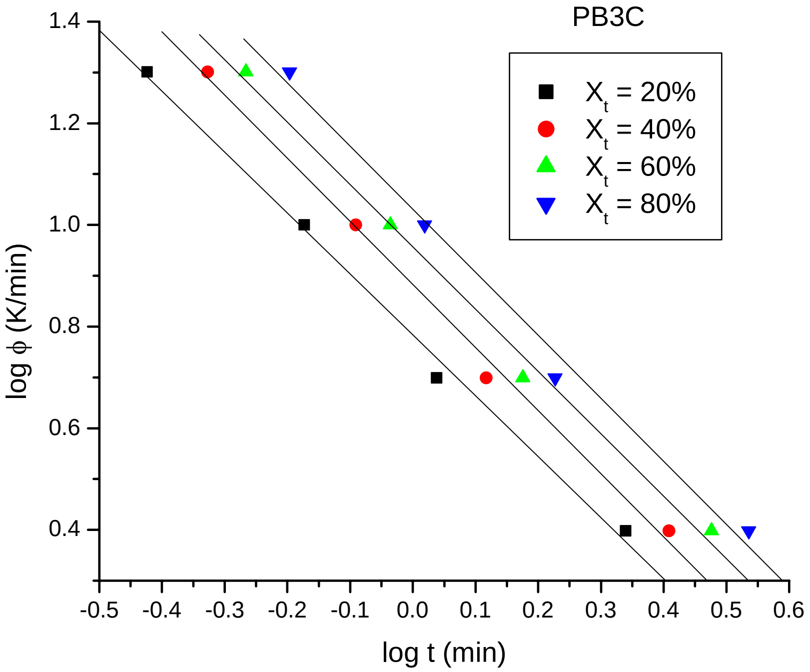

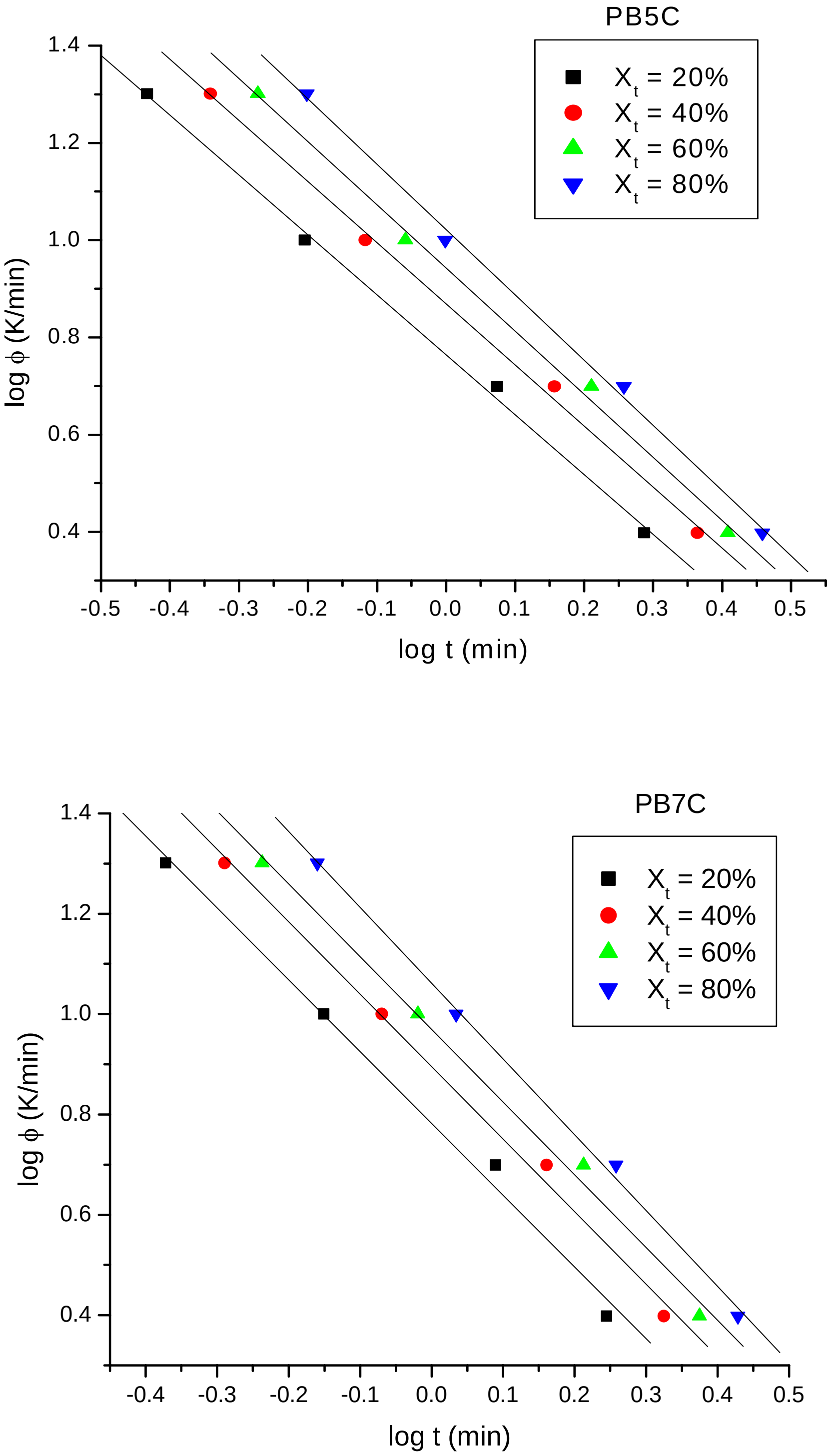

Figure 4.5: log ϕ vs log t for PB/MWCNT nanocomposites

Table 4.3: Non-isothermal crystallization parameters for PB and PB/MWCNT nanocomposites (combined Avrami – Ozawa analysis)

Sample	X_t (%)	F(T)	'a'
PB	20	8.0	1.3
	40	10.3	1.3
	60	12.2	1.3
	80	14.7	1.3
PB3C	20	6.1	1.2
	40	7.6	1.2
	60	9.1	1.2
	80	10.7	1.2
PB5C	20	5.8	1.2
	40	7.4	1.3
	60	8.8	1.3
	80	10.5	1.3
PB7C	20	6.1	1.4
	40	7.9	1.4
	60	9.3	1.4
	80	11.5	1.5

It can be seen that the F(T) values for PB and nanocomposites increases with an increase in the relative degree of crystallization, suggesting that the time required for reaching the finite degree of crystallization increases for a given cooling rate. However, the lower values of F(T) for nanocomposites clearly signifies that the time required for reaching a certain degree of crystallization is lower in case of nanocomposites compared to the time required for the same degree of crystallization for pristine PB. The values of Avrami-

Ozawa exponent ‘a’ are found to be 1.3 and 1.2 to 1.5 for all the cooling rates for PB and PB/MWCNT nanocomposites.

4.3.2.1.2 Energy of Activation:

From the non-isothermal crystallization study, it has been observed that the crystallization temperature is significantly increased by about 15°C for PB7C nanocomposite, while from the kinetics it is revealed that the rate of crystallization is enhanced due to incorporation of MWCNTs. The non-isothermal crystallization activation energy is calculated by using the Kissinger equation as described in 2.5.3.2 section.

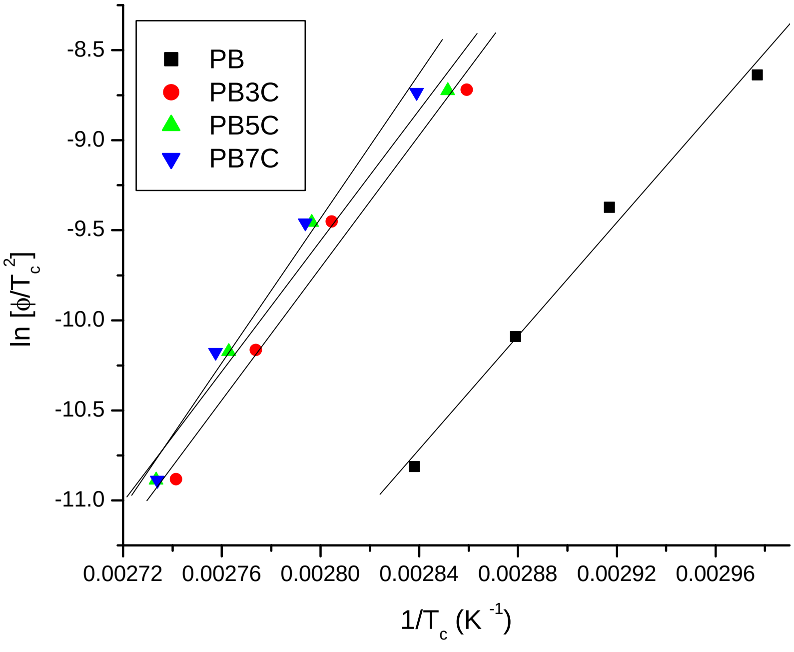

Figure 4.6: ln [ϕ/T_c^2] vs 1/T_c plots for PB and PB/MWCNT nanocomposites

Figure 4.6 shows the plot of ln(ϕ/T_c^2) vs (1/T_c). From the slopes, the activation energies are calculated. Energy of activation for PB is found to be about 131 kJ/mol, while it increased to 153, 151 and 167 kJ/mol for PB3C, PB5C, and PB7C nanocomposites respectively. The increase in activation energy for the nanocomposites indicates that the incorporation of MWCNTs impedes the chain transportation to the growing crystal surfaces. Although an increase in activation energy is observed, the other results such as F(T) and Z_t indicate increase in the rate of crystallization. These results also suggest that the incorporation of MWCNTs have significant effect on nucleation rather than growth. Similar increase in energy of activation is observed as the content of MWCNT increased for the PEN/MWCNT nanocomposites by Kim et al [12]. They suggested that MWCNT act as nucleating agent. Thus, accelerating non-isothermal crystallization and may adsorb PEN molecular segments restricting the movement of polymer chains.

4.3.2.1.3 Nucleating Activity:

The nucleating activity of the MWCNT is determined by the method used by Dobreva and Gutzow as discussed in section 2.5.3.3.

The nucleating activity (Φ), is determined from the slopes of linear function log ϕ as the function of $1/\Delta T_c^2$ (Figure 4.7). It has been stated that for active surface, Φ tends to zero while it tends to one, the surface is considered as an inert surface for nucleation.

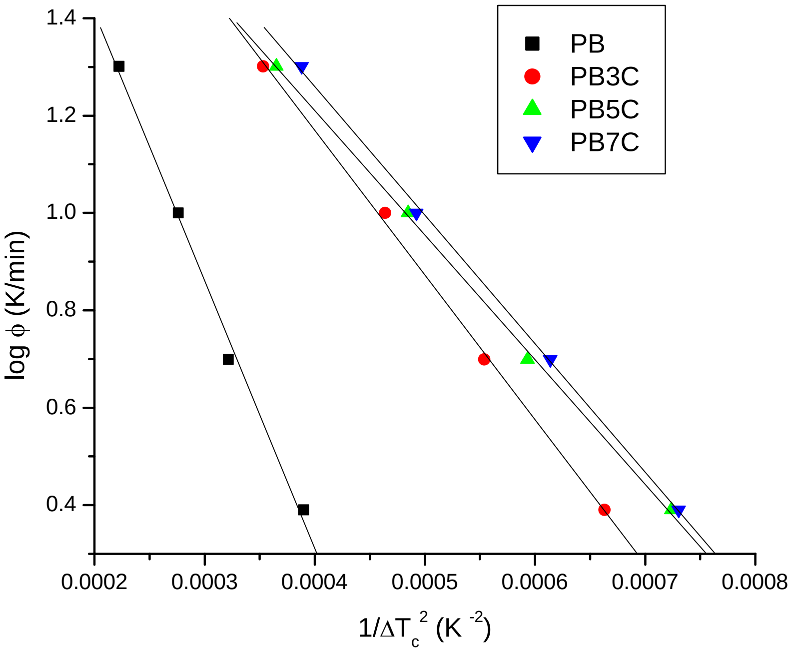

Figure 4.7: log ϕ vs $1/\Delta T_c^2$ for PB and PB/MWCNT nanocomposites

The nucleating activity is found to be 0.540, 0.465, and 0.479 for PB3C, PB5C, and PB7C nanocomposites respectively, which signifies that MWCNTs offer an active surface for nucleation.

4.3.2.2 Isothermal Crystallization:

Isothermal crystallization is studied in the temperature range of 82-90 °C and 86-94 °C for PB and PB/MWCNT nanocomposites respectively. The isothermal crystallization of PB and the nanocomposites is strongly affected by temperature of crystallization (T_c). As the T_c increases, the exothermic peak shifts to the higher value and broadens. Thus, the time required to reach the maximum degree of crystallization is increased with increase in T_c. It signifies that the rate of crystallization decreases with increase in T_c. The influence of T_c is similar for both PB and the nanocomposites. However, presence of

MWCNTs reduces the time required to reach the maximum degree of crystallization in nanocomposites, signifies an increase in crystallization rate.

4.3.2.2.1 Isothermal Crystallization kinetics:

Avrami equation is used to analyze the isothermal curves for the crystallization kinetics in PB and PB/MWCNT nanocomposites. The total crystallization time (t_c), and the rate constant (K) are calculated from the plots.

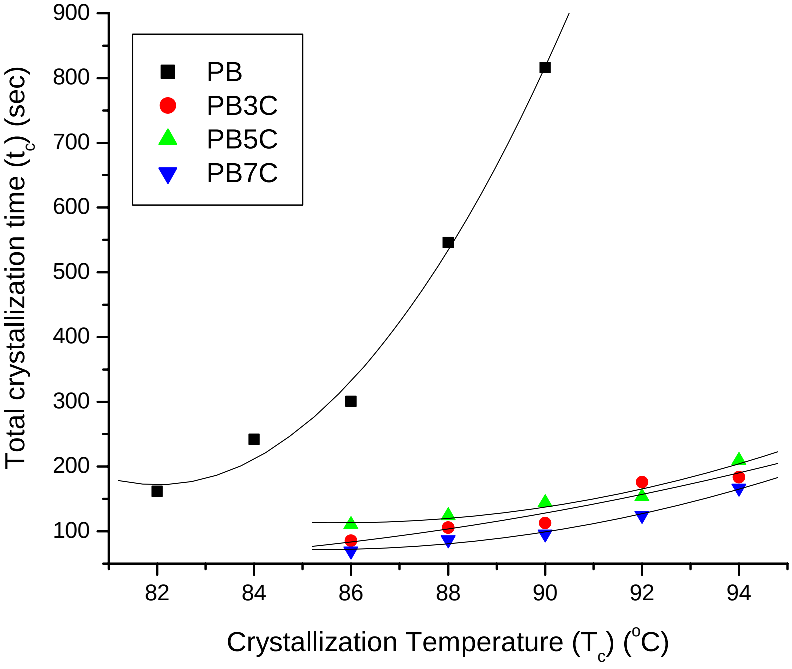

Figure 4.8: Total crystallization time (t_c) for PB and PB/MWCNT nanocomposites

Figure 4.8 depicts the variation of t_c with T_c. As can be seen from the figure, t_c increases with the increase in T_c for PB as well as PB/MWCNT nanocomposites. However, it can be observed that at comparable temperatures of crystallization, the t_c for the nanocomposites is much lower than those observed for pristine PB. This reduction in the total crystallization time indicates enhanced crystallization rate in presence of MWCNT. The value of rate constant (K) at 86°C is found to be 1.03×10^{-4} (min^{-1}) for PB and it increased to 1.05×10^{-3} (min^{-1}), 1.92×10^{-3} (min^{-1}), and 2.84×10^{-3} (min^{-1}), for PB3C, PB5C, and PB7C nanocomposites respectively. The total crystallization time (t_c) for PB at 86 °C is 300 seconds while it reduced to 85, 110 and 70 seconds for PB3C, PB5C, and PB7C nanocomposites respectively. These results confirm the enhanced crystallization of PB in presence of MWCNT. These results are similar with those reported by Wiemann et al [13] on the crystallization of sPP.

Figure 4.9 shows the graph from Lauritzen – Hoffman equation and the K_g values are determined from the slopes of the lines for PB and PB/MWCNT nanocomposites. The K_g value for PB is 4.3×10^5 and it decreases to 2.9×10^5, 2.5×10^5 and 3.1×10^5 for PB3C, PB5C and PB7C nanocomposites respectively. It is well known that a foreign surface reduces frequently the nucleus size needed for crystal growth. Since, the creation of the interface between polymer crystal and substrate may be less hindered than the corresponding free polymer crystal surface. A heterogeneous nucleation path makes the use of a foreign pre-existing surface to reduce the free energy opposing primary nucleation because of which the K_g decreases as the amount of filler increased. The lower values of K_g obtained in the present study thus can be ascribed to the heterogeneous nucleation of PB in the nanocomposites.

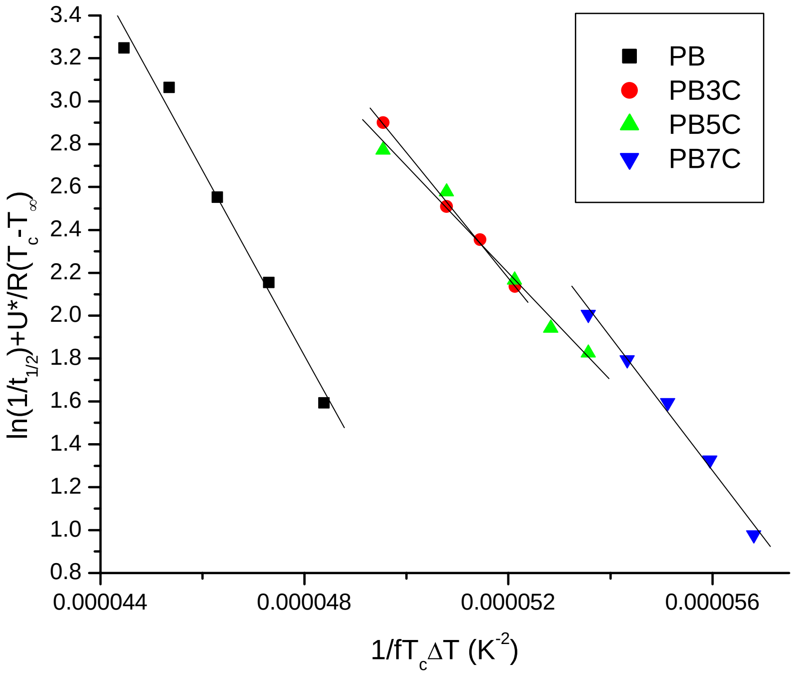

Figure 4.9: ln $(1/t_{1/2})$ + $U^*/R(T_c-T_\infty)$ vs 1/fTc ΔT (K^{-2}) for PB and PB/MWCNT nanocomposites

4.3.2.2.2 Energy of Activation:

The energy of activation (E_a) is calculated from the slope of the graph [1/n ln K vs $1/T_c$] for isothermal crystallization (Figure 4.10). The activation energy, E_a is found to change marginally due to the incorporation of MWCNT. The values of E_a are found to be about 170 kJ/mol for PB, while it was 150, 149 and 182 kJ/mol for PB3C, PB5C and PB7C respectively.

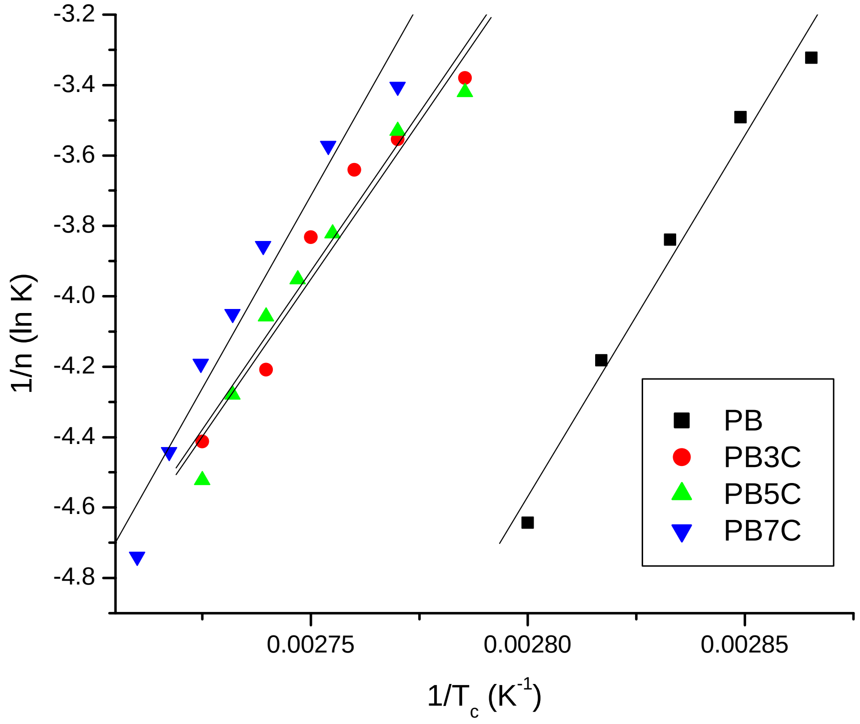

Figure 4.10: 1/n (ln K) vs 1/T_c for PB and PB/MWCNT nanocomposites

The non-isothermal crystallization studies confirm the nucleating activity of MWCNT and higher crystallization rate of PB in the nanocomposites. The isothermal crystallization results also support these findings as evidenced by the lower total crystallization times and increase in crystallization temperature. The decrease in the K_g values and marginal changes in the energy for activation imply that the observed increase in the overall crystallization rate can be ascribed to the enhanced nucleation in PB/MWCNT nanocomposites.

4.3.3 Optical Microscopy (OM):

Figure 4.11 shows the optical micrographs for PB, PB/MWCNT nanocomposites.

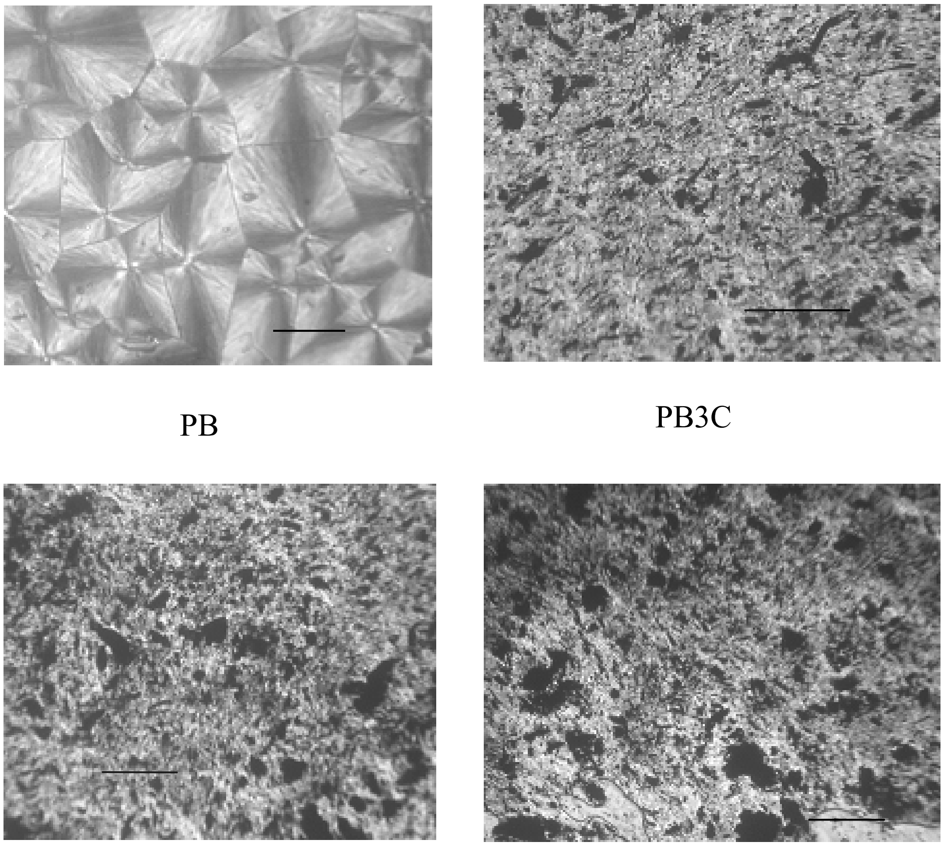

PB

PB3C

PB5C

PB7C

Figure 4.11: Optical micrographs for PB and PB/MWCNT nanocomposites (Scale bar = 100μm)

As can be seen, from the micrographs pristine PB shows well-defined spherulitic morphology while in case of nanocomposites very small crystalline structures are observed. This suggests that the dispersion of MWCNTs in the polymer matrix hinders the formation of ordered crystallites of Form II. The inherent morphology of spherulites of the pristine polymer is not observed due to increase in number of nucleation sites. This observation can be ascribed as heterogeneous nucleation in presence of MWCNTs. Kodjie et al reported similar results in case of HDPE/CNT nanocomposites [14].

4.3.4 Phase transformation studies:

4.3.4.1 Phase transformation study by DSC:

It is reported that the rate of phase transformation is maximum at room temperature (25°C) [15]. Although the mechanism of this transformation is not yet fully understood, it is proposed that the form I grow by pulling in the molecular chains from the surrounding form II crystals creating new stems of form I rather than growing stem-by-stem [16].

Here we have studied the phase transformation of PB and PB nanocomposite at room temperature by measuring the heat of fusion for the two forms at various time intervals. Figure 4.12 illustrates the heating scans for melt crystallized PB and PB7C samples. Both samples exhibit two peaks corresponding to the melting of Form I and Form II. As the aging time increases, the area under the lower temperature peak decreases and the area under the higher temperature peak (128 °C, which corresponds to form I) increases. The fractional conversion is calculated using heat of fusion values for Form I at different time intervals as follows.

$$\text{Fractional conversion} = \frac{\Delta H_f \text{ of Form I at time 't'}}{\Delta H_f \text{ of Form I at 216 hrs}}$$

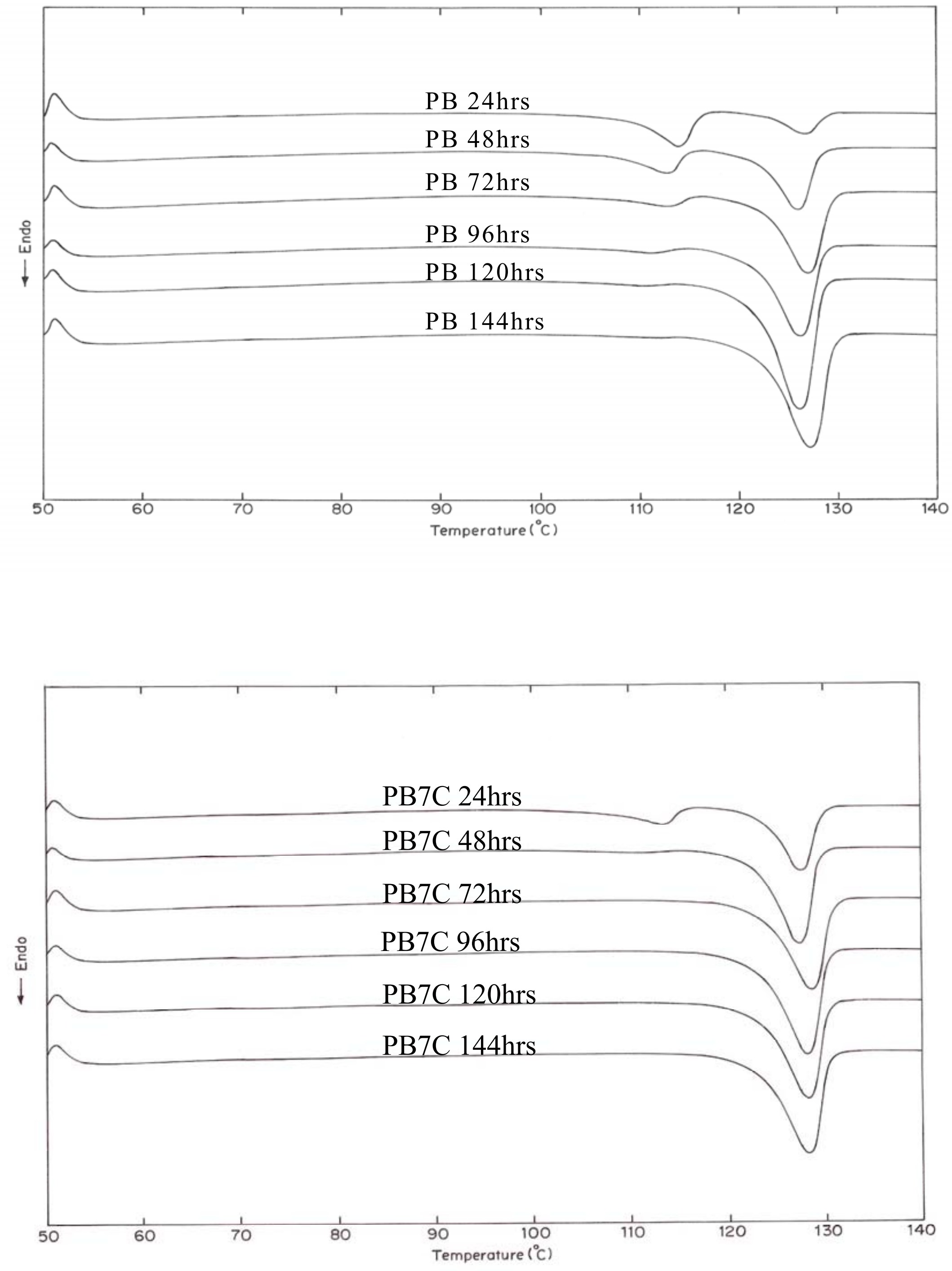

Figure 4.12: DSC thermograms illustrating the phase transformation at different time intervals for PB and PB7C nanocomposite

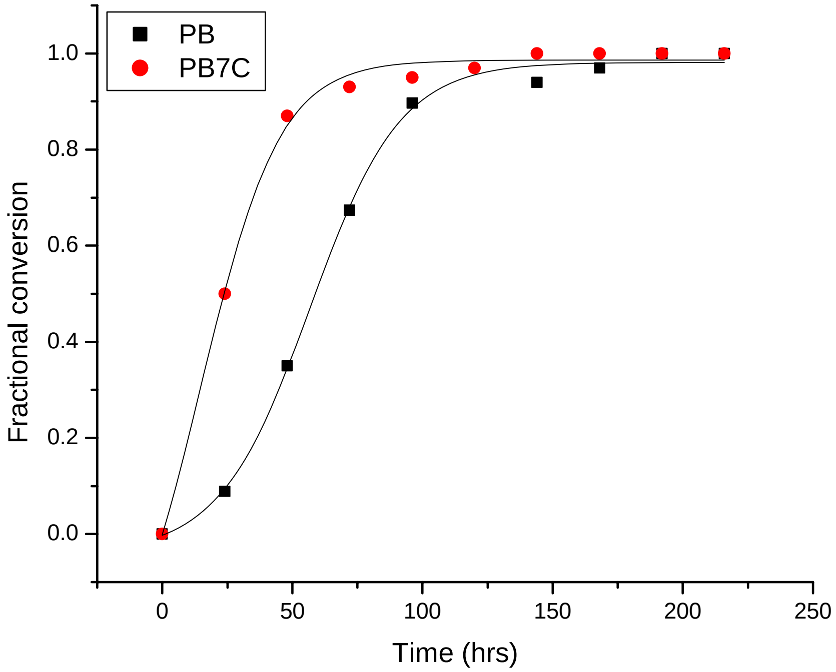

Figure 4.13: Fractional conversion of Form I for PB and PB7C nanocomposite

Figure 4.13 shows the fractional conversion of Form I for PB and PB7C at different time intervals from 24 to 216 hrs. The figure clearly indicates that the rate of phase transformation is higher in case of nanocomposites. For example, the conversion of form I for PB at 48 hrs is 35% while it significantly increased to 83% in presence of 7% MWCNT, suggesting significant enhancement in the rate of phase transformation in presence of MWCNT. The Avrami equation is used to study the phase transformation kinetics. The rate constant for phase transformation is found to be 2.89×10^{-4} (hrs^{-1}) for PB while it is 9.7×10^{-3} (hrs^{-1}) and 6.2×10^{-2} (hrs^{-1}) for PB5C and PB7C nanocomposites respectively, suggesting increased rate of phase transformation. The Avrami exponent for

PB is found to be about 1.9 while it reduces to 1.1 for PB3C, PB5C, and 0.8 for PB7C. This signifies that the process of nucleation and growth is different for PB/MWCNT nanocomposites. The half time for phase transformation (50% conversion to Form I) of PB is about 58 hrs and it significantly reduced to about 35 hrs for PB3C and PB5C and to 25 hrs for PB7C. The above results clearly indicate that the MWCNTs act as nucleating agent for PB, as it enhances the nucleation as well as the rate of phase transformation.

The observed increase in the transformation rate could be explained as follows. An increase in the rate of phase transformation with decrease in amorphous fraction was observed by Azzurri et al [17]. In the present case, higher crystallinity values for nanocomposites suggest lower amorphous content. Although, the amorphous content for PB5C and PB7C are almost comparable, their phase transformation rates vary significantly. This suggests that the lowering in amorphous fraction is not the only factor in enhancing the rate of phase transformation.

4.3.4.2 Phase transformation study by XRD:

The phase transformation of PB and PB7C nanocomposite is also studied using WAXD. As explained earlier, the two crystalline forms exhibit characteristic peaks for each form. For Form I, the X-ray diffraction peaks are observed at 2θ values of 10.0°, 17.6°, and 21.6° corresponding to planes (110), (300) and (211) respectively, whereas the peaks at 2θ values of 12°, 17°, 18.5° corresponding to planes (200), (220) and (213) respectively of Form II. The compression molded film samples are used for this purpose. The X-ray diffraction patterns are recorded at different predetermined time intervals. Figures 4.14 A and B illustrates the WAXD patterns of PB and PB7C recorded at various time intervals. A series of diffraction patterns are recorded in which the intensity of peak at 12° of Form II is monitored. Figure 4.15 shows the percent intensity ratio ($I_t/I_0 \times 100$), where, I_t is the intensity at time t and I_0 is the intensity at time zero.

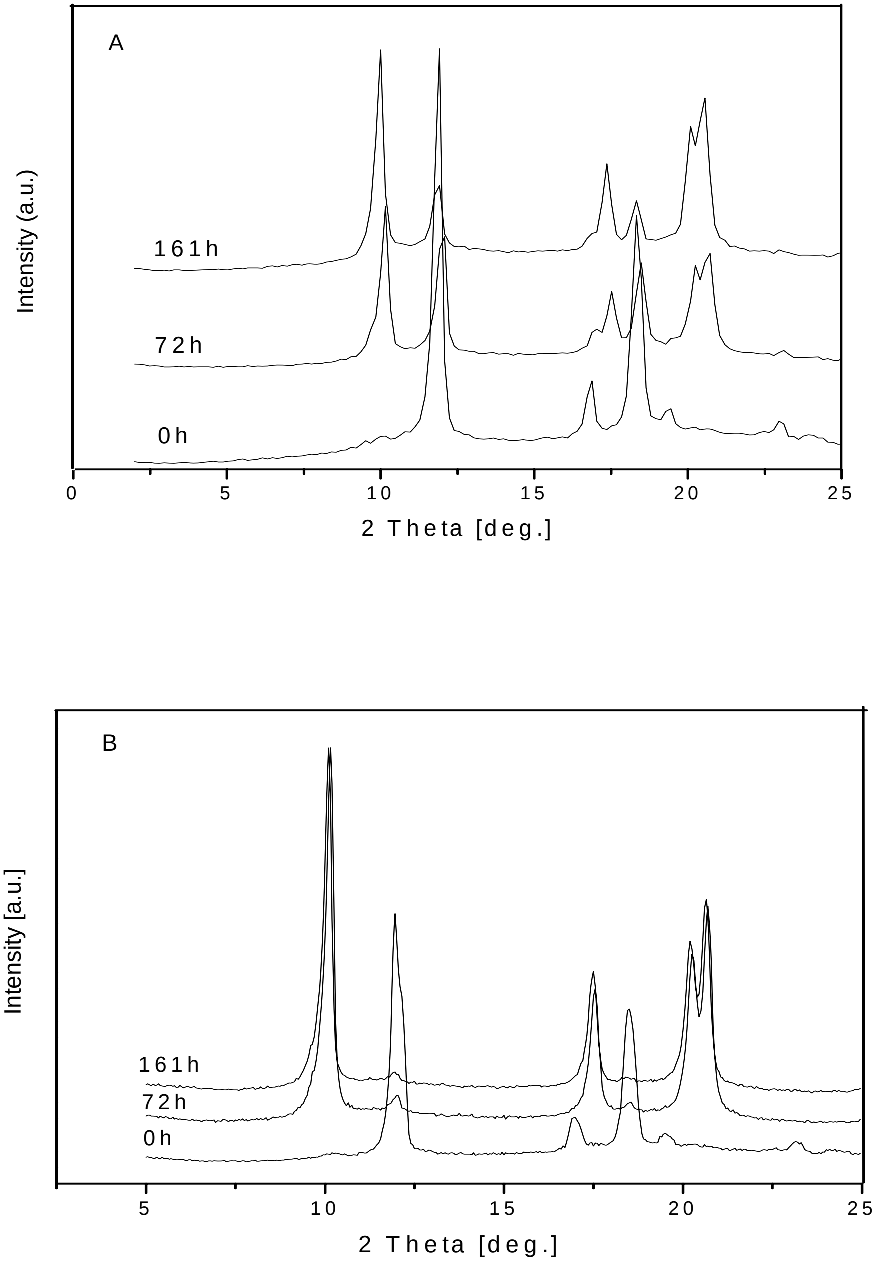

Figure 4.14: WAXD patterns for PB (A) and PB7C (B) at different time intervals

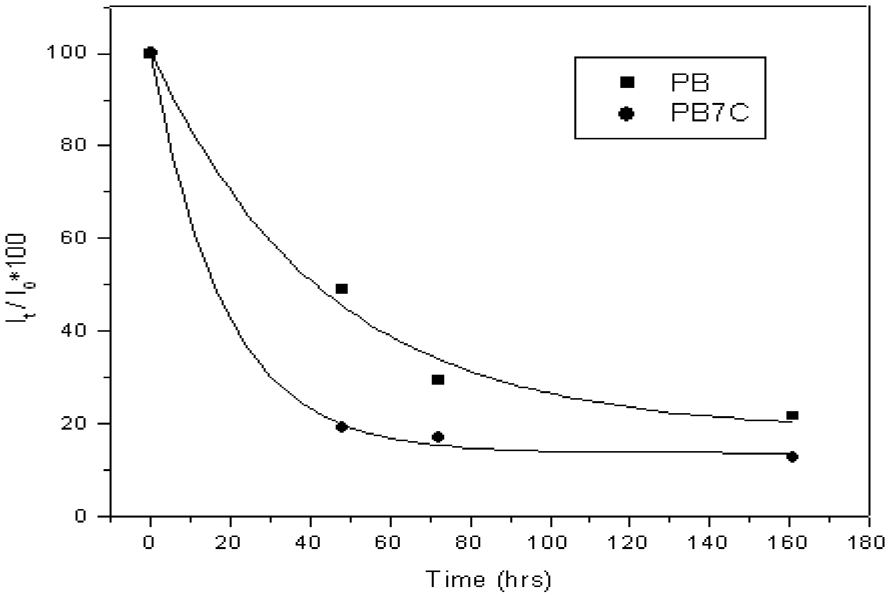

Figure 4.15: Change in peak intensity (percent) of peak at 12° of Form II at different time intervals

It is observed that as the aging time increases, the ratio of intensities decreases. The magnitude of decrement ratio for PB7C is found to be larger than that of pristine PB for all time intervals studied. These results suggest enhanced rate of phase transformation in case of nanocomposites.

4.3.5 Viscoelastic Properties:

4.3.5.1 Dynamic Mechanical Analysis (DMA):

Dynamic mechanical analysis is carried out from – 60 to 100 °C. Figure 4.16 illustrates the variation of storage modulus for PB and PB/MWCNT nanocomposites. In the glassy state, the polymer shows higher storage modulus and it decreases with respect to temperature. Similar behavior is observed for the nanocomposites with different loading of MWCNTs. The storage modulus below T_g maintains a plateau for PB as well as PB/MWCNT nanocomposites. However, above T_g, in the rubbery region, the storage modulus of the nanocomposites is significantly increased with increasing MWCNT content.

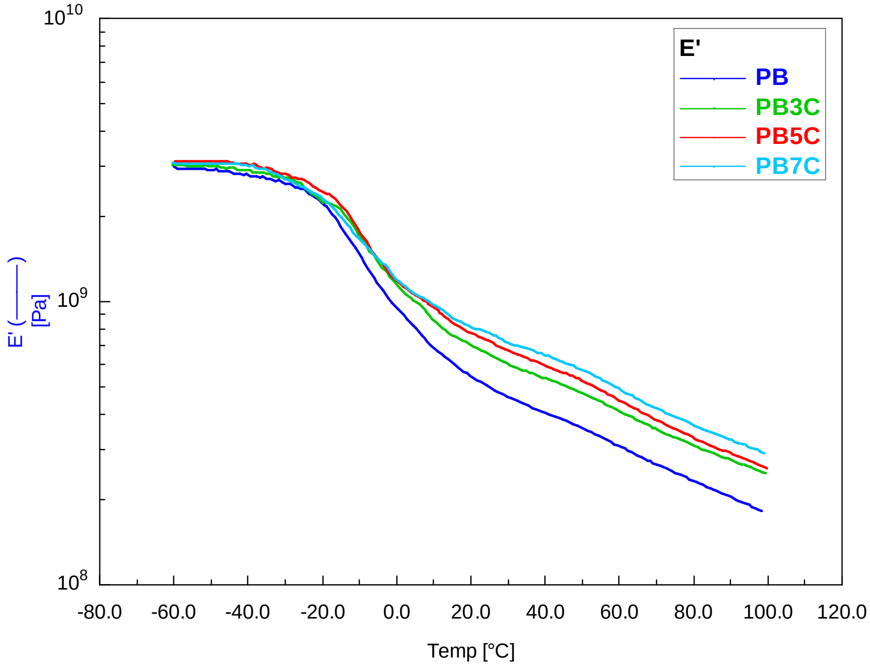

Figure 4.16: Storage modulus curves for PB and PB/MWCNT nanocomposites

For example at 40 °C, the E' for pristine PB is 0.4 GPa and is found to increased by 34%, 49% and 62% for 3, 5 and 7 wt% MWCNT loading respectively. This suggests that the incorporation of MWCNT results in the retention of high proportion of the stiffness in the rubbery regime. The retention of stiffness at temperature above the glass transition can be ascribed to the dispersion of high aspect ratio nanotubes in the polymer matrix.

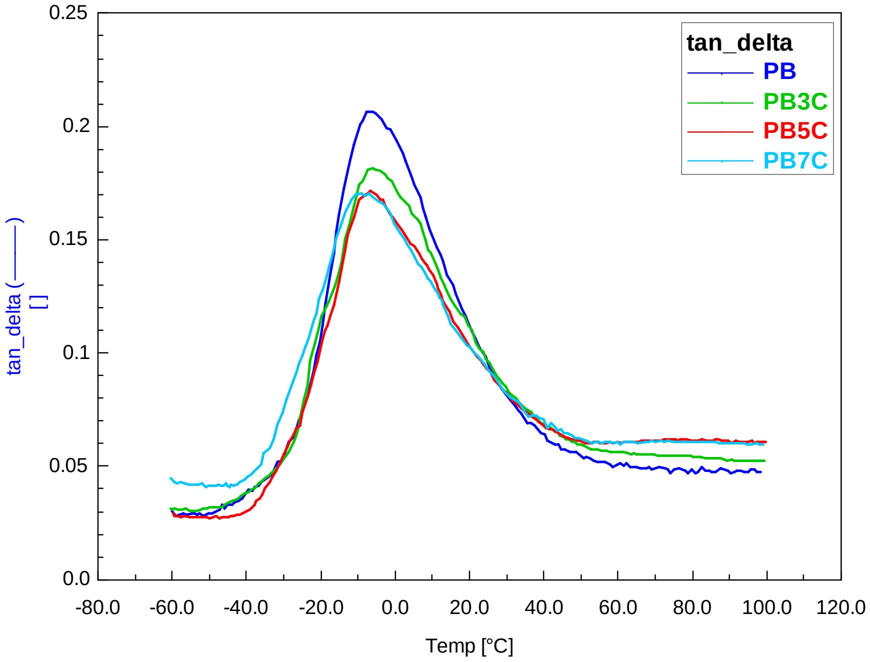

Figure 4.17: Tan δ curves for PB and PB/MWCNT nanocomposites

The glass transition temperature of the nanocomposites remains almost constant as that of pristine polymer. The tan δ value signifies dissipation of energy due to internal friction and molecular motion and is found to decrease for nanocomposites with increase in MWCNT content. The tan δ values reduced to 0.175, 0.162, and 0.158 for PB3C, PB5C, and PB7C, from 0.206 for PB. From the tan δ values (Figure 4.17), it is inferred that the viscoelastic energy dissipation is lowered because of dispersion of MWCNTs in the polymer matrix. The lowering of tan δ values for the nanocomposites can be ascribed to the confinement of PB chains by MWCNT and this confined fraction increases as the content of MWCNT increases. Similar behavior is reported for PC/MWCNT nanocomposites [18].

4.3.5.2 Melt rheology:

The rheological study of the polymer nanocomposites is very complex and interesting as the incorporation of fillers greatly alters the microstructure and the flow behavior of polymer matrix [19]. The complex viscosities of the nanocomposites and pristine PB are shown in Figure 4.18.

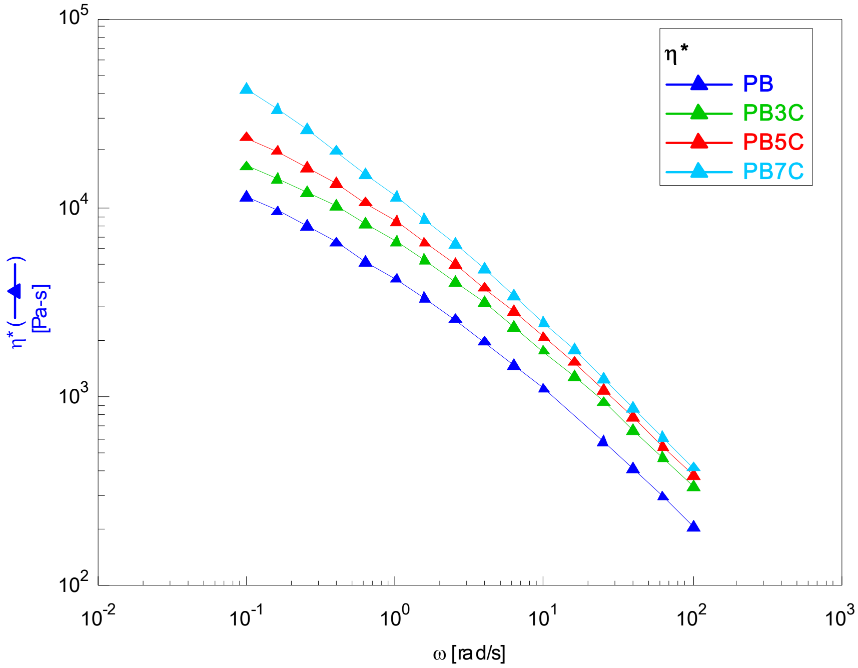

Figure 4.18: Complex viscosity curves for PB and PB/MWCNT nanocomposites

The low frequency behavior is sensitive to the structure of composites and thus can be used to derive information about the percolation state of the fillers in polymer matrix. As can be seen from the figure, the complex viscosity of the nanocomposites increased with the MWCNT content and the effect is more pronounced at the lower frequencies. The viscosity of neat PB is 11385 Pa-S at 0.1 rad/sec and increases to about 42204 Pa-S for 7% MWCNT content. The remarkable increase in the viscosity of the PB/MWCNT nanocomposites between 5 to 7% is due to the formation of interconnected structures (percolated network) of the nanotubes called as rheological percolation threshold which is similar to that reported for PE/MWCNT nanocomposites [20].

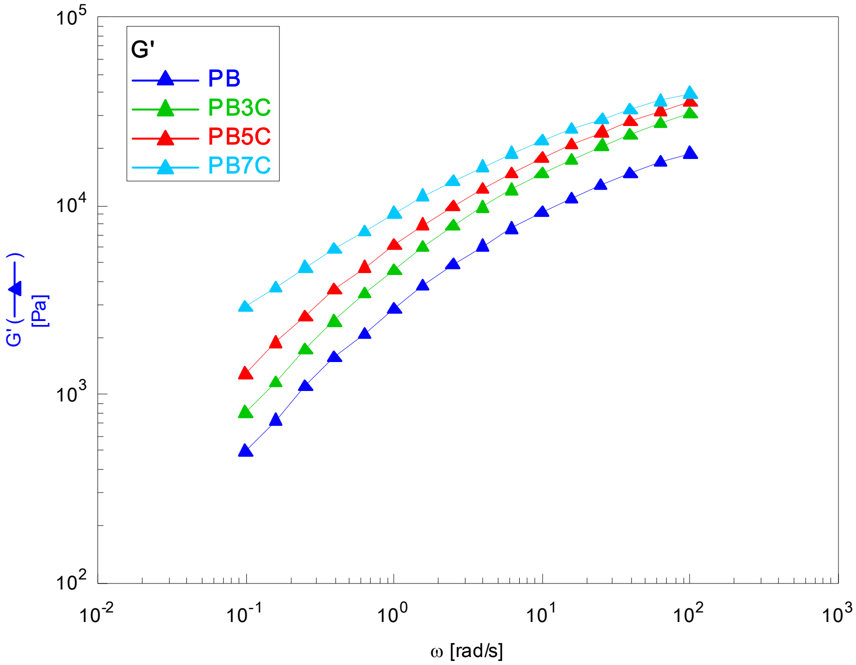

Figure 4.19: G' for PB and PB/MWCNT nanocomposites

The increase in the complex viscosity is concomitant with an increase in the storage modulus. The storage modulus for the composites is presented as a function of MWCNT content in Figure 4.19.

The storage modulus increased from about 500 Pa to about 800 Pa for 3 % MWCNT and then up to about 3000 Pa for 7% MWCNT.

The Cole – Cole plots (imaginary part of the viscosity is plotted against the real part) are generally used to observe the compatibility and the relaxation behavior of the two constituents of the blend/composite. The smooth semi circular arcs imply the compatibility of the components [21].

Figure 4.20 shows the Cole – Cole plots for PB and PB/MWCNT nanocomposites.

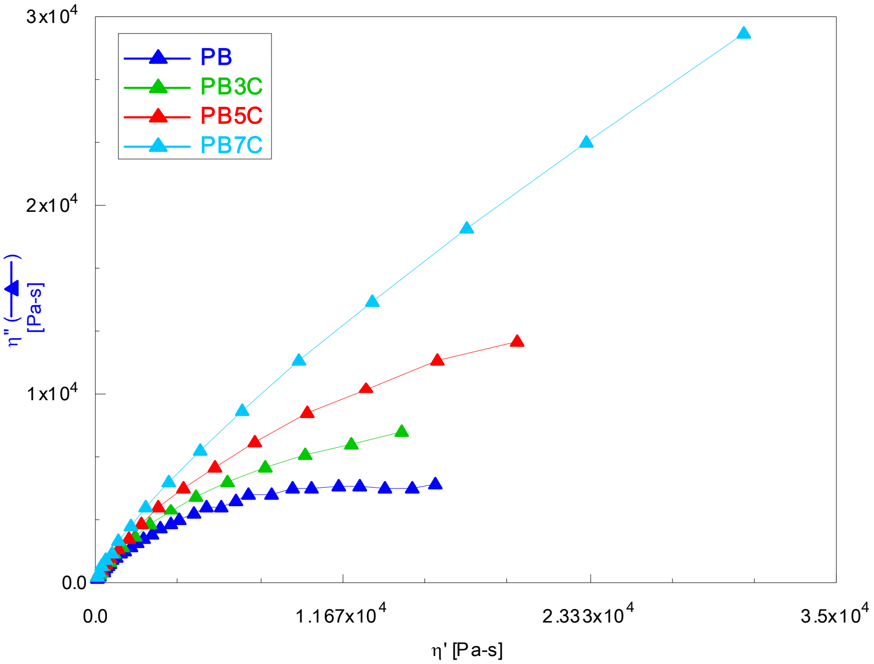

Figure 4.20: Cole-Cole plots for PB and PB/MWCNT nanocomposites

From figure 4.20 it is revealed that the nanocomposites show different nature of the plots compare to pristine PB which suggest the incompatibility of MWCNT and the polymer matrix and it increases with the content of MWCNT.

The dynamic storage modulus (G'), the loss modulus (G") and the complex viscosity (η*) for PB at 200 °C are shown in Figure 4.21. In the lower frequency region, PB melt shows liquid (viscous) like behavior (G'<G"), while the solid (Elastic) like behavior in the

higher frequency region (G'>G"). The frequency at which the crossover between G' and G" occurs is considered as the transition from liquid to solid like behavior of the matrix [22].

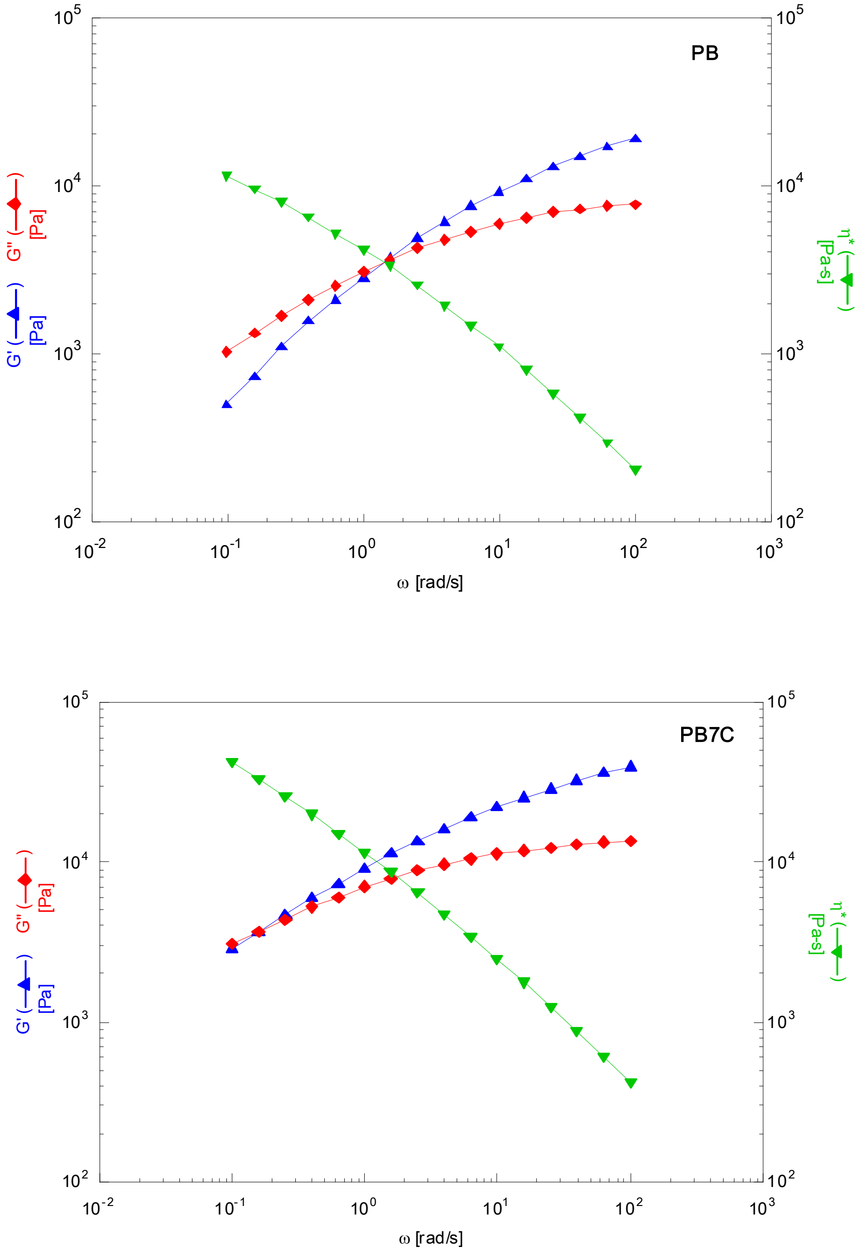

Figure 4.21: G', G", and η* curves for PB and PB/MWCNT nanocomposites

A shift in the crossover frequency of the nanocomposites towards the lower frequency side with increasing MWCNTs content is clearly discernible from the Figure 4.21. The crossover frequencies at three temperatures for PB and PB nanocomposites are presented in table 4.4.

Table 4.4: Crossover frequencies for PB and PB/MWCNT nanocomposites

Temp (°C)	Crossover frequency (rad/s)			
	PB	PB3C	PB5C	PB7C
175	0.61	0.48	0.3	--
200	1.39	1.14	0.66	0.15
225	2.81	1.81	1.0	0.21

At 200°C, the crossover occurres at a frequency of 1.39 rad/s for pristine PB, while for PB3C nanocomposite this frequency shifts to the lower side i.e. at 1.1 rad/s. As the content of the MWCNT is increased, the crossover frequency shifts to further lower side i.e. 0.66 and 0.15 rad/s for 5 and 7 wt% MWCNT respectively. Similar behavior is observed even at 225 °C. The shifting of crossover frequency towards the left (lower) side also signifies the delayed relaxation for the molecular chains. As can be seen from Table 4.4 that the crossover frequencies of pristine PB and the nanocomposites are also temperature dependent. To compare the relaxation behavior, the terminal slopes of G’ are determined [23]. The slope at 200 °C for PB is found to be about 0.76 while it decreased to 0.75, 0.67 and 0.50 for PB3C, PB5C and PB7C nanocomposites respectively. As the temperature increases to 225 °C the slopes also increases because of enhanced motions of molecular chains at high thermal energy. For example, at 225 °C, the slopes decreased from 0.86 (for PB) to 0.76, 0.62, and 0.51 for PB3C, PB5C, and PB7C respectively.

In case of nanocomposites, the magnitude of increase in slopes is lower as compared to pristine PB, suggesting increase in relaxation time. The magnitude of increase in slope is also reduced with the content of MWCNT. This clearly indicates that the nanotube network hinders the relaxation of polymer chains.

The lowering of the magnitude of the terminal slopes for the nanocomposites indicate that the relaxation of the nanocomposites is slower than that of pristine PB, this is confirmed by the stress relaxation data, obtained from the rheological analysis [23].

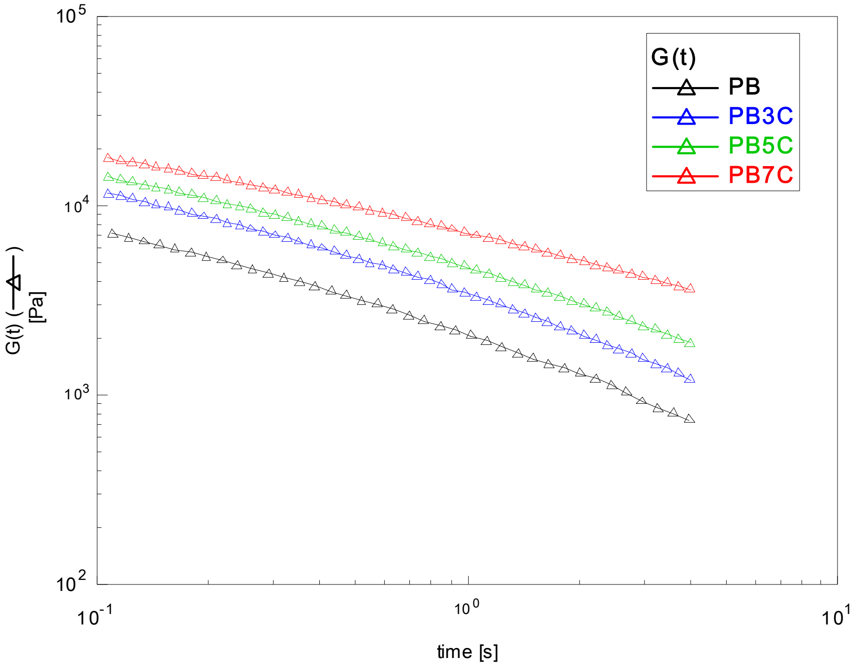

Figure 4.22: Stress relaxation modulus curves for PB and PB/MWCNT nanocomposites

Figure 4.22 shows the relaxation modulus G(t) for PB and the nanocomposites, it can be readily understood that the slope of the curves for the nanocomposites reduced with respect to the MWCNT content. The slopes are found to decrease from 0.63 for PB to 0.62, 0.55, and 0.44 for PB3C, PB5C, and PB7C nanocomposites respectively. The decrease in the slope implies an increase in relaxation time with increase in MWCNT content. Above results suggest that the delayed relaxations of the molecular chains in presence of MWCNTs are due to the formation of nanotube network, which acts as physical barrier for the complete relaxation. This network gives the stability to the composite framework and impedes the long-range motion of the polymer chains [24].

The tan δ values at 200 °C are shown against the frequencies studied in Figure 4.23.

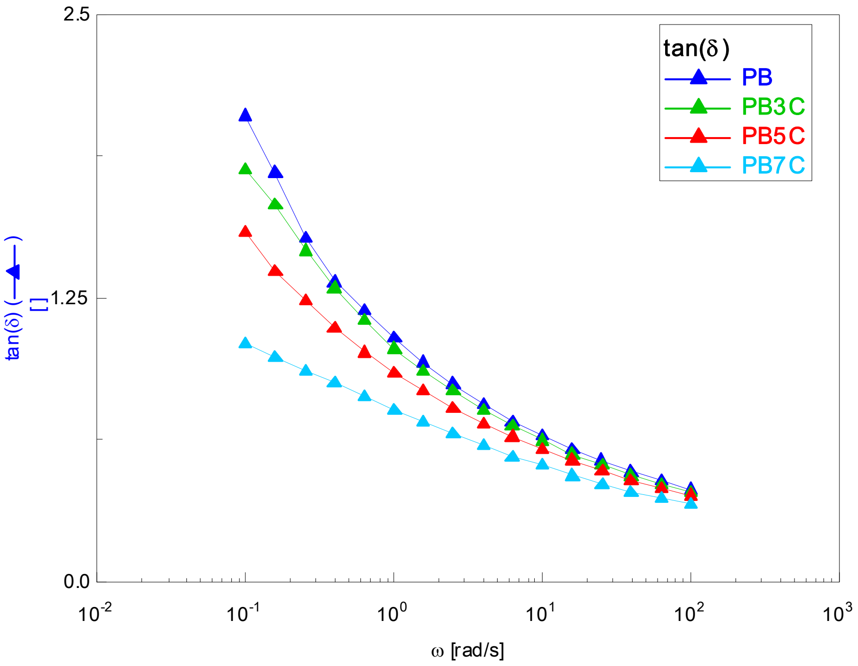

Figure 4.23: Tan δ curves for PB and PB/MWCNT nanocomposites

It can be seen from the figure that, at lower frequencies the decrease in tan δ much more than at higher frequencies. As the content of MWCNT increased the curves becomes flatter. Similar behavior is reported by McNally et al [20]. The observed reduction in tan δ values was attributed to the presence of interfacial interactions between the polymer matrix and MWCNT and to the increased hindrance for energy dissipation and relaxation of the polymer chains in presence of MWCNT.

4.3.6 Dielectric Spectroscopy:

The polymer matrix reinforced by the conductive phase is interesting to study as it greatly alters the dielectric properties of the matrix. The dielectric response of the composite is strongly dependent on the volume fraction, the size and the shape of the reinforced conductive phase as well as the interaction between the two phases [25]. PB is an insulator while MWCNT is conducting material. Consequently, the conductivity of PB/MWCNT nanocomposites varies as the MWCNT content increases. However, the change in the conductivity is not of linear characteristics but exhibits percolation threshold and a drastic increase in the conductivity for the compositions at which the volume fraction of MWCNT becomes just sufficient to provide continuous electrical path through PB matrix. At the low frequency the applied AC field provides sufficient time to charge carriers to drift over large distances. Increasing frequency results in a deduction of the mean displacement of charge carriers and after a critical frequency, the real part conductivity follows a power law. At low frequencies, the conductivity plateau is observed which is characteristic of non-dielectric with direct current (dc) conductivity σ_c and is often describe as universal dynamic response for most of the materials.

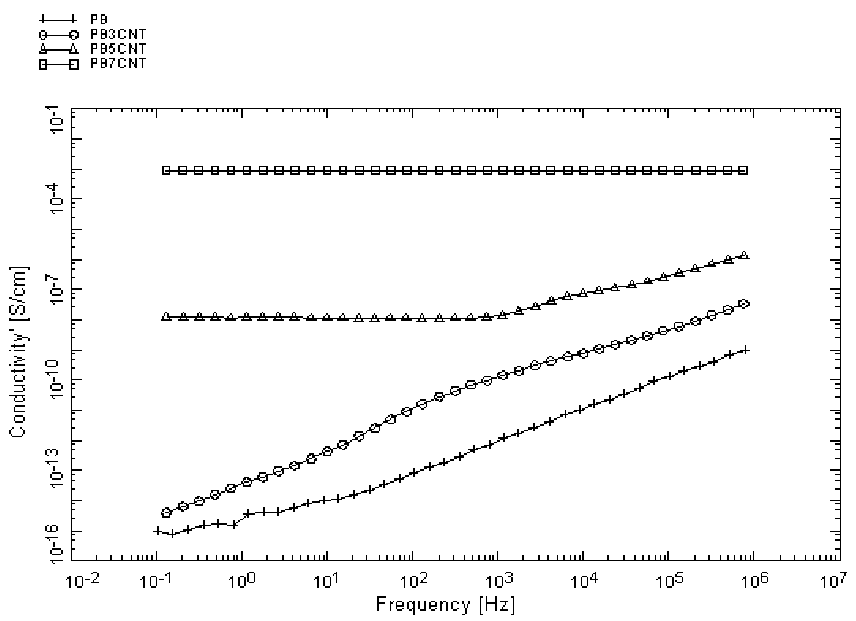

Figure 4.24: Electrical conductivity for PB and PB/MWCNT nanocomposites

Figure 4.24 shows the electrical conductivity of the PB/MWCNT nanocomposites with various content of the MWCNT. As can be seen from the figure that the electrical conductivity increase with an increase in the content of MWCNT. The conductivity of the pristine PB is dependent on the frequency and is found to be about 1×10^{-15} S/cm at 0.1 Hz. While it increased to 9×10^{-14}, 1×10^{-08} and 1×10^{-03} S/cm for 3, 5 and 7 wt% MWCNT respectively. The figure clearly shows that for 7 wt% MWCNT nanocomposite the conductivity is independent of the frequencies studied while below 7 wt% nanocomposites it is dependent at the higher frequencies.

The variation of relative permittivity (ε') of the nanocomposites with different weight fractions of MWCNT is shown in Figure 4.22.

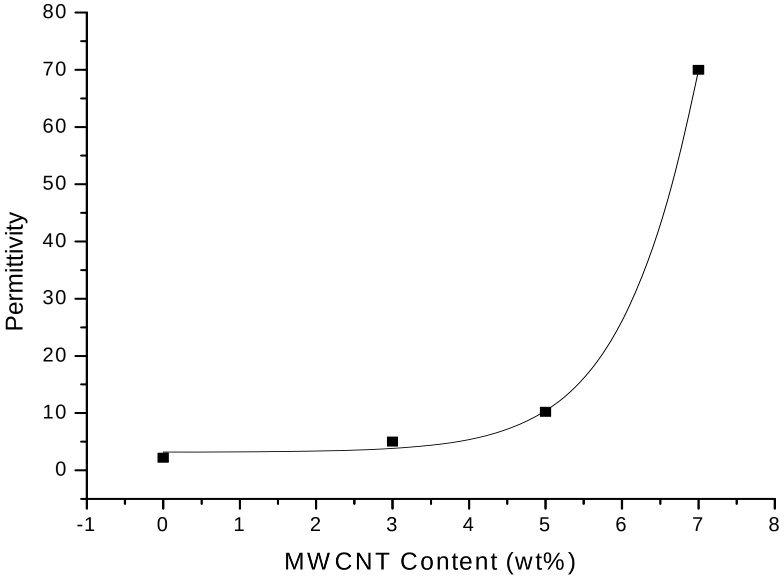

Figure 4.25: Relative permittivity for PB and PB/MWCNT nanocomposites

The relative permittivity (ε') values are measured at a frequency of 1 MHz. As can be seen from the figure, the value of relative permittivity (ε') increases moderately up to 5 wt% of MWCNT and exhibits a sudden increase at 7 wt%. The relative permittivity (ε') value for pristine PB is 2.3 while it increased to 70 for PB7C. It is well known that significant changes in the dielectric constant and conductivity are observed at the critical volume fraction at which the percolation network is formed. The remarkable increase in the conductivity for 7 wt% MWCNT confirms the efficient dispersion and interconnectivity of MWCNT in PB matrix, which leads to electrical percolation threshold.

4.3.7 Thermogravimetric analysis (TGA):

The thermal stability of the PB and the nanocomposites is studied using Perkin Elmer TGA7 in an inert atmosphere. Figure 4.26 shows the TGA thermograms for PB and PB/MWCNT nanocomposites.

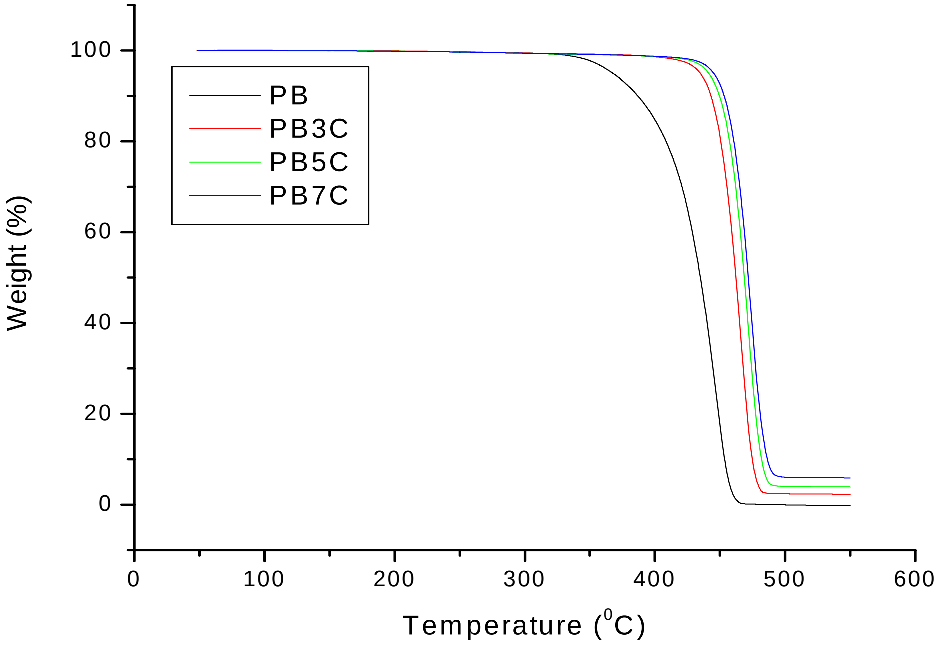

Figure 4.26: TGA thermogram in nitrogen atmosphere for PB and PB/MWCNT nanocomposites

The degradation of pure PB started at 350 °C and the complete degradation occurred at 475 °C. From the figure it can be clearly seen that the temperature at the onset of degradation initiation (TDI) is increased for the nanocomposites compared to pristine PB. The TDI is found to be increased by about 65 °C, 85 °C and 90 °C for PB3C, PB5C, and PB7C nanocomposites respectively. To our knowledge, this is the highest degree of increase in temperature of degradation initiation for the PB composites. The constant weights of the composites were found at 483 °C for 3% MWCNT content and increased with respect to the loading suggesting the PB matrix degraded completely and the residue left was of only nanotubes. This might be due to the higher thermal stability of the nanotubes. The 50% weight loss for PB was found at 450 °C while in case of 7% composite it increased by 24°C. The presence of MWCNTs significantly enhances the thermal stability of the composites. There are two reasons given in the literature [26] for the improvement in the thermal stability of the composites, the first one is that the barrier effect due to well dispersion of nanotubes which hinders the formed degradation products and the other one is that due to the strong physical adsorption of matrix molecules on the surface of nanotubes and these adsorbed molecules are much less active than those far from nanotube surface and thus their volatilization is delayed.

Dondero et al [27] have reported about 80 °C increase in thermal stability for PP/MWCNT nanocomposites with just 3% MWCNT content, prepared by melt compounding while in HDPE/SWNT nanocomposites the thermal stability was found to be increased by about 70 °C in nitrogen atmosphere and by 115 °C in air [14].

4.4 Conclusions:

The significant observations of the present investigation can be summarized as follows. The non-isothermal crystallization studies revealed the higher values for Z_t and lower values for F(T) compared to pristine PB suggest enhanced crystallization rate in presence of MWCNT. The energy of activation in case of non-isothermal crystallization is found to be slightly higher than that of pristine PB. The nucleation activity of MWCNT obtained from non-isothermal crystallization is found to be 0.48 for PB7C nanocomposite confirm highly active surface for nucleation. In isothermal crystallization studies, the crystallization half time is found significantly lower and the crystallization temperatures are increased by 15 °C, while the nucleation constant (K_g) deduced from Lauritzen – Hoffmann equation is found lower as compared to PB. All these observations corroborate the active nucleation of PB due to incorporation of MWCNT. The energy of activation in case of isothermal crystallization is found to be lower for PB3C and PB5C while marginal increase is observed for PB7C nanocomposite. The optical micrographs exhibit significantly smaller crystallites of disordered morphology for the nanocomposites as compared to well defined spherulitic morphology for pristine PB. Avrami analysis of phase transformation revealed higher rate for PB/MWCNT nanocomposites while the Avrami exponent is found to be lower for PB/MWCNT nanocomposites compared to pristine PB. These results suggest that the mechanism for nucleation and growth of Form I is altered in presence of MWCNT. The observed increase in the rate of phase transformation for the nanocomposites is attributed to the decrease in amorphous content and enhanced nucleation of Form I. The dynamic mechanical analysis shows significant improvement in storage modulus in the rubbery regime as compared to the glassy regime. The glass transition temperature remained the same while a decrease in tan δ values are observed. In the melt state, an increase in viscosity is found with respect to increasing content of MWCNT. Tan δ in the melt state shows frequency dependence and becomes flatter at the lower frequencies with the increasing content of MWCNT. The crossover frequency of the nanocomposites shifts towards the lower frequency region with increasing MWCNT content, signifying the elastic behavior and the delayed relaxation of the nanocomposites because of incorporation of MWCNT. This result is ascribed to the formation of a percolated network that resisted the flow of the matrix. The electrical conductivity and the permittivity are considerably enhanced at 7 wt% MWCNT. From the results, it can be concluded that the rheological and electrical conductivity percolation threshold coincides between 5 and 7 wt% MWCNTs. The thermal stability is found to significantly improve for the nanocomposites than that of pristine PB due to the strong adsorption of chain segments on the surface of nanotubes.

References:

[1] Vasilios G, Vasilios T, Dimitrios G, Dimitrios P. Chemistry of Materials, 17(7), 1613 (**2005)**

[2] Mitchell D, Lee S, Trofin L, Li N, Nevanen T, Soderlund H, Martin C. Journal of American Chemical Society, 124,11864 (**2002)**

[3] Sreekumar, T.; Liu, T.; Min, B.; Guo, H.; Kumar, S.; Hauge, R.; Smalley, R. Advanced Materials, 16(1), 58 (**2004)**

[4] Sandler J, Shaffer M, Prasse T, Bauhofer Q, Schulte K, Windle A. Polymer, 40, 5967 (**1999)**

[5] Clayton L, Sikder A, Kumar A, Cinke M, Meyyappan M, Girasimov T, Harmon J. Advanced functional materials, 15, 101 **(2005)**

[6] Karmakar S, Tyagi P, Misra D, Sharma S, Physical Review B73, 184119 **(2006)**

[7] Kim T, Park I, Ryoo R. Angew Chem Int Ed 42, 4375, **(2003)**

[8] Lozano K, Bonilla-Rios J, Barrera E. Journal of Applied Polymer

Science, 80, 1162 **(2001)**

[9] Tang W, Santare M, Advani S. Carbon, 41, 2779 **(2003)**

[10] Song YS, Youn JR. Carbon, 43, 1378 **(2005)**

[11] Potschke P, Fornes T, Paul DR. Polymer, 43, 3247 **(2002)**

[12] Kim J, Park H, Kim S. Polymer, 1379, **(2006)**

[13] Wiemann K, Kaminsky W, Gojny F, Schulte K. Macromolecular chemistry and physics 206, 1472 **(2005)**

[14] Kodjie S, Li L, Li B, Cai W, Li C, Keating M. Journal of Macromolecular Science Part B Physics, 45, 231 **(2006)**

[15] Kaszonyiova M, Rybnikar F, Geil PH. J Macro Sci Phys; B43, 1095 **(2004)**

[16] Tosaka M, Kamijo T, Tsuji M, Kohjiya S, Ogawa T, Isoda S, Kobayashi T. Macromolecules, 33, 9666 **(2000)**

[17] Azzurri F, Flores A, Alfonso G, Calleja B. Macromolecules, 35, 9069 **(2002)**

[18] Sung Y, Kum C, Lee H, Byon N, Yoon H, Kim W. Polymer, 46, 5656 (**2005)**

[19] Abdel-Goad M, Pötschke P. Journal of Non-Newtonian Fluid Mechanics, 128, 2 **(2005)**

[20] McNally T, Pötschke P, Halley P, Murphy M, Martin D, Bell S, Brennan, G, Bein D, Lemoine P, Quinn J. Polymer, 46, 8222 (**2005**)

[21] Hameed T, Hussein I. Macromol Mater Eng, 289, 198 **(2004)**

[22] Hyun Y, Lim S, Choi H, Jhon M. Macromolecules, 34, 8084 (**2001)**

[23] Gu, S.; Ren, J.; Wang, Q. Journal of Applied Polymer Science, 91, 2427 (**2004)**

[24] Zhang Q, Rastogi S, Chen D, Lippits D, Lemstra P. Carbon, 44, 778 (**2005)**

[25] Zhu B, Xie S, Xu Z, Xu Y. Compos Sci Technol, 66, 548 (**2006)**

[26] Yang J, Lin Y, Wang J, Lai M, Li J, Liu J, Tong X, Cheng H. Journal of Applied polymer science, 98, 1087 **(2005)**

[27] Dondero W, Gorga R. Journal of polymer Science Polymer Physics, 44, 864 **(2006)**

Chapter 5

PB/Barium titanate ($BaTiO_3$) Nanocomposites

5.1 Introduction:

In this chapter we present the results of effect of nanoparticles on the crystallization, phase transformation, and dynamic mechanical properties of poly(1-butene). Barium titanate ($BaTiO_3$) nanoparticles (size 30-50 nm) are used for this purpose. Generally, the incorporation of nanoparticles is reported to results in enhanced crystallization rate [1], change in spherulitic morphology [2], increase in thermal stability [3] and improved mechanical properties [4]. In the previous chapters, we have studied the effect of nanoclay, and MWCNTs on the crystallization, phase transformation and thermo-mechanical properties of PB. It is therefore interesting to find out the effect nanoparticles on the crystallization, phase transformation, and mechanical behavior of PB.

5.2 Barium titanate nanopowder:

The $BaTiO_3$ nanoparticles with 99% purity are procured from Aldrich. The average particle size of the nanoparticles is 30-50 nm. The density of the nanoparticles is 6.08 g/cc at 25 °C. The crystalline phase of the nanoparticles is cubic (as per company data sheet).

5.2.1 X - ray diffraction (XRD):

The X - ray diffraction pattern for $BaTiO_3$ nanoparticles is shown in Figure 5.1. All the diffraction peaks can be indexed to cubic structure of $BaTiO_3$ and are in good agreement with the values reported. The sharp XRD patterns indicate presence of highly crystalline nanoparticles. It is also confirmed from the X - ray diffraction patterns that no impurity is present in the sample [5].

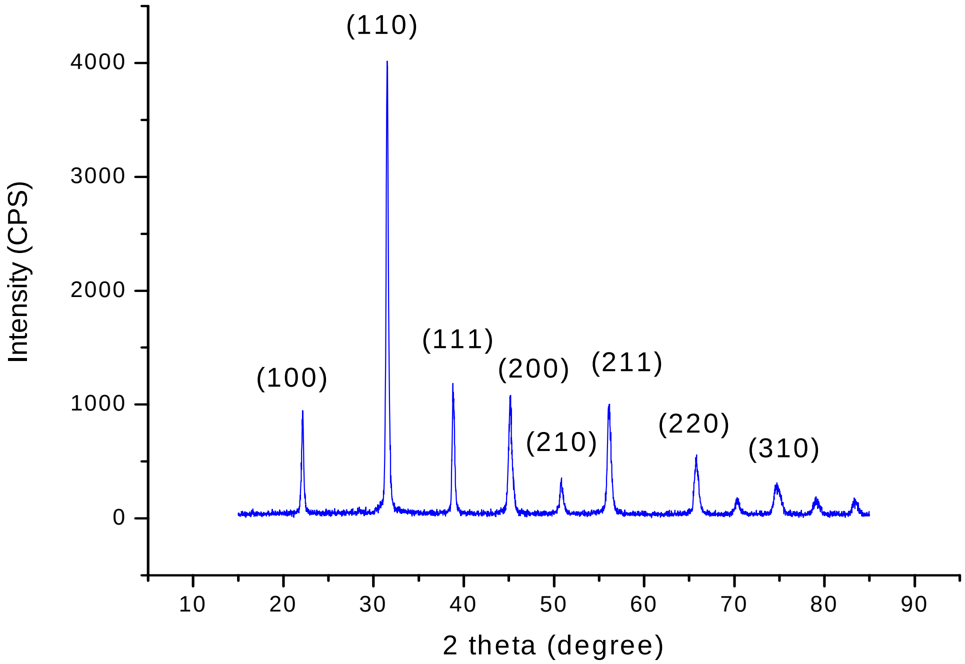

Figure 5.1: X - ray diffraction pattern for BaTiO$_3$ nanoparticles

5.2.2 Morphology:

The morphology of the BaTiO$_3$ nanoparticles is studied using SEM and TEM, the micrographs are shown in Figures 5.2 and 5.3 respectively. Even though, the particle size as per company data sheet is 30-50 nm, the nanoparticles normally form aggregates. The clumps of BaTiO$_3$ nanoparticles of various sizes are observed in both the micrographs. The inset of Figure 5.3 clearly shows the non-spherical shape of the nanoparticles.

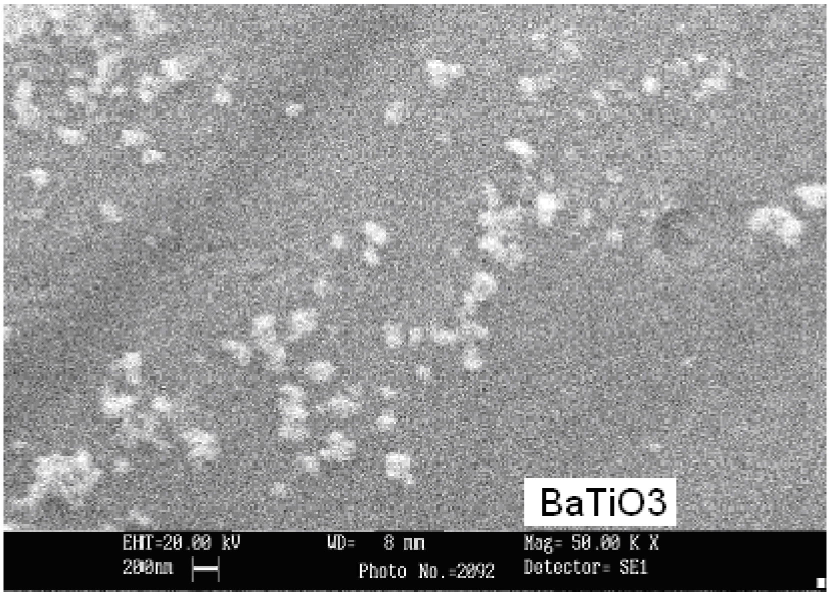

Figure 5.2: Scanning electron micrograph for $BaTiO_3$ nanoparticles

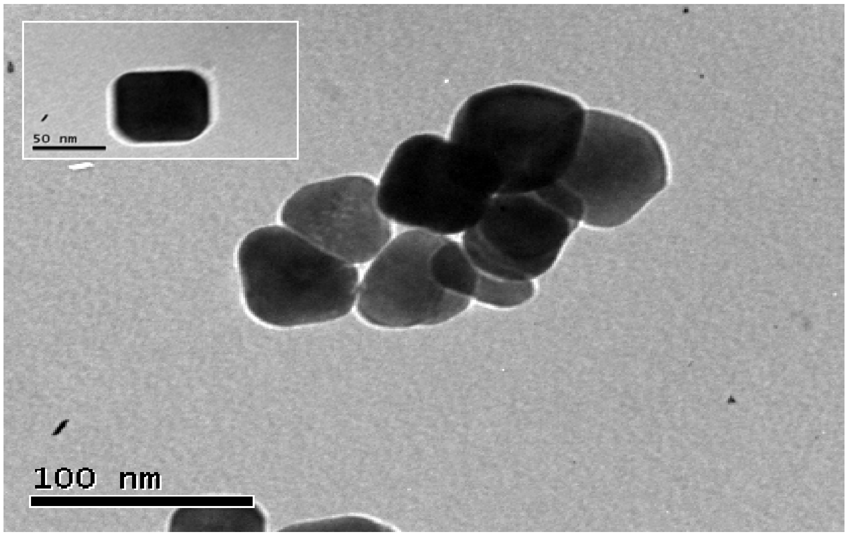

Figure 5.3: TEM micrograph for $BaTiO_3$ nanoparticles

5.2.3 Thermogravimetric analysis (TGA):

The thermal stability of Barium nanoparticles is studied using thermogravimetric analysis. The TGA thermogram shows no weight loss in the temperature range studied (50-700 °C)

5.3 Results and discussion:

5.3.1 Morphology:

5.3.1.1 Scanning Electron Microscopy (SEM):

The nanoparticles generally form agglomerates that can not be dispersed uniformly by mere shearing due to the strong interactions between them.

Figure 5.4 A, B and C presents the SEM micrographs of PB/$BaTiO_3$ nanocomposites. It can be seen from the micrographs that nanoparticles are well dispersed in the polymer matrix. In addition, agglomerates having particle size of 1-2 μm are observed. When the content of $BaTiO_3$ nanoparticles is increased, a uniform dispersion is seen along with an increase in the number of agglomerates. The size of the agglomerates in the case of PB7B and PB10B is found to be larger (about 1- 4 μm) compared to PB5B nanocomposite.

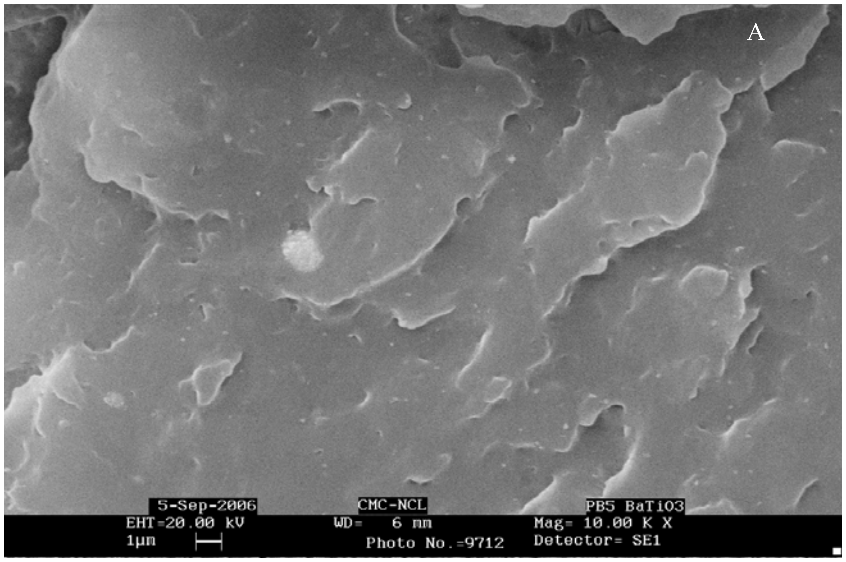

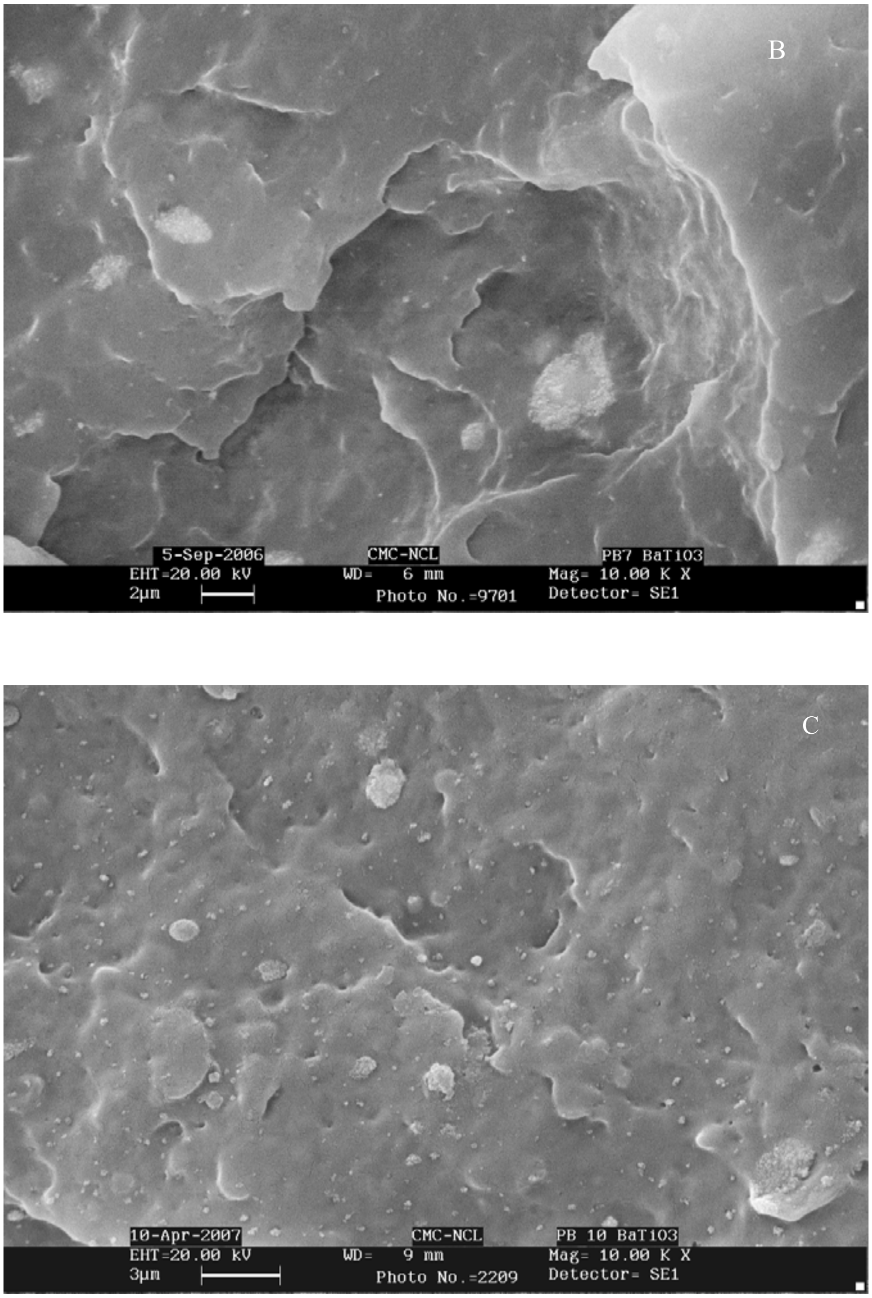

Figure 5.4: SEM micrographs for PB5B (A), PB7B (B) and PB10B (C)

5.3.2 Crystallization Studies:

5.3.2.1 Non-isothermal Crystallization:

It is interesting to study the effect of nanoparticle (three dimensions in nanoscale) on the crystallization behavior of PB. The melting and crystallization parameters are obtained from the DSC scans and presented in Table 5.1. The melting temperature is found to be same as that of pristine PB, while the crystallization temperature is increased by 4-5 °C for all the nanocomposites. This suggests that the nanoparticles serve as nucleating agents. The heat of fusion is increased marginally with the content of $BaTiO_3$ nanoparticles.

Table 5.1: Melting and crystallization parameters for PB and PB/$BaTiO_3$ nanocomposites

Sample	T_m (°C)	T_c (°C)	ΔH_f (J/g)
PB	128.9	69.8	68.9
PB5B	128.5	74.5	69.2
PB7B	128.9	75.0	69.6
PB10B	129.1	74.2	70.7

5.3.2.1.1 Non-isothermal Crystallization Kinetics:

Effect of $BaTiO_3$ nanoparticles on the crystallization of PB at different cooling rates is studied. The crystallization temperature decreased as the cooling rate is increased for PB. Similar behavior is observed for nanocomposites. The nanocomposites with $BaTiO_3$ show higher values of crystallization temperature than pristine PB, suggesting enhanced nucleation of PB in presence of nanoparticles. The non-isothermal crystallization kinetics is studied using modified Avrami theory (as discussed in section 2.5.3.1) to determine n, $t_{1/2}$ and Z_t for the nanocomposite. Table 5.2 presents the n, $t_{1/2}$ and Z_t values for PB and the nanocomposites. It can be seen from the table that the value of Z_t increases with an increase in cooling rate for PB as well as for nanocomposites. The values for Z_t depend on the content of nanoparticles. The higher values of Z_t and lower values of $t_{1/2}$ for nanocomposites compared to that of pristine PB, suggests that the nanoparticles act as nucleating agent.

Table 5.2: Non-isothermal crystallization parameters for PB and PB/$BaTiO_3$ nanocomposites (modified Avrami analysis)

Sample	ϕ (K/min)	$t_{1/2}$ (min)	T_c (°C)	n	Z_t (min^{-1})	Z_c
PB	2.5	1.5	79.4	4.2	4.99×10^{-3}	0.12
	5	1.1	74.3	4.5	5.28×10^{-2}	0.56
	10	1.0	69.8	4.6	0.54	0.94
	20	0.9	62.9	4.2	3.48	1.06
PB5B	2.5	1.4	83.0	4.3	9.96×10^{-3}	0.16
	5	1.1	79.1	4.6	4.29×10^{-2}	0.53
	10	0.9	74.5	4.9	0.57	0.95
	20	0.9	67.4	4.2	5.98	1.09
PB7B	2.5	1.4	83.5	4.2	1.02×10^{-2}	0.16
	5	1.0	79.4	4.5	9.39×10^{-2}	0.62
	10	0.9	75.0	4.1	1.30	1.02
	20	0.9	67.8	3.9	8.10	1.11
PB10B	2.5	1.4	86.3	4.2	1.73×10^{-2}	0.20
	5	1.0	80.8	4.0	0.19	0.71
	10	0.9	74.2	4.5	0.82	0.98
	20	0.9	67.9	3.9	6.95	1.10

The non-isothermal crystallization is analyzed using combined Avrami-Ozawa equation, which is discussed in part 2.5.1.1. Table 5.3 shows the values of F(T) and ‘a’ calculated from the plots of log ϕ vs. log t as shown in Figure 5.5

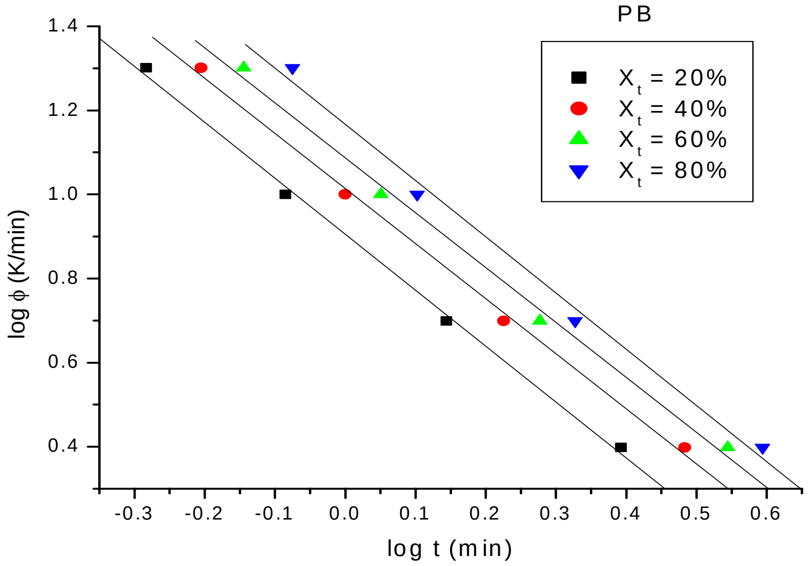

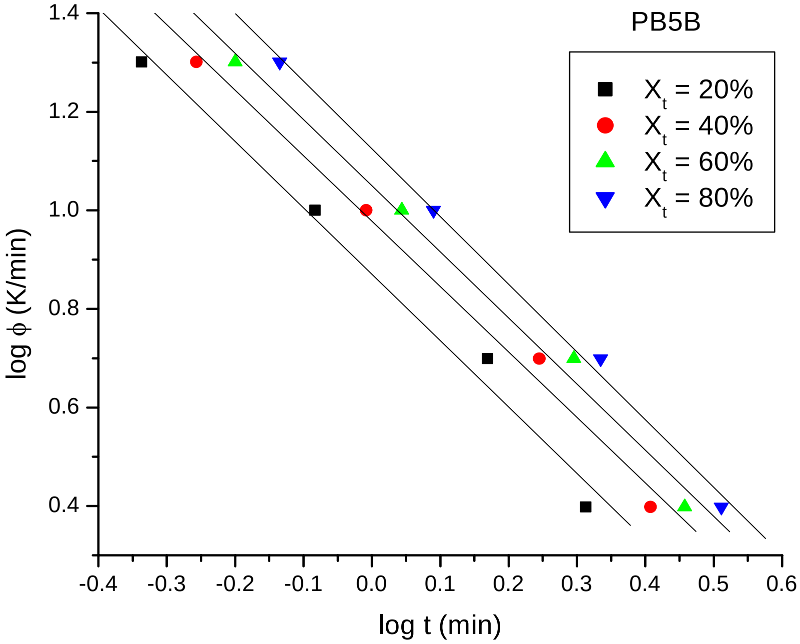

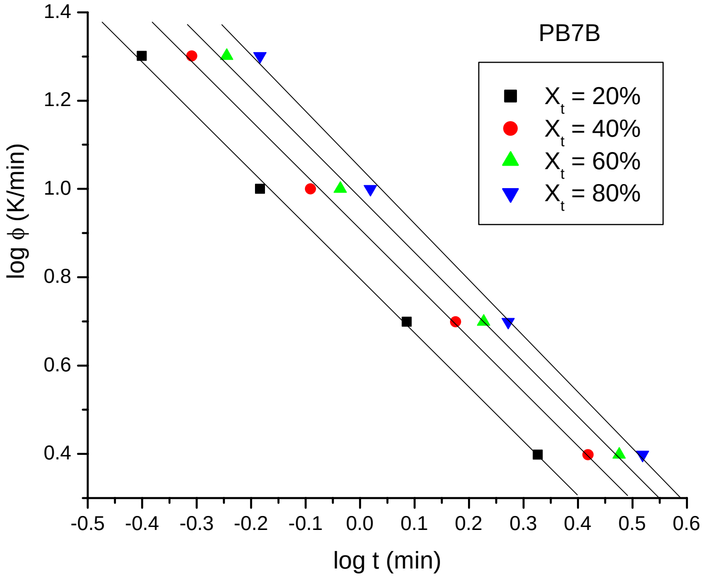

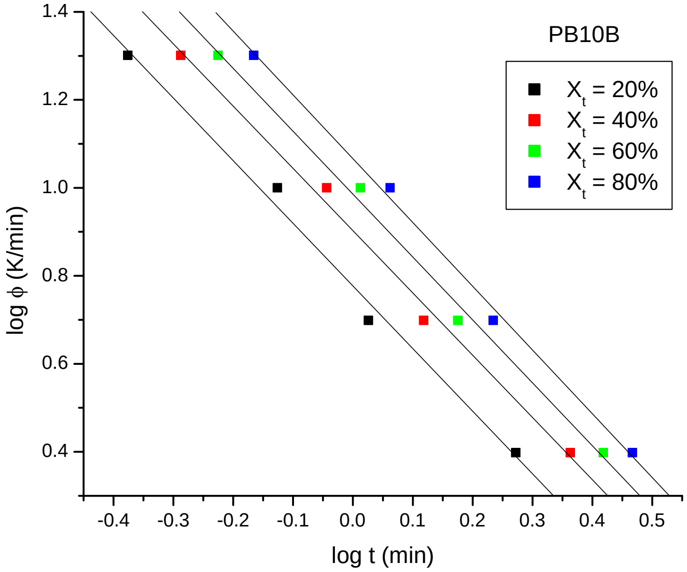

Figure 5.5: log ϕ vs log t for PB and PB/ $BaTiO_3$ nanocomposites

Table 5.3: Non-isothermal crystallization parameters for PB and PB/$BaTiO_3$ nanocomposites (combined Avrami - Ozawa analysis)

Sample	X_t (%)	F(T)	'a'
PB	20	8.1	1.3
	40	10.3	1.3
	60	12.2	1.3
	80	14.7	1.3
PB5B	20	7.4	1.4
	40	9.5	1.3
	60	11.2	1.4
	80	13.3	1.3
PB7B	20	6.3	1.2
	40	8.1	1.2
	60	9.5	1.2
	80	11.2	1.3
PB10B	20	6.0	1.4
	40	8.0	1.4
	60	9.7	1.4
	80	11.6	1.4

As the F(T) values signify the time required to reach the finite degree of crystallinity, the values of F(T) increases with the relative degree of crystallinity. The F(T) values are slightly lower for nanocomposites than that of pristine PB, suggesting time required to reach the certain relative degree of crystallinity is lowered as compared to pristine PB in presence of nanoparticles. The Avrami-Ozawa exponent is found to be 1.3 for PB and 1.2-1.4 for PB/$BaTiO_3$ nanocomposites.

5.3.2.1.2 Energy of Activation:

From the non-isothermal crystallization studies, it has been observed that the crystallization temperature is increased by 4-5 °C, while from the kinetics it is revealed that the rate of crystallization is enhanced due to incorporation of nanoparticles. The non-isothermal crystallization activation energy is calculated using the Kissinger equation as described in part 2.5.1.2. The plot of $\ln(\phi/T_c^2)$ vs $(1/T_c)$ is shown in Figure 5.6. From the slopes, the activation energies were calculated. Energy of activation for PB is found to be 131 kJ/mol, whereas 139 kJ/mol for PB5B and PB7B, and 120 kJ/mol for PB10B nanocomposite.

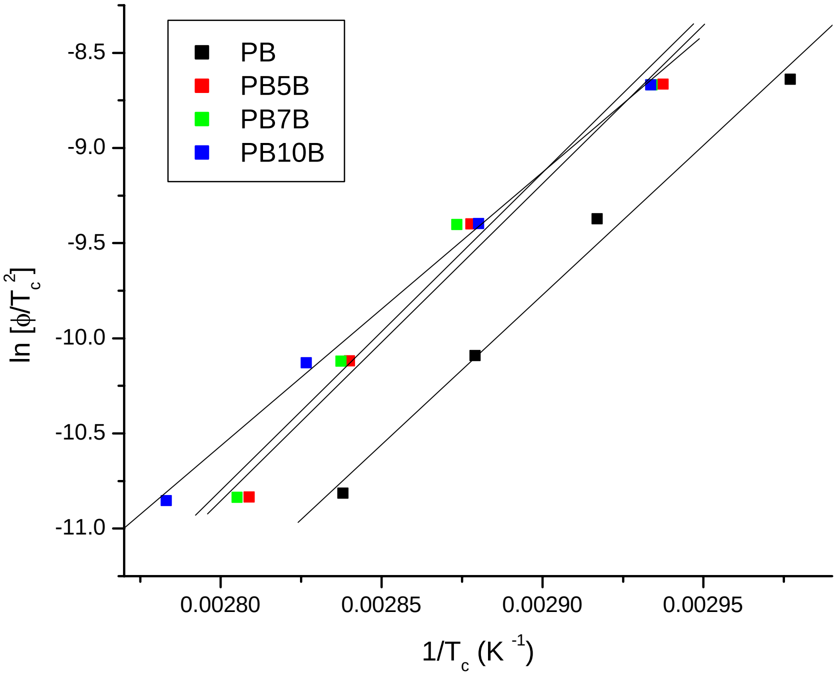

Figure 5.6: ln $[\phi/T_c^2]$ vs $1/T_c$ plots for PB and PB/ $BaTiO_3$ nanocomposites

These results suggest that the incorporation of nanoparticles have significant effect on nucleation rather than growth but the net influence is positive.

5.3.2.1.3 Nucleating Activity:

The nucleating activity of the $BaTiO_3$ nanoparticles is determined from the non-isothermal crystallization data. The detail analysis of this method has been described in part 2.5.1.3. The plot of log ϕ vs $1/\Delta T_c^2$ is shown in Figure 5.7. The nucleating activity is found to be 0.84, 0.82, and 0.61 for PB5B, PB7B, and PB10B respectively.

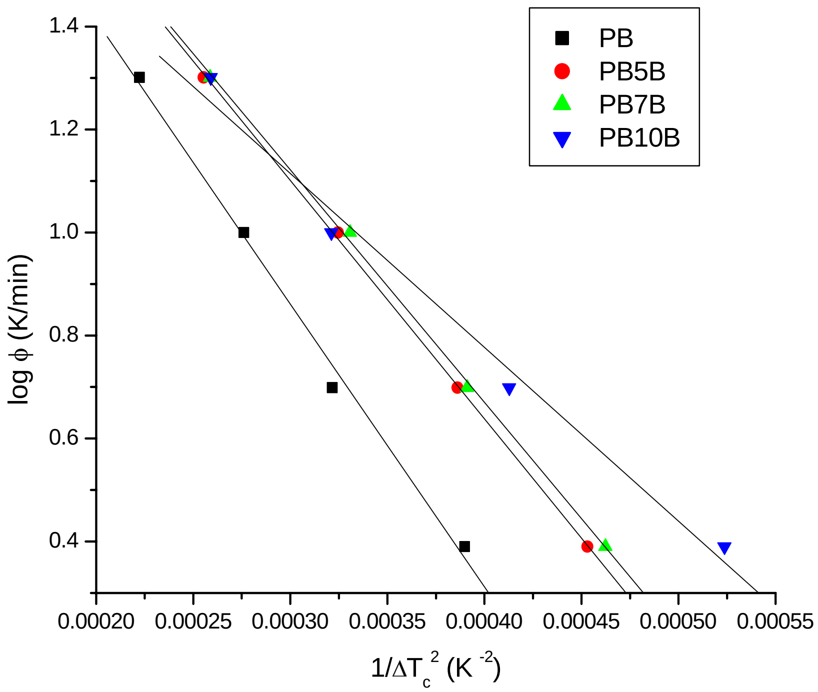

Figure 5.7: log ϕ vs $1/\Delta T_c^2$ for PB and PB/ $BaTiO_3$ nanocomposites

The values of nucleation activities suggest that the nanoparticles act as nucleating agent. Similar values of nucleating activity were reported for PP/SiO_2 nanocomposites [6].

5.3.2.2 Isothermal Crystallization:

Isothermal crystallization is studied in the temperature ranging from 76 to 84 °C for PB and PB/$BaTiO_3$ nanocomposites. The crystallization kinetics is studied using Avrami theory and the rate constant K and the Avrami exponent (n) is determined.

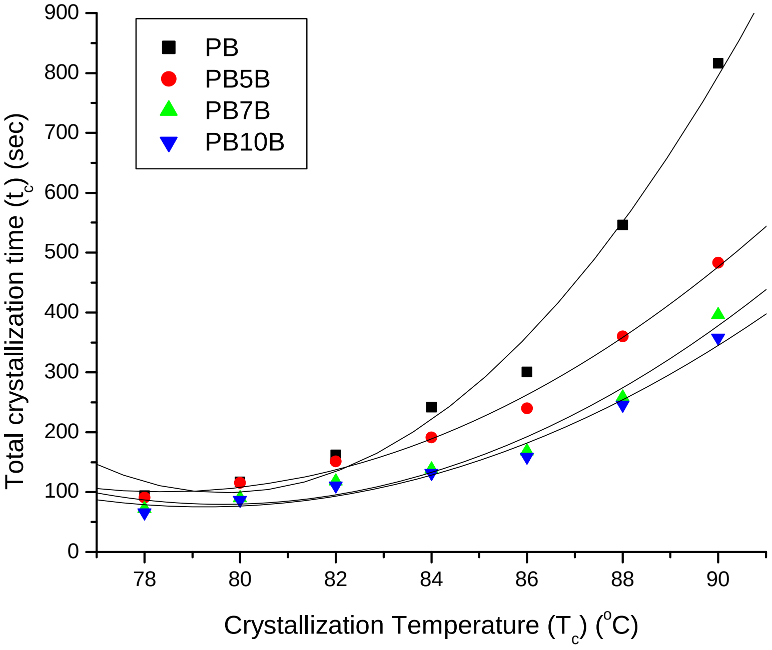

Figure 5.8: Total crystallization time for PB and PB/ $BaTiO_3$ nanocomposites

The total crystallization time is calculated from the isothermal curves and shown in Figure 5.8. It can be seen from the figure that the effect of nanoparticles on the crystallization behavior is more significant at higher crystallization temperatures.

At 84 °C, the total crystallization time t_c for PB is 242 seconds that reduced to 191, 138 and 132 seconds for PB5B, PB7B and PB10B. The lower values of total crystallization time (t_c) observed in case of nanocomposites suggest enhanced crystallization of PB in presence of $BaTiO_3$ nanoparticles. The rate constant at 84 °C for PB is 1.05×10^{-4} (min^{-1}), while it increased to 1.21×10^{-4} (min^{-1}), 1.4×10^{-4} (min^{-1}) and 2.37×10^{-4} (min^{-1}) for PB5B, PB7B and PB10B nanocomposites respectively. While the Avrami exponent remained almost same (~ 2) as that for pristine PB.

5.3.2.2.1 Isothermal Crystallization Kinetics:

The isothermal crystallization kinetics is also studied by Lauritzen - Hoffmann theory. Figure 5.9 shows the graph obtained from Lauritzen - Hoffman equation. The K_g values are determined from the slopes of the lines for PB and PB/$BaTiO_3$ nanocomposites.

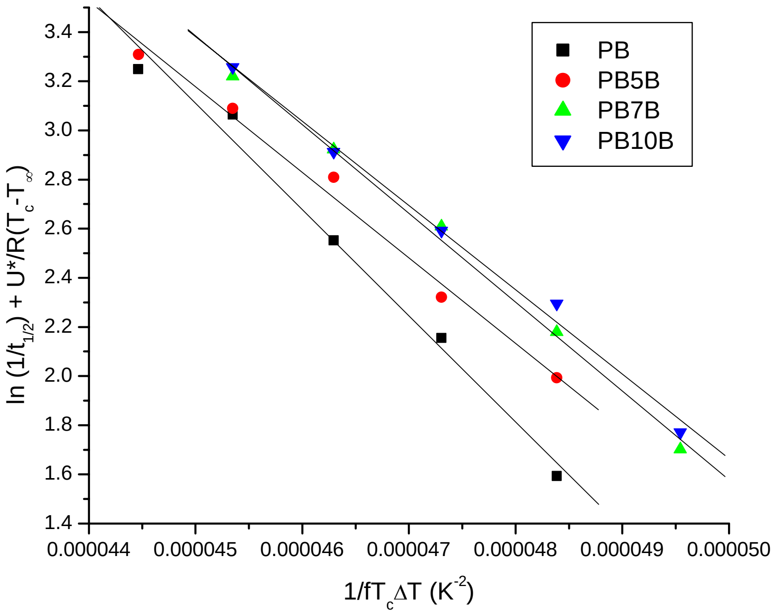

Figure 5.9: ln ($1/t_{1/2}$) + $U^*/R(T_c-T_\infty)$ vs $1/fT_c\,\Delta T$ (K^{-2}) for PB and PB/ $BaTiO_3$ Nanocomposites

The K_g value for PB is found to be 4.3×10^5 and it decreases to 3.5×10^5, 3.6×10^5, and 3.4×10^5 for PB5B, PB7B and PB10B nanocomposites respectively. It is reported that heterogeneous nucleation path makes the use of a foreign pre-existing surface to reduce the free energy opposing primary nucleation because of which the K_g value decreases [7]. The existence of $BaTiO_3$ nanoparticles reduces the work needed to create new surface and thus leading to faster crystallization rates. The lower values of K_g obtained in the present study is ascribed to the heterogeneous nucleation of PB in the nanocomposites.

5.3.2.2.2 Energy of Activation:

The energy of activation (E_a) for isothermal crystallization is calculated from the slope of the graph [1/n ln K vs $1/T_c$] shown in Figure 5.10.

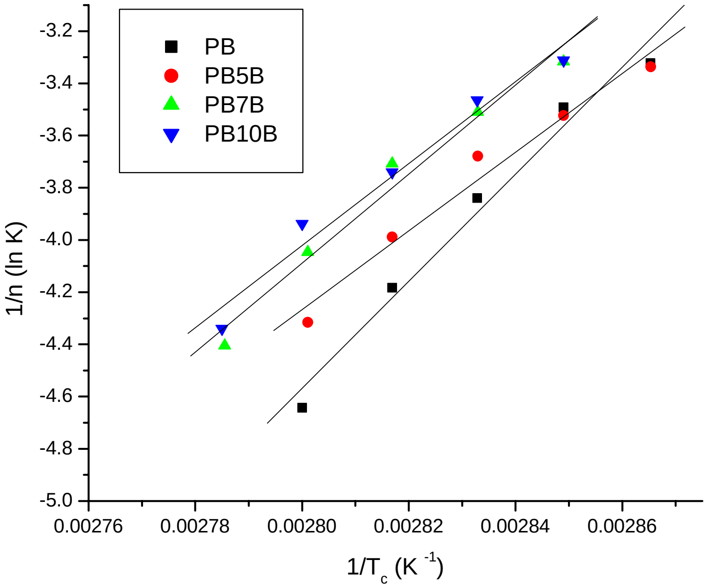

Figure 5.10: 1/n (ln K) vs $1/T_c$ for PB and PB/ $BaTiO_3$ nanocomposites

The values of E_a are found to be 170 kJ/mol for PB and 125.4, 141.8, and 130.5 kJ/mol for PB5B, PB7B, and PB10B nanocomposites respectively. The value of energy of activation for PB7B and PB10B nanocomposites is found to be marginally higher than that of PB5B. Similar results were observed in case of PP/$Mg(OH)_2$ nanocomposites [8].

5.3.3 Optical microscopy (OM):

Figure 5.11 shows the optical micrographs for PB and PB/$BaTiO_3$ nanocomposites.

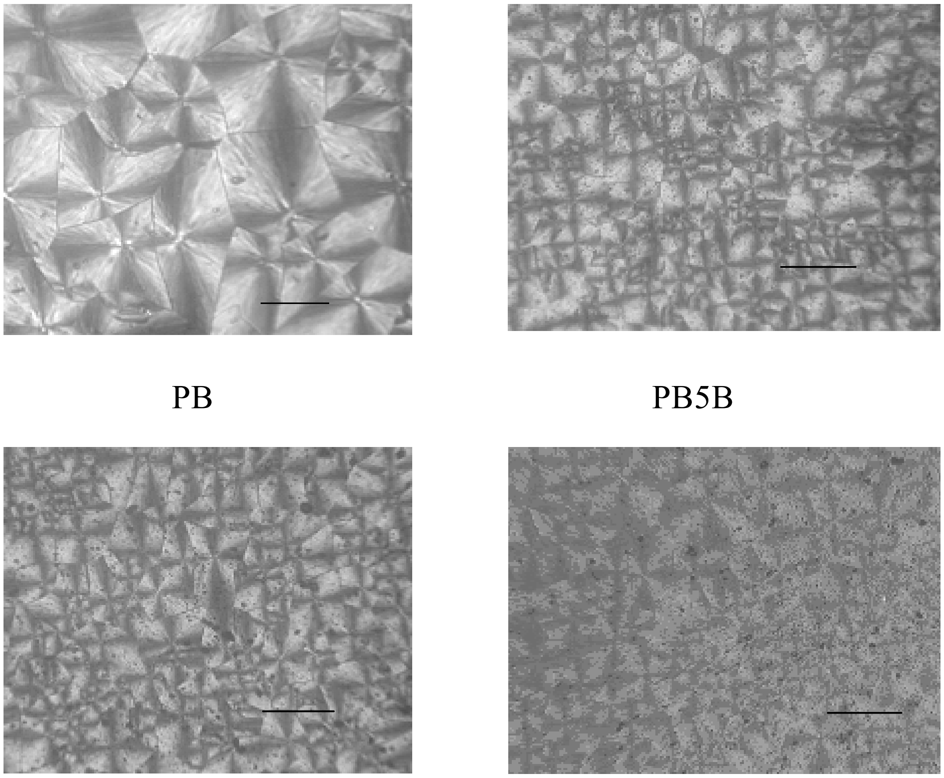

PB PB5B

PB7B PB10B

Figure 5.11: Optical micrographs for PB, PB/$BaTiO_3$ nanocomposites (Scale bar = 100 μm)

The micrographs indicate that the pristine PB shows well-defined spherulitic morphology. The spherulites of nanocomposites are of smaller size than that of pristine PB. However, the spherulites are not as well defined as in case of pristine PB. This observation is in contrast with the nanocomposites synthesized using organically modified clay and MWCNT in which disordered and disturbed crystallites are observed.

5.3.4 Phase transformation studies:

The phase transformation of PB/$BaTiO_3$ nanocomposites is studied using DSC. The DSC heating scans recorded at various time intervals for PB and PB10B nanocomposites are shown in Figure 5.12. As can be seen from the figure, the area under melting peak for Form II decreases with time, suggesting that it transforms into the stable Form I. The fractional conversion for Form I is calculated using the heat of fusions and is shown in figure 5.13.

$$\text{Fractional conversion} = \frac{\Delta H_f \text{ of Form I at time 't'}}{\Delta H_f \text{ of Form I at 216 hrs}}$$

Nanocomposites show higher conversion initially than PB. As the aging period is increased the extent of phase transformation from the Form II to Form I decreases as compared to pristine PB. The conversion of Form I for PB at 48 hrs is 35% while it increased to 47% for PB 10B nanocomposite.

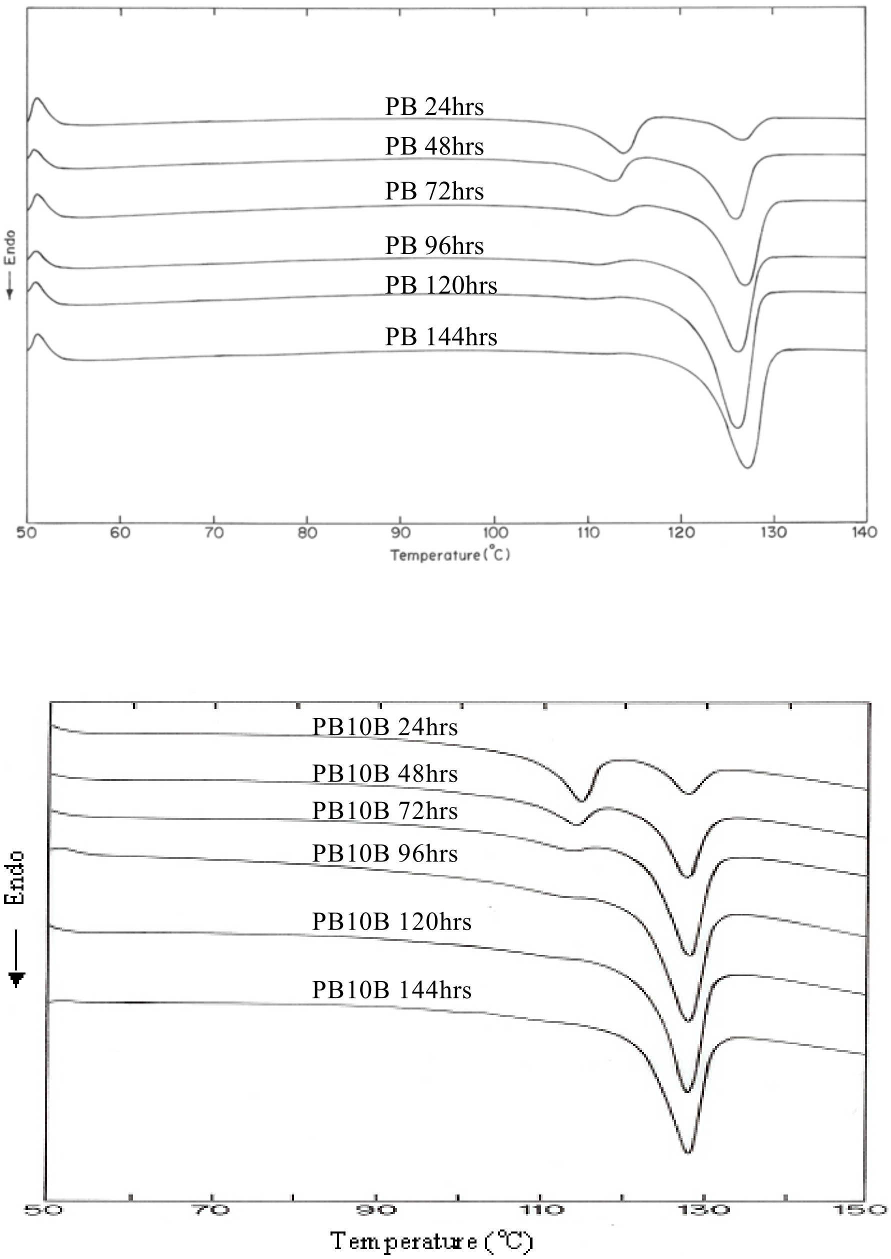

Figure 5.12: DSC thermograms for Phase transformation in PB and PB10B

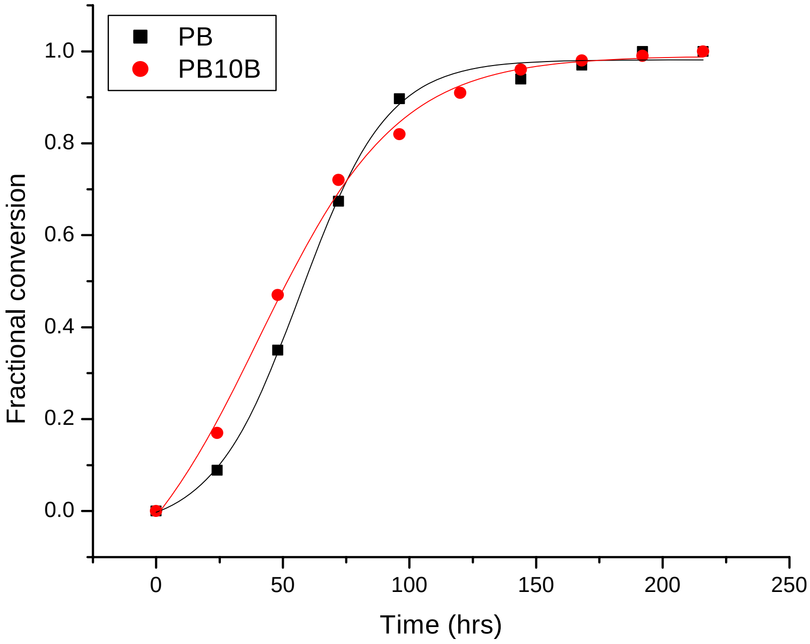

Figure 5.13: Fractional conversion for PB and PB10B nanocomposite

The half time for conversion is found to be 58 hrs for PB5B and PB7B, whereas it is 52 hrs for PB10B nanocomposite. The rate constants are found to be 2.8 × 10^{-4} (hrs^{-1}) and 1.38 × 10^{-3} (hrs^{-1}) for PB and PB10B nanocomposites respectively. The Avrami exponent (n) for nanocomposites is found to be 1.6 and that for PB is about 1.9. It is reported that the rate of phase transformation is enhanced with the decrease in amorphous fraction and the defective Form II crystals. The rate of phase transformation did not change much for 3 and 5% $BaTiO_3$ loadings. However, a marginal change is observed for 10% $BaTiO_3$ loading.

5.3.5 Viscoelastic properties:

5.3.5.1 Dynamic mechanical analysis (DMA):

Figure 5.14 depicts the temperature dependence of storage modulus (E') for PB and the PB/$BaTiO_3$ nanocomposites. It can be seen from the figure that in the sub glass transition region, the storage modulus increased by 5-6% compared to PB. The reinforcement effect is found to be more discernible in the rubbery regime as the storage modulus improved by about 22% at the temperature of 100 °C for all three nanocomposites.

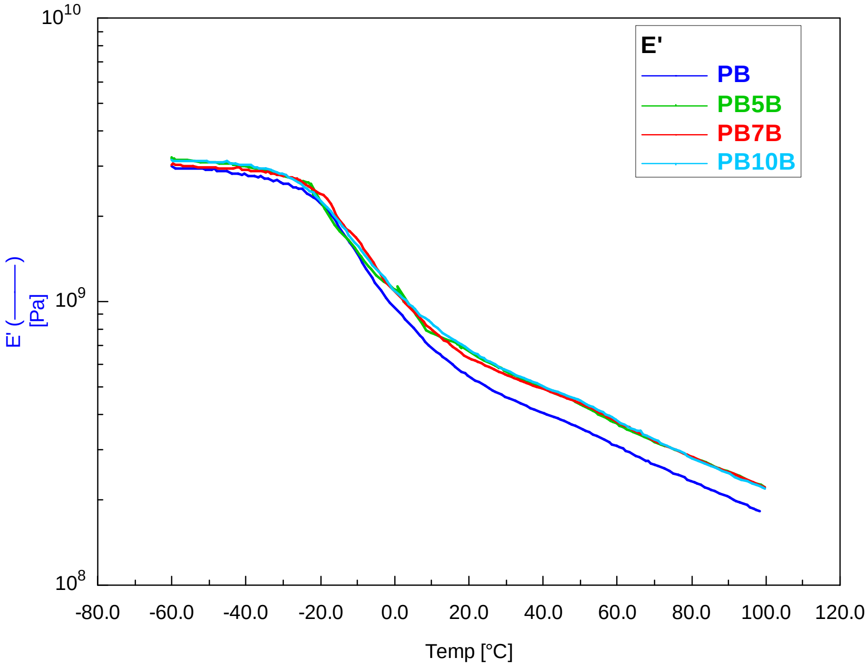

Figure 5.14: Storage modulus curves for PB, PB/$BaTiO_3$ nanocomposites

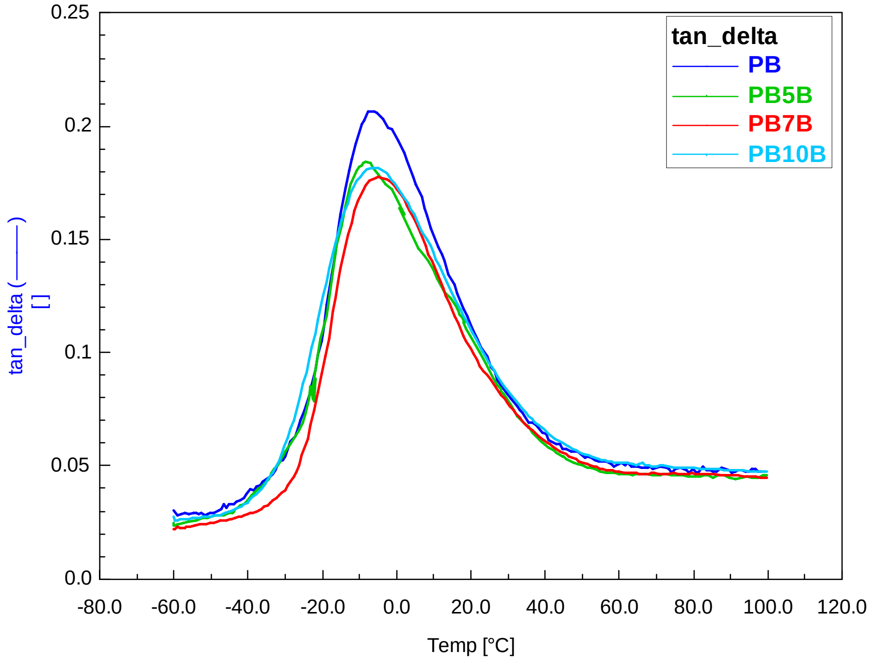

Figure 5.15: Tan δ curves for PB and PB/BaTiO$_3$ nanocomposites

Figure 5.15 depicts the tan δ curves for PB and PB/BaTiO$_3$ nanocomposites. The glass transition temperature is found to be almost same for all the compositions but the tan δ values for nanocomposites are lower than that of PB. The tan δ values (corrected with respect to the content of PB) are found to be 0.17, 0.16, and 0.16 for PB5B, PB7B, and PB10B nanocomposites respectively.

5.3.6 Dielectric spectroscopy (DES):

The permittivity (ε') of the nanocomposites is measured at room temperature. Figure 5.16 presents the frequency dependence of permittivity (ε') for PB and PB nanocomposites. As can be seen from the figure the permittivity is almost independent of frequency, which could be attributed to the non-polar nature of PB. The values of permittivity of nanocomposites are found to be 2.43, 2.65 and 2.86 for PB5B, PB7B and PB10B nanocomposites respectively. The marginal increase in the permittivity is attributed to the low volume percent of $BaTiO_3$. Vo and Shi [9] systematically investigated the effective dielectric permittivity of polymer filler composites. A number of parameters such as filler concentration, filler polymer interaction and size of the filler is taken into account. The values of dielectric permittivity are calculated based on this model. For this purpose, the dielectric permittivity of $BaTiO_3$ nanoparticles is also measured.

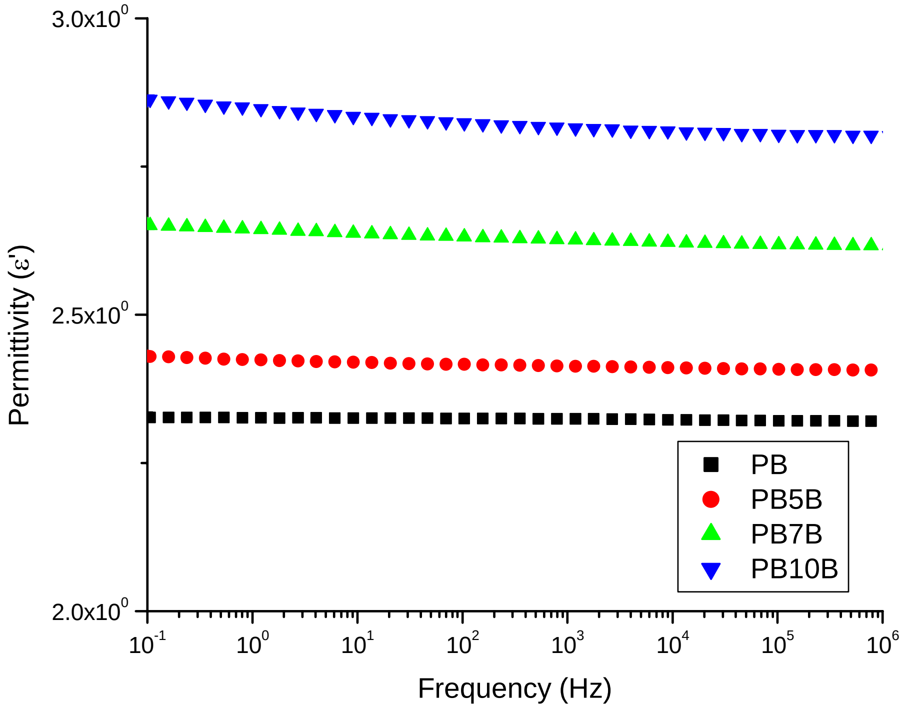

Figure 5.16: Permittivity for PB and PB/$BaTiO_3$ nanocomposites

The pellet of $BaTiO_3$ nanopowder is prepared by compaction using a die of 20 mm diameter at pressure 3.0 metric tons. The permittivity of pellet of $BaTiO_3$ is then measured over the same frequency range. The value of permittivity of $BaTiO_3$ at a frequency of 1 Hz is found to be 248 and is used for calculating the permittivity of the nanocomposites. The calculated values of permittivity using the model developed by Vo and Shi are found to be 2.57, 2.68 and 2.86 for PB5B, PB7B, and PB10B, which are in good agreement with the experimentally observed values.

5.3.7 Thermogravimetric analysis (TGA):

The effect of inorganic $BaTiO_3$ nanoparticles on the thermal stability of PB is studied. The percent weight loss of PB and PB/$BaTiO_3$ nanocomposites in nitrogen atmosphere is shown in Figure 5.17.

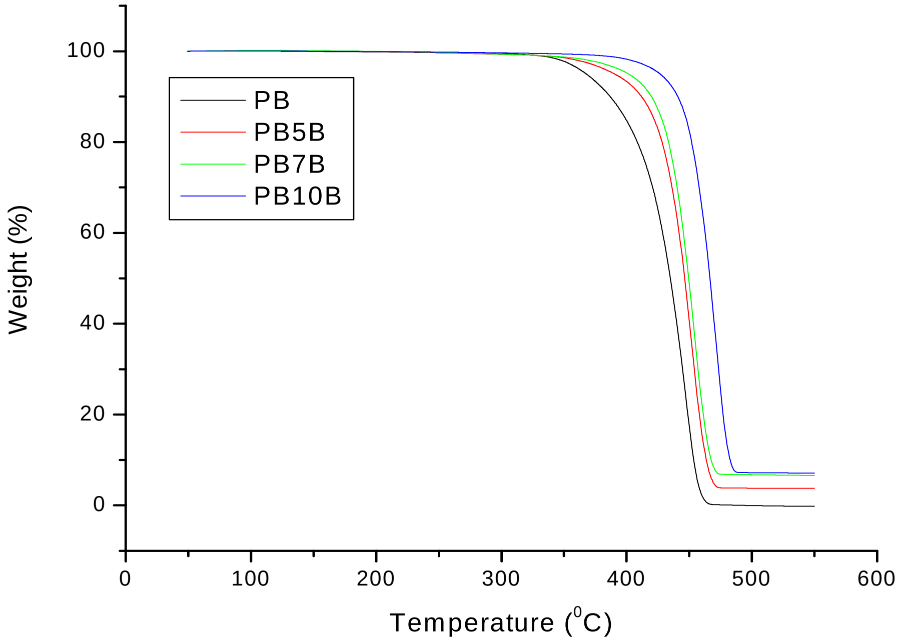

Figure 5.17: TGA thermograms for PB and PB/ $BaTiO_3$ nanocomposites

The temperature at the onset of degradation (TDI) increased for the nanocomposites compared to that of pristine PB and is increased by 24 °C, 35 °C and 54 °C for PB5B, PB7B and PB10B nanocomposites respectively. This suggests that the enhancement in thermal stability is due to the retardation effect of the inorganic nanoparticles. Residual weight after complete degradation of PB is found to be dependent on the content of $BaTiO_3$ nanoparticles.

5.4 Conclusions:

The nanocomposites with $BaTiO_3$ nanoparticles were successfully prepared using melt compounding method. The scanning electron micrographs showed homogeneous dispersion of nanoparticles as well as some aggregates. In non-isothermal crystallization studies, the crystallization temperature is increased by 5 °C for the nanocomposites. The values for Z_t are found to depend on the content of nanoparticles and the $t_{1/2}$ is significantly reduced. The higher values of Z_t and lower values of $t_{1/2}$ compared to pristine PB suggest that the nanoparticles act as nucleating agent. The F(T) values are found slightly lower for nanocomposites, suggesting time required to reach the defined degree of crystallinity is lowered as compared to pristine PB in presence of nanoparticles. The nucleating activity is found to be 0.84, 0.82, and 0.61 for PB5B, PB7B, and PB10B nanocomposites. The isothermal crystallization studies revealed a decrease in total crystallization time and higher rate constants as compared to pristine PB. Lower values of K_g are obtained in the present study, which are ascribed to the heterogeneous nucleation of PB in presence of nanoparticles. Optical micrographs exhibited a slight reduction in the size of spherulites. It is interesting to note that phase transformation studies, revealed marginal change in rate of crystal-to-crystal phase transformation while the crystallization results showed increase in crystallization rates. The dynamic mechanical analysis revealed an increase in storage modulus in rubbery regime. The dielectric permittivity at 0.1 Hz increased from 2.3 to 2.86 for PB10B nanocomposite. The thermogravimetric analysis revealed increase in the thermal stability for the nanocomposites compared to pristine PB.

References:

[1] Zhao H, Li R. Journal of Polymer Science: Part B: Polymer Physics 43, 3652 **(2005)**

[2] Tang J, Wang Y, Liu H, Belfiore L. Polymer 45, 2081 **(2004)**

[3] Xia X, Cai S, Xie C. Materials Chemistry and Physics 95, 122 **(2006)**

[4] Kontou E, Niaounakis M. Polymer 47, 1267 **(2006)**

[5] Guangneng, F, Lixia H, Xueguang H. Journal of Crystal Growth 279, 489 **(2005)**

[6] Bikiaris DN, Vassiliou A, Pavlidou E, Karayannidis GP. European Polymer Journal 41, 1965 **(2005)**

[7] Papageorgiou G, Achilias D, Bikiaris DN, Karayannidis GP. Thermochimica Acta 17, 128 **(2005)**

[8] Yin J, Wang S, Zhang Y, Zhang Y. Journal of Polymer Science: part B: Polymer Physics 43, 1914 **(2005)**

[9] Vo H, Shi F. Microelectronics Journal, 33, 409 **(2002)**

Chapter 6

Conclusions and Scope for future work

6.1 Conclusions:

Nanocomposites of PB are successfully prepared by melt compounding technique and characterized for the first time. Different nanofillers such as, clay, MWCNT, and $BaTiO_3$ nanoparticles are used for this purpose. The structure, morphology, crystallization, crystal-to-crystal phase transformation and thermo-mechanical behavior of the nanocomposites are studied using various techniques.

In the following sections, the effectiveness of the nanofillers in modifying the crystallization and phase transformation behavior is evaluated by comparing the three nanocomposites containing 5 wt% of the filler.

The PB/clay nanocomposites show intercalated structures with uniform dispersion of clay layers in the polymer matrix. The SEM micrographs for PB/MWCNT nanocomposite exhibit dispersion of bundles of MWCNTs in the matrix, whereas in PB/$BaTiO_3$ nanocomposites, uniform dispersion of $BaTiO_3$ nanoparticles with some agglomerates having size 1-4 μm is observed.

The crystallization studies reveal enhanced crystallization rates for non-isothermal as well as isothermal crystallization for nanocomposites with all the nanofillers. The non-isothermal crystallization studied using modified Avrami and combined Avrami-Ozawa theory. The higher values of Z_t and lower values of $t_{1/2}$ and F(T) for the nanocomposites as compared to PB suggests enhanced crystallization rates. The nucleating activity of the nanocomposites is found to be about 0.89, 0.47 and 0.82 for PB5N, PB5C and PB5B nanocomposites respectively, suggesting that the MWCNTs offer most active surface for crystallization.

In isothermal crystallization, the effect of nanofillers is compared by plotting the total crystallization time against the temperature. Figure 6.1 depicts the variation of total crystallization time versus temperature for different nanofillers.

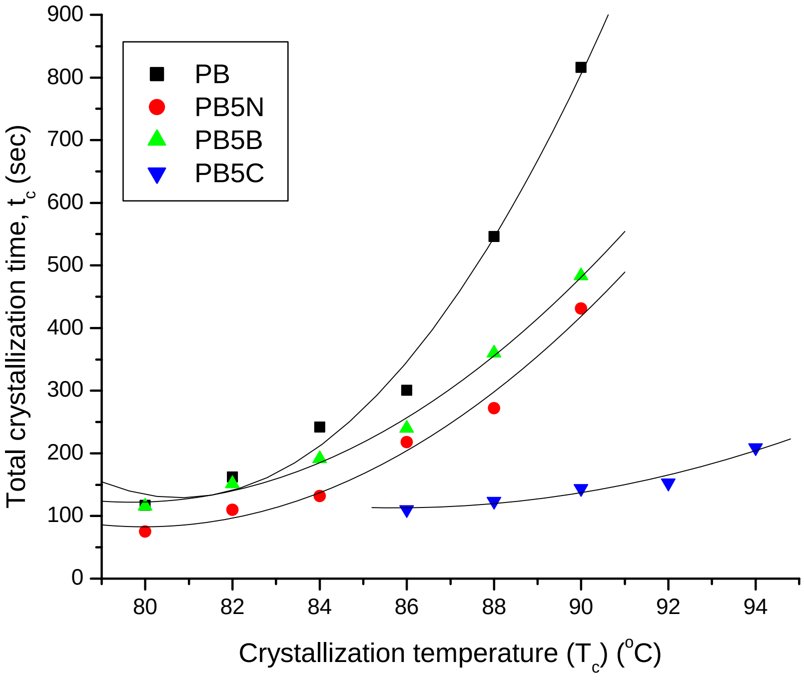

Figure 6.1: Total crystallization time for PB and PB nanocomposites

As can be seen from the figure, PB5N and PB5B show marginal decrease while PB5C nanocomposite exhibits significantly lower values of 't_c'. The total crystallization time (t_c) at 86 °C for PB is found to be about 301 seconds, while it decreases to 218, 110 and 240 seconds for PB5N, PB5C, and PB5B nanocomposites respectively. This suggests heterogeneous nucleation of PB in presence of nanofillers and MWCNT is found to be more effective than clay and $BaTiO_3$ nanoparticles. This effect is more pronounced at higher crystallization temperatures.

The optical micrographs of PB and the nanocomposites containing 5 wt% filler are shown in Figure 6.2. As can be seen form the micrographs, well-defined spherulitic morphology is observed for pristine PB and PB5B nanocomposite, but a disturbed morphology is observed for PB5N nanocomposite. The nanocomposites with MWCNT exhibited very small and disordered crystallites.

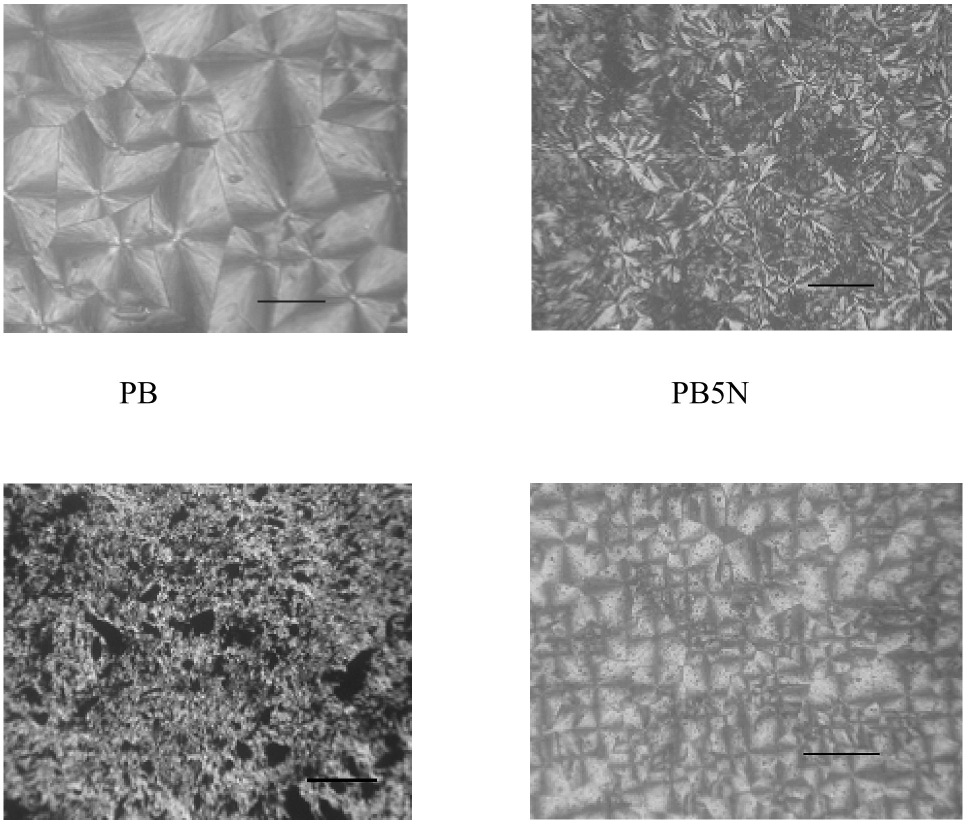

PB PB5N

PB5C PB5B

Figure 6.2: Optical micrographs for PB and PB nanocomposites

(Scale bar = 100 μm)

The dynamic mechanical analysis shows improved storage modulus for all the nanocomposites compared to pristine PB, but the highest improvement is found for the nanocomposites with MWCNTs. From the Figure 6.3 it can be seen that the improvement in the storage modulus is higher in the rubbery state as compared to the glassy state signifying the reinforcing effect of the nanofillers. At 25 °C, the increase in modulus is found to be about 40, 46 and 22% while at 100 °C it is observed about 25, 42 and 22% for PB5N, PB5C and PB5B nanocomposites respectively.

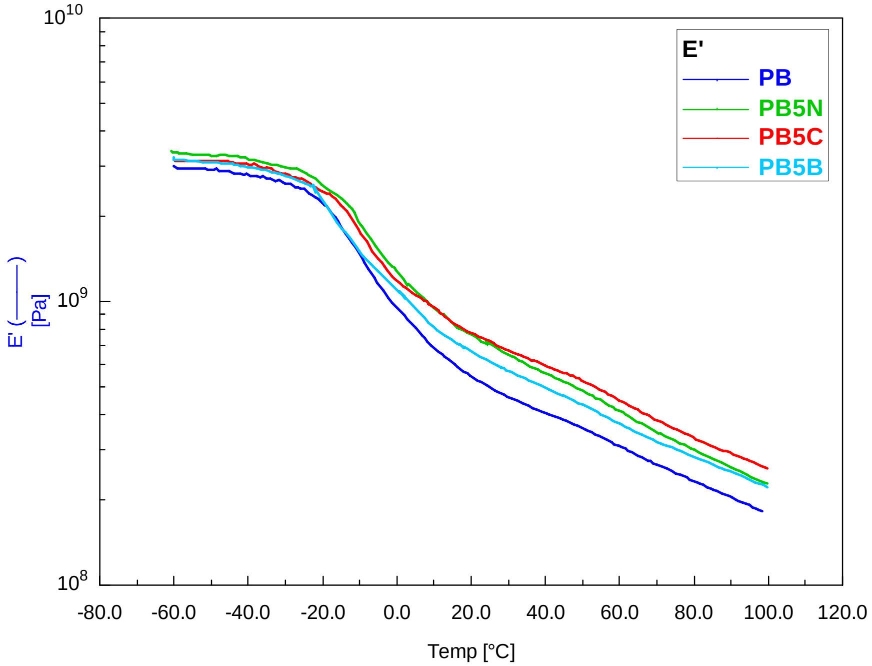

Figure 6.3: The storage modulus (E') curves for PB and PB nanocomposites

The reinforcing effect of MWCNT is evident from the colossal increase in storage modulus at higher temperatures.

The thermogravimetric analysis indicates enhanced thermal stability for all nanocomposites. The onset temperature of degradation is increased by about 28, 74 and 25 °C for PB5N, PB5C, and PB5B nanocomposites respectively, which shows that the incorporation of MWCNT results in significant increase in the degradation initiation temperature.

The important aspect of this study is the kinetics of phase transformation from metastable tetragonal form (Form II) to stable twinned hexagonal form (Form I). The fractional conversions of Form I of PB and PB with 5 wt% nanofillers for various time intervals are shown in figure 6.4. Avrami theory is used to study the kinetics of phase transformation.

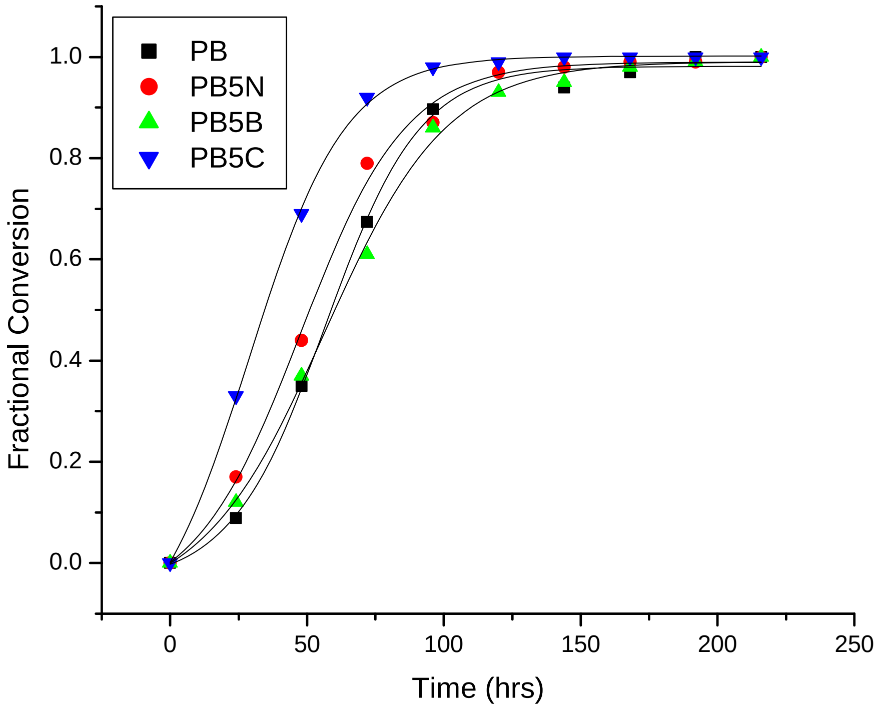

Figure 6.4: Fractional conversion of Form I for PB and PB nanocomposites

The half time for phase transformation (50% conversion to Form I) of PB is about 58 hrs and it is 50.6, 34.6, and 59 hrs for PB5N, PB5C, and PB5B nanocomposites respectively. The clay and MWCNT are found to be more effective in enhancing the rate than $BaTiO_3$ nanoparticles. The observed difference in the variations for the rate of phase transformation with different nanofillers could be explained on the basis of crystallinity. It is found that the decrease in amorphous content along with the enhanced nucleation of Form I (as observed in case of MWCNT nanocomposites) results in significant increase in the phase transformation rate. Finally, our results demonstrate that clay, MWCNT, and $BaTiO_3$ nanoparticles provide active nucleation sites for the crystallization. MWCNTs play a significant role in enhancing the rate of phase transformation.

The main conclusions of this study are:

- All the nanofillers used in this study enhance the crystallization rate.
- The phase transformation rates however, are found to be different for the three nanofillers.
- The rate of phase transformation is higher with incorporation of MWCNTs compared to other nanofillers in PB matrix.
- The incorporation of nanofillers results in higher storage modulus and improved thermal stability. The extent of improvement is maximum for MWCNT nanocomposites as compared to clay and $BaTiO_3$ nanocomposites.

6.2 Scope for future work:

Based on the results of the present work following studies can be carried out in future.

1. Study of effect of temperature on the phase transformation kinetics of PB nanocomposites.
2. Crystallization and phase transformation could be studied by novel routes such as, blends with low molecular weight organic compounds; for example, dihydrogenated oligo cyclopentadiene, α and β pinene, limonene, rosin and terpenes etc.
3. Effect of other nanofillers can be explored to study the crystallization, phase transformation and mechanical properties of PB.
4. Study on the use of compatibilizer, functionalization of the nanotubes and modification of nanoparticles can be carried out, as it would enhance the dispersion of nanofillers resulting in improved properties of nanocomposites.
5. Electrospinning of these nanocomposites could be carried out to see the effect of orientation of the nanofillers on the crystallization and crystal-to-crystal phase transformation.

List of Publications

1) **S D Wanjale** and J P Jog, Poly (1-butene)/clay nanocomposites: Preparation and Properties. Journal of Polymer Science Part B: Polymer Physics. 41(10), 1014, 2003.

2) **S D Wanjale** and J P Jog, Poly (1-butene)/clay nanocomposites: A Crystallization Study. Journal of Macromolecular Science – Physics. B42, 6, 1141, 2003.

3) **S D Wanjale** and J P Jog, Effect of modified layered silicates and compatibilizer on the properties of PMP/clay nanocomposites. Journal of Applied Polymer Science. 90, 12, 3233-3238, 2003.

4) **S D Wanjale** and J P Jog, PMP/clay nanocomposites: Effect of organically modified layered silicates. Polymer International. 53(1), 101-105, 2004.

5) **S D Wanjale**, L Priya and J P Jog, Crystallization and melting behavior of Polypropylene in presence of hydrogenated dicyclopentadiene.
Journal of Macromolecular Science – Physics. B42(5), 1007, 2003.

6) Sunil R. Vaidya, Ulhas K. Kharul, Shobha D. Chitambar, **Santosh D. Wanjale** and Yogesh S. Bhole, Removal of hepatitis A virus from water by polyacrylonitrile-based ultrafiltration Membranes. Journal of Virological Methods, 119(1), 7-9, 2004.

7) **S D Wanjale** and J P Jog, Crystallization and Phase transformation kinetics of poly (1-butene)/MWCNT nanocomposites. Polymer 47, 6414-6421, 2006.

8) **S D Wanjale** and J P Jog, Viscoelastic and Dielectric behavior of Poly(1-butene)/MWCNT nanocomposites. Journal of Macromolecular Science – Physics. B45(6), 1053-1064, 2006.

Book Chapter: Effect of nanofillers on crystallization, crystal-to-crystal phase transformation and thermo-mechanical properties of poly(1-butene)

Title: **Polyolefin Composites**

Publisher: John Wiley and sons, Inc. (To be Published in January 2008)

Oral Presentations

1) Preparation and Properties of PMMA/layered silicate nanocomposites using solution intercalation technique.
   Santosh D Wanjale and Jyoti. P. Jog.
   International Conference on Advances in Polymer Blends, Composites, IPNs and Gels: Macro to Nano Scales. March 21-23, Kottayam, Kerala, India. 2005.

2) PC/PCL Clay Nanocomposites: Preparation and Properties.
   Santosh D Wanjale, S. Kumari, **J. P. Jog**.
   Polymer Nanocomposites, 2003, Quebec, Canada, October 6-8, 2003.

3) Chemical modification of PAN-UF membranes
   Santosh D Wanjale, Y S Bhole, U K Kharul.
   National conference on desalination and water reuse, Madurai, India. February 22-23, 2001.